THIAGO DE PAULA SALES

SIMULTANEOUS USE OF SHAPE MEMORY ALLOYS AND PERMANENT MAGNETS IN MULTISTABLE SMART STRUCTURES FOR MORPHING AIRCRAFT APPLICATIONS

FEDERAL UNIVERSITY OF UBERLÂNDIA
SCHOOL OF MECHANICAL ENGINEERING
2017

THIAGO DE PAULA SALES

SIMULTANEOUS USE OF SHAPE MEMORY ALLOYS AND PERMANENT MAGNETS IN MULTISTABLE SMART STRUCTURES FOR MORPHING AIRCRAFT APPLICATIONS

Thesis presented to the Mechanical Engineering Graduate Program of the Federal University of Uberlândia, as a partial fulfillment of the requirements for the degree of **DOCTOR IN MECHANICAL ENGINEERING**

Focus Area: Solid Mechanics and Vibrations

Advisor: Prof. Dr. Domingos Alves Rade

UBERLÂNDIA – MG
2017

Dados Internacionais de Catalogação na Publicação (CIP)
Sistema de Bibliotecas da UFU, MG, Brasil

S163s Sales, Thiago de Paula, 1988-
2017 Simultaneous use of shape memory alloys and permanent magnets in multistable smart structures for morphing aircraft applications/ Thiago de Paula Sales. - 2017
135 p. : il.

Orientador: Domingos Alves Rade.
Tese (doutorado) – Universidade Federal de Uberlândia, Programa de Pós-Graduação em Engenharia Mecânica.
Inclui bibliografia.

1. Engenharia mecânica - Teses. 2. Ligas com memória de forma - Teses. 3. Ímãs permanentes - Teses. 4. Aeronaves com geometria variável - Teses. I. Rade, Domingos Alves. II. Universidade Federal de Uberlândia. Programa de Pós-Graduação em Engenharia Mecânica. III. Título.

CDU: 621

THIAGO DE PAULA SALES

SIMULTANEOUS USE OF SHAPE MEMORY ALLOYS AND PERMANENT MAGNETS IN MULTISTABLE SMART STRUCTURES FOR MORPHING AIRCRAFT APPLICATIONS

Thesis **APPROVED** by the Mechanical Engineering Graduate Program of the Federal University of Uberlândia

Focus Area: Solid Mechanics and Vibrations

Examining Committee:

Prof. Dr. Domingos Alves Rade – ITA – Advisor

Profa. Dra. Aline Souza de Paula – UnB

Prof. Dr. Leonardo Sanches – UFU

Prof. Dr. Paulo Sérgio Varoto – EESC-USP

Prof. Dr. Roberto Mendes Finzi Neto – UFU

Uberlândia, July 28th, 2017

ACKNOWLEDGMENTS

To my wife, Martina, for her support, encouragement, and endurance during the hard times I've had while performing research.

To my mom and brother, Norma and Dhiego, for their patience, understanding and support.

To my doctoral advisor, Prof. Dr. Domingos A. Rade, for always giving me opportunities, motivation, and example.

To my supervisor at the University of Michigan, Prof. Dr. Daniel J. Inman, for receiving me during one year at his lab, and being an exemplary person with whom I enjoyed working with.

To my lab mates and colleagues at the Federal University of Uberlândia, for their friendship over the years.

To the lab mates I've had, and friends I've made while at the University of Michigan, for having welcomed me at Ann Arbor — I hope seeing all of you again one day!

To all professors I've had over the years who kept me motivated and interested in my studies.

To the examining committee for having evaluated the Thesis and provided valuable contributions to the work.

To the Graduate Program of the School of Mechanical Engineering for having me as their student.

To the Brazilian agencies CNPq (National Council for Scientific and Technological Development) and CAPES (Coordination for the Improvement of Higher Education Personnel), as well as to the Science without Borders scholarship program, for their financial support.

SALES, T. P. **Simultaneous use of shape memory alloys and permanent magnets in multistable smart structures for morphing aircraft applications**. 2017. 135 p. Ph. D. Thesis. Federal University of Uberlândia, Uberlândia.

ABSTRACT

This Thesis considers the simultaneous use of shape memory alloys and permanent magnets for achieving multistable smart structures aiming towards morphing applications. Motivation for this approach lies in the poor energetic efficiency of shape memory alloys, which can void system-level benefits provided by morphing technologies. Multistability can therefore be adopted to prevent continuous operation of shape memory alloy actuators. Objectives of the study involve the combination of shape memory alloys and permanent magnets in new geometrical arrangements to achieve multistable behavior; the development of a numerical modeling procedure that is able to simulate the multi-physics nature of the studied systems; and the proposal of a geometric arrangement for morphing applications that is based on a repeating pattern of unit cells which incorporate the combined use of shape memory alloy wires and permanent magnets for multistability. The proposed modeling strategy considers a geometrically nonlinear beam finite element; a thermo-mechanical constitutive behavior for shape memory alloys; the interaction of cuboidal permanent magnets with arbitrary orientations; and node-to-element contact. Experiments are performed with three distinct systems, including a proof-of-concept beam, a three cell morphing beam metastructure, and a morphing airfoil prototype with six unit cells. Results show that the combination of shape memory alloys and permanent magnets indeed allows for multistable behavior. Furthermore, the distributed actuation capabilities of the morphing metastructure allow for smooth and localized geometrical shape changes.

Keywords: shape memory alloys, permanent magnets, multistability, morphing

SALES, T. P. **Uso simultâneo de ligas com memória de forma e ímãs permanentes em estruturas inteligentes multi-estáveis para aplicações em aeronaves com geometria variável**. 2017. 135 p. Tese de Doutorado. Universidade Federal de Uberlândia, Uberlândia.

RESUMO

Esta Tese considera o uso simultâneo de ligas com memória de forma e ímãs permanentes para a obtenção de estruturas inteligentes multiestáveis, com vistas a sua aplicação em aeronaves de geometria variável. A motivação para tal abordagem reside na baixa eficiência energética associada às ligas com memória de forma, a qual pode eliminar benefícios oriundos de tecnologias relacionadas a geometria variável. Multiestabilidade pode, desta forma, ser adotada para prevenir operação contínua de atuadores baseados em ligas com memória de forma. Objetivos do estudo envolvem a combinação de ligas com memória de forma e ímãs permanentes em novos arranjos geométricos para a obtenção de comportamento multiestável; o desenvolvimento de um procedimento de modelagem numérica que pode simular a natureza multifísica dos sistemas estudados; e a proposição de um arranjo geométrico para aplicações que envolvem geometria variável, o qual é baseado num padrão repetitivo de células unitárias que incorporam o uso combinado de ligas com memória de forma e ímãs permanentes para multiestabilidade. A estratégia de modelagem proposta considera um elemento finito de viga com não-linearidades geométricas; um modelo constitutivo termomecânico para ligas com memória de forma; a interação entre ímãs permanentes cúbicos com orientação arbitrária; e contato entre elemento-e-nó no contexto de elementos finitos. Experimentos são realizados com três sistemas distintos, incluindo uma viga para prova de conceito, uma metaestrutura do tipo viga com geometria variável composta por três células unitárias, e um protótipo de aerofólio com geometria variável composto por seis células unitárias. Resultados mostram que a combinação de ligas com memória de forma e ímãs permanentes permite a obtenção de comportamento multiestável. Além disso, a característica de atuação distribuída das metaestruturas com geometria variável permite alterações de forma suaves e localizadas.

Palavras chave: ligas com memória de forma, ímãs permanents, multiestabilidade, sistemas com geometria variável

LIST OF FIGURES

LIST OF TABLES

LIST OF SYMBOLS

Greek letters and symbols

α	constant used to specify a time integration algorithm
β	shape memory alloy stress-free transformation strain
$\bar{\beta}$	weighting coefficient used for the computation of $\mathbf{y}^*$
δ	virtual variation
ϵ	axial strain field
ϵ_{abs}	absolute error tolerance
ϵ_n	small constant used for approximating normal contact conditions
ϵ_s	small constant used for approximating tangential contact conditions
η	line-search step
ϕ	Helmholtz specific free energy
γ	shear strain field
κ	curvature field
λ	amplitude of the normal component of the the contact force
λ_c	normal contact force related to the contact pair c
$\bar{\mu}$	dynamic coefficient of friction between two surfaces
μ_0	vacuum permeability
μ_c	critical value for thermodynamic driving force
μ_i	shape memory alloy thermodynamic transformation driving forces, $i = \{1, 2\}$
ν_0	constant that controls the speed with which phase transformation occurs
π	irrational number, equal to the ratio of a circle's circumference to its diameter

ψ	beam cross-section rotation field
ψ_k	beam cross-section rotation at node k
$\psi_k^{(e)}$	beam cross-section rotation at node k of element e
ρ	specific mass
σ	shape memory alloy wire longitudinal stress
τ	amplitude of the tangent component of the the contact force
$\bar{\tau}$	normalized amplitude of the tangent component of the contact force
$\bar{\tau}_c$	normalized tangential contact force related to the contact pair c
ξ_1	tensile martensite variant volumetric phase fraction
ξ_2	compressive martensite variant volumetric phase fraction
ξ_3	austenite volumetric phase fraction
Δs	difference between martensite and austenite specific entropies
Δt	integration time step
ΔE	difference between martensite and austenite longitudinal stiffness moduli
$\boldsymbol{\epsilon}$	vector of strain fields
$\boldsymbol{\lambda}$	vector of normal contact forces of all contact pairs
$\boldsymbol{\mu}$	vector of shape memory alloy thermodynamic transformation driving forces
$\bar{\boldsymbol{\tau}}$	vector of normalized tangential contact forces of all contact pairs
$\boldsymbol{\xi}$	vector of martensite volumetric phase fractions
$\boldsymbol{\xi}_a$	vector of martensite volumetric fractions related to the shape memory alloy wire actuator a
$\mathbf{\xi}$	vector of martensite volumetric fractions of all shape memory alloy wire actuators
$\Delta\mathbf{u}_{\text{system}}$	increment vector used to update $\mathbf{u}_{\text{system}}$ during solution
${}^{b}\mathbf{\Phi}^{a}$	rotation matrix used to transform coordinates from the basis related to frame a to those of frame b
∂V_{b_1}	(target) surface of the volume V_{b_1} of a contact pair
∂V_{b_2}	(contactor) surface of the volume V_{b_2} of a contact pair

$\boldsymbol{\nabla}$	nabla operator

Roman letters and symbols

a	line-search residual function
c_0	shape memory alloy reference specific heat
c_I	constant that controls hardening during shape memory alloy phase transformation
d	diameter
g	gap function that measures the signed distance between the surfaces of a contact pair
h	convective heat transfer film coefficient
k	summation index; used to indicate node number; used as Newton-Raphson iteration index
$k_{\Delta t}$	integer number used to refine the time step Δt
k_{LS}	number of iterations after which line-search is performed
k_{max}	maximum number of iterations
$(l_i)_m$	half the length of magnet m along direction i, $i = \{1, 2, 3\}$
m	external distributed bending moment
n	external distributed axial load; used as time discretization index
$n^{(e)}$	number of nodes of element e
q	external distributed shear force
$\mathscr{s}$	sigmoid function
s_0	shape memory alloy reference specific entropy
s_A	austenite specific entropy
s_M	martensite specific entropy
t	time
$\dot{u}$	amplitude of the tangential component of the relative velocity vector $\dot{\mathbf{u}}_{b_2,b_1}$
u_i	displacement along direction i, $i = \{1, 2, 3\}$

$(u_i)_k$	displacement of node k along direction i, $i = \{1, 2, 3\}$
$(u_i)_k^{(e)}$	displacement of node k of element e along direction i, $i = \{1, 2, 3\}$
w_n	constraint function for normal contact conditions
w_s	constraint function for frictional contact conditions
x_i	deformed position along direction i, $i = \{1, 2, 3\}$
$(x_i)_k$	deformed position of node k along direction i, $i = \{1, 2, 3\}$
A	area
A_s	cross-section area corrected for shear effects
B_m	residual magnetization of magnet m
E	longitudinal stiffness modulus
E_A	austenite longitudinal stiffness modulus
E_M	martensite longitudinal stiffness modulus
$E(\xi)$	shape memory alloy longitudinal stiffness modulus
$(F_i)_k$	force applied at node k along direction i
G	transversal stiffness modulus
H	Heaviside function
$\tilde{H}$	smooth Heaviside function
I	area moment of inertia
K	big number used in the computation of a sigmoid function
L	length
M	bending moment
N	axial force
N_a	total number of shape memory alloy wire actuators
N_c	total number of contact pairs
$N_{\max}$	maximum number of integration time steps
$N_k^{(e)}$	shape function associated with node k of element e
P_E	electrical power
Q	shear force
R_T	residual equation related to T

$(R_T)_a$	residual equation related to T of the a-th shape memory alloy wire actuator
R_λ	residual equation related to λ
$(R_\lambda)_c$	residual equation related to λ of the contact pair c
$R_{\bar{\tau}}$	residual equation related to $\bar{\tau}$
$(R_{\bar{\tau}})_c$	residual equation related to $\bar{\tau}$ of the contact pair c
T	temperature
T_a	temperature of the shape memory alloy wire actuator a
T_{ij}	i, j-th component of the Biot stress tensor
T_R	shape memory alloy reference transformation temperature
T_∞	ambient temperature
V	volume
X_i	undeformed position along direction i, $i = \{1, 2, 3\}$
$(X_i)_k$	undeformed position of node k along direction i, $i = \{1, 2, 3\}$
${}^{b_i}\mathbf{f}_{b_1,b_2}$	vector of loads acting on body b_i, $i = \{1, 2\}$, due to the contact between bodies b_1 and b_2
$\mathbf{i}_i$	basis (unit) vector along direction i, $i = \{1, 2, 3\}$
$\mathbf{m}$	shape memory alloy transformation direction vector
$\boldsymbol{n}$	unit vector outward normal to the (ξ_1, ξ_2) admissible space
$\hat{\mathbf{n}}$	unit vector outward normal to the target surface of a contact pair
$\mathbf{r}$	position vector
$\tilde{\mathbf{r}}$	skew-symmetric matrix constructed from the vector $\mathbf{r}$
$\mathbf{r}_{a,b}$	relative position vector of a with respect to b
$\hat{\mathbf{r}}_{a,b}$	unit vector pointing from a to b
$\hat{\mathbf{s}}$	unit vector tangent to the target surface of a contact pair
$\boldsymbol{t}$	unit vector tangent to the (ξ_1, ξ_2) admissible space
$\mathbf{u}$	vector of nodal degrees of freedom
$\mathbf{u}^{(e)}$	vector of nodal degrees of freedom of element e
$\dot{\mathbf{u}}_{b_2,b_1}$	relative velocity vector between points on the surfaces of bodies b_2 and b_1
$\dot{\mathbf{u}}_{b_i}$	velocity vector of a point at the surface of body b_i

$\mathbf{u}_{\text{system}}$	vector of system degrees of freedom
$\mathbf{x}$	position vector of a point on the contactor surface of a contact pair
$\mathbf{y}$	position vector of a point on the target surface of a contact pair
$\mathbf{y}^*$	position vector of the closest point on the target surface with respect to a point $\mathbf{x}$ on the contactor surface
B	strain-displacement matrix
B_m	residual magnetization vector related to magnet m
D	matrix containing beam stiffness coefficients
$\mathrm{F}_{a,b}$	vector of forces at magnet a due to magnet b
$\bar{\mathrm{F}}_{a,b}$	vector of forces at a differential element of volume $\mathrm{d}V_a$ that occur due to the permanent magnet b
$\left(\mathrm{F}_{a,b}\right)_i$	i-th component of the vector of forces at magnet a due to magnet b
$(\mathrm{F}_{\text{contact}})_k$	vector of contact forces at node k
$[(\mathrm{F}_{\text{contact}})_k]_c$	vector of contact forces at node k related to the contact pair c
F_{ext}	vector of externally applied loads
F_{int}	vector of material internal loads
F_m	vector of loads applied at the node related to the centroid of magnet m, due to its interaction with yet another magnet
$(\mathrm{F}_m)_p$	vector of loads applied at the node related to the centroid of magnet m of the p-th magnet pair
$(\mathrm{F}_{\text{SMA}})_k$	vector of forces applied at node k due to shape memory alloy wire actuator
$[(\mathrm{F}_{\text{SMA}})_k]_a$	vector of forces applied at node k due to shape memory alloy wire actuator a
H_m	magnetic field due to magnet m
I_3	3×3 identity matrix
$\mathbf{K}_{\text{system}}$	Jacobian matrix related to the system residual vector $\mathrm{R}_{\text{system}}$
$\mathbf{M}_{a,b}$	vector of moments at magnet a due to magnet b
$\left(\mathbf{M}_{a,b}\right)_i$	i-th component of the vector of moments at magnet a due to magnet b
$\mathbf{N}^{(e)}$	matrix of shape functions for element e
R	residual vector

$\mathrm{R}_{\mathrm{system}}$	system-level residual vector
R_{ξ}	residual equations related to ξ
$\left(\mathrm{R}_{\xi}\right)_{a}$	residual equations related to ξ of the a-th shape memory alloy wire actuator
$\mathbb{R}$	set of real numbers
S	vector of beam internal loads per unit length
T	vector of temperatures of all shape memory alloy wire actuators

SUMMARY

CHAPTER I

INTRODUCTION

1.1 Background and Motivation

Morphing aircraft have been intensively studied lately, as is shown by several recent literature reviews on the subject (RODRIGUEZ, 2007; THILL et al., 2008; BARBARINO et al., 2011b; GOMEZ; GARCIA, 2011; LACHENAL; DAYNES; WEAVER, 2013; WEISSHAAR, 2013; BARBARINO et al., 2014; DAYYANI et al., 2015; EMAM; INMAN, 2015; SUN et al., 2016). The term refers to aircraft whose geometry can be modified as demanded, usually trying to achieve better performance, greater maneuverability, improved fuel consumption, etc. Insects, birds and bats are some of the animals that have made mankind pursue sustained flight, and motivated the search for novel approaches in aircraft design, based on bio-inspiration, such as morphing technologies (VALASEK, 2012).

Structural reconfiguration in aircraft can be seen nowadays in the form of flaps, slats, and ailerons, for example. These are for the most part adopted for achieving high-lift configurations during take-off and landing; or to allow for roll control and/or stabilization of the aircraft. More unconventional approaches can also be listed, such as variable wing sweep, as implemented in the F-14 Tomcat, among other aircraft, which is adopted to allow for flight both at low and high speeds; and tilting rotors, as seen in the Bell Boeing V-22 Osprey, which enable vertical take-off and landing, while simultaneously allowing for the long-range, high-speed cruise performance of a turboprop aircraft.

Table 1.1 summarizes the effects that result from geometric modifications adopted during aircraft wing design. It can be seen that airfoil camber morphing allows for the modification of the zero-lift angle of attack; the airfoil aerodynamic efficiency (i.e. the ratio between lift and drag); and the behavior of flow separation. Furthermore, if camber morphing is implemented at distinct sections along the wing span, differential camber morphing could imply in modifications of the wing torsion distribution, thus effectively enabling control of the lift distribution of the wing. Ideally, elliptical lift distribution could be achieved, so as to minimize induced drag, during the whole mission profile of the morphing aircraft, if energy efficiency is to be

Table 1.1 – Effects of wing geometry on aircraft performance (JHA; KUDVA, 2004)

Parameter	Variation	Resulting effects, with other parameters unchanged
Wing plan area	↑	Increased lift and load factor capability
	↓	Decreased parasitic drag
Wing aspect ratio	↑	Increased L/D, loiter time, cruise distance and turn rates; Decreased engine requirements
	↓	Increased maximum speed; Decreased parasitic drag
Wing dihedral	↑	Increased rolling moment capability and lateral stability
	↓	Increased maximum speed
Wing sweep	↑	Increased critical Mach number and dihedral effect; Decreased high-speed drag
	↓	Increased $C_{L,\max}$
Wing taper ratio	↑↓	Wing efficiency (span-wise lift distribution) and induced drag can be reduced/increased
Wing twist distribution	↑↓	Tip stall can be prevented and span-wise lift distribution can be tailored
Airfoil camber	↑↓	Zero-lift angle of attack and airfoil efficiency can be increased/decreased; separation behavior can be improved/worsen
Airfoil thickness/chord ratio	↑	Improved low-speed airfoil performance
	↓	Improved high-speed airfoil performance
Leading edge radius	↑	Improved low-speed airfoil performance
	↓	Improved high-speed airfoil performance
Airfoil thickness distribution	↑↓	Airfoil characteristics and laminar/turbulent transition can be improved/worsen

pursued. Because of these outcomes, camber morphing is indeed the most researched aspect amidst the morphing aircraft literature (BARBARINO et al., 2011b).

Nevertheless, morphing aircraft have not taken over traditional aircraft designs, despite the huge benefits they provide. This comes, in part, from designs that have been highly optimized during the previous decades by aircraft manufacturers. Another reason for morphing aircraft designs not being adopted at this time is related to penalties this technology actually poses (WEISSHAAR, 2013; FRISWELL, 2014). For instance, increased weight and costs might be observed due to the requirement of additional actuation systems, and structural rearrangements. Complying with this, the morphing technology might be advantageous mostly, or even only, in conditions for which conflicting and/or multiple requirements are to be met by the aircraft, as shown in Fig. 1.1.

To tackle the weight issue that naturally arises in morphing aircraft, the so-called smart materials can be useful. These are able to convert energy from one physical domain to another, and, as long as one of these domains is the mechanical one, they can be adopted as sensors and/or actuators (LEO, 2007). Examples include piezoelectric materials, that exhibit electromechanical coupling; and shape memory alloys (SMAs), which are characterized by their thermomechanical nature. Smart materials can be adopted to enhance traditional mechanical designs by enabling embedded sensing and actuation, for example, and therefore lead to compact sys-

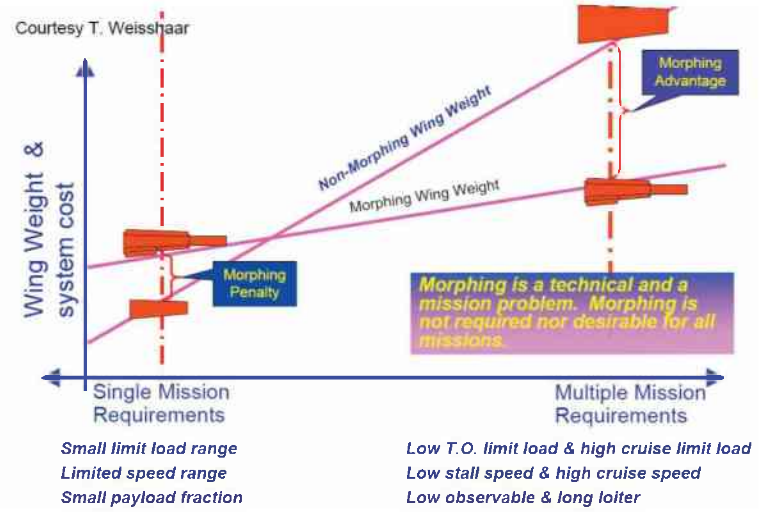

Figure 1.1 – Wing weight and cost versus aircraft mission requirements (MCGOWAN, 2007)

tems. Furthermore, smart material actuators usually can be designed so as to bear structural loads, and thus promote an overall weight minimization for the system in which they are integrated. As reported in the literature review by Barbarino et al. (2011b), smart material actuators are, if not mandatory, the most promising approach for enabling morphing aircraft technologies.

SMAs, in particular, have been adopted in numerous applications related to morphing aircraft (BARBARINO et al., 2014). This class of materials have also been largely adopted in the biomedical (MACHADO; SAVI, 2003; MORGAN, 2004; PETRINI; MIGLIAVACCA, 2011), aerospace (HARTL; LAGOUDAS, 2007), and robotics (KHEIRIKHAH; RABIEE; EDALAT, 2010) research fields. Broader review publications on the subject of SMA actuators can also be found (NESPOLI et al., 2010; MOHD JANI et al., 2014; CISSE; ZAKI; ZINEB, 2016a; CISSE; ZAKI; ZINEB, 2016b).

Table 1.2 summarizes the main characteristics related to SMAs, and also points out to direct consequences related to their engineering application. Table 1.3, on the other hand, compares the characteristics of several actuators adopted in engineering applications, including SMAs and piezoelectric materials. When the data given in this table is considered, it becomes clear that NiTi SMAs are the obvious choice when actuators that provide significant displacement and forces are needed, with no critical requirements for a short response time or high efficiency (MOHD JANI et al., 2014).

In this respect, specially when morphing applications are considered, the poor energetic efficiency of SMAs can be particularly troublesome. As Barbarino et al. (2014) point out, system-level benefits provided by morphing technologies should be expected as long as power consumption can be kept low. In this regard, avoiding continuous actuation of an SMA material consists in an interesting strategy, if this is indeed possible from an operational point of view. Following this reasoning, the adoption of a multistable SMA actuation arrangement can lead to significant benefits in terms of energy savings, while still allowing the system to assume distinct configurations.

In fact, several morphing aircraft research have adopted the use of multistable structures. For the most part, they rely on bistable laminated composites that are actuated by piezoelec-

Table 1.2 – Summary of various SMA properties and their effects (HARTL; LAGOUDAS, 2007)

SMA traits	Consequences
Shape memory effect	Material can be used as an actuator, providing force during shape recovery
Pseudoelasticity	Material can be stressed to provide large, recoverable deformations at nearly constant stress levels
Hysteresis	Allows for dissipation of energy during pseudoelastic response
High actuation stress (400–700 MPa)	Small component cross-sections can provide substantial forces
High actuation strain (8%)	Small component lengths can provide large displacements
High energy density (~1200 J/kg)	Small amounts of material required to provide substantial actuation work
Three-dimensional actuation	Polycrystalline SMA components fabricated in a variety of shapes, providing a variety of useful geometric configurations
Actuation frequency	Difficulty of quickly cooling components limits use in high frequency applications
Energy efficiency (10–15%)	Amount of thermal energy required for actuation is much larger than mechanical work output
Transformation-induced plasticity	Plastic accumulation during cyclic response eventually degrades material and leads to failure

tric materials (DIACONU; WEAVER; MATTIONI, 2008; MATTIONI et al., 2008b; ARRIETA; WAGG; NEILD, 2011; LEE; MOOSAVIAN; INMAN, 2017) or SMA actuators (LEE et al., 2014). In these cases, multistability arises due to unsymmetric lay-up patterns; or results from residual stresses that are introduced during the manufacturing process of the composite part (HUFENBACH; GUDE; KROLL, 2002; DAYNES; POTTER; WEAVER, 2008; MATTIONI et al., 2008a).

Table 1.3 – Comparison of actuator performance (MOHD JANI et al., 2014)

Actuator type	Stress [MPa]	Strain [%]	Efficiency [%]	Bandwidth [Hz]	Work per Volume [J/cm^3]	Power per Volume [W/cm^3]
NiTi SMAs	200	10	3	3	10	30
Piezoceramics	35	0.2	50	5000	0.035	175
Single crystal piezoelectric	300	1.7	90	5800	2.55	15000
Human muscle	0.007–0.8	1–100	35	2–173	0.035	0.35
Hydraulic	20	50	80	4	5	20
Pneumatic	0.7	50	90	20	0.175	3.5

Another means for achieving multistability consists in the use of permanent magnets, as previously demonstrated in the literature (ZHAO et al., 2013; ZHAO et al., 2014a; ZHAO et al., 2014b; ZHAO et al., 2015). Permanent magnets already have been adopted in other smart material-related applications, more prominently in vibration energy harvesters (KARAMI; VAROTO; INMAN, 2011; AVVARI et al., 2013; HARNE; WANG, 2013; PELLEGRINI et al., 2013; KIM; SEOK, 2014). Their use in providing multistability allows for structure simplicity, since multiple equilibrium configurations can be achieved within the structural range of motion through nonlinear magnetic-mechanical interactions (ZHAO et al., 2015).

When it comes to SMA actuated systems for morphing aircraft applications, multistability has been adopted while considering bistable structural arrangements, as reported by Barbarino et al. (2014). To this author's best knowledge, multistability driven by permanent magnets combined with SMA actuation has been considered previously only in applications such as microvalves, microswitches and microactuators (BARTH; KOHL, 2010; BARTH; KREVET; KOHL, 2010; BARTH; MEGNIN; KOHL, 2012) and not for structural morphing purposes.

1.2 Thesis Objective and Contributions

Considering the background given previously, it is of interest, and it consists of the main objective of this Thesis, to investigate the simultaneous use of SMA wire actuators with permanent magnets so as to attain multistable smart structures, and their use for morphing applications. In this respect, the main contributions the Thesis offers are:

a) the combination of SMA actuators and permanent magnets in new geometrical arrangements to achieve multistable behavior;
b) the development of a numerical modeling procedure that is able to simulate the multiphysics nature of the studied systems;
c) the proposal of a geometric arrangement for morphing applications that is based on a repeating pattern of unit cells that incorporate the combined use of SMA wires and permanent magnets for multistability; and
d) the experimental evaluation of prototypes associated to the matter.

1.3 Organization of the Thesis

Besides this Chapter I, which introduces the background, objective, and contributions of the Thesis, seven additional ones, for which brief descriptions are provided below, make up this report.

In Chapter II, a literature review is presented, in which studies related to morphing aircraft, multistability, and SMA-based morphing airfoil concepts are discussed. A critical view about research that has already been performed is also provided, which allows for a better judgment of the contributions of the Thesis.

Chapter III covers the modeling strategies that have been adopted for numerical simulations. These encompass structural modeling through the use of the finite element method; a strategy for dealing with contact; the modeling of the thermomechanical behavior of SMA wires; and the modeling of interacting permanent magnets. The coupling of all these strategies into a single simulation framework is also discussed.

Chapters IV, V, and VI successively elaborate upon the simultaneous use of SMA actuators and permanent magnets for achieving multistable smart structures and their use in morphing applications.

First, in Chapter IV, a system comprising a cantilever beam with attached permanent magnets and antagonistic SMA wires is considered, allowing for an initial assessment of the proposed multistable arrangement. The procedures adopted for experimental tests are discussed and results are shown. Comparison between numerical and experimental responses is also performed.

Next, SMA wires and permanent magnets are employed within the design of a unit cell in Chapter V. The proposed unit cell is arranged repeatedly along the length of a beam-like structure, which is studied to assess the benefits and drawbacks of the considered approach. Experimental setups are detailed, and collected data allows for the comparison of two distinct configurations that have been tested.

In Chapter VI, a morphing airfoil whose design is based upon the beam-like structure considered in Chapter V is examined. Experimental tests are detailed, and results are given.

Conclusions are finally considered in Chapter VII. Future research directions are also addressed.

Lastly, bibliographic references are provided.

CHAPTER II

LITERATURE REVIEW

This Chapter is dedicated to a review of the literature related to the topics addressed in the Thesis. Publications dealing with morphing aircraft and multistability are considered. Focus is also given to articles that consider multistable structures actuated by SMAs. Some works that have motivated the adoption of an airfoil design based on a repeating pattern of unit cells are also addressed.

2.1 Morphing Aircraft

One starts by considering the morphing aircraft literature. Recent reviews about this matter are available and are therefore adopted for evaluation of the current research status about this subject.

Rodriguez (2007) reviews the technology that has been developed towards morphing aircraft. The author highlights the enormous efforts made by government agencies, universities and companies, both in the United States and in Europe, so as to conceive aircraft that are more efficient and able to operate under a wide range of flight conditions. The review reports on projects that have been carried out by NASA, by the Defense Advanced Research Projects Agency (DARPA), and in Europe. Studies developed in universities and companies that deal with adaptive structures and smart materials are also discussed, and include works performed at Penn State University; University of Notre Dame; Georgia Institute of Technology; University of Florida; University of Michigan; Virginia Tech; Massachusetts Institute of Technology; University of Purdue; Texas A&M University; Arizona State University; Instituto Superior Técnico, Portugal; among several others.

Morphing skins are addressed by Thill et al. (2008). According to the authors, if morphing aircraft are to be successful, then the technology associated with morphing skins must be addressed thoroughly. It is required from morphing skins that they: a) be elastic in chord-wise direction to allow for low actuation forces; b) be stiff in span-wise direction to withstand aerodynamic and inertial loads; c) possess toughness; d) be abrasion and chemical resistant; e) be resistant to different weather conditions; f) have high strain capability; g) have high strain recovery rate; and h) possess environmental longevity and fatigue resistance. Thill et al. (2008) conclude that the concepts, materials and/or structures that have already been proposed in the literature are not able to fulfill all these characteristics. It appears that the major design problem in morphing skins consists in combining flexibility and stiffness into a single structure. While pointing out for the low level of maturity of the available concepts, they suggest that morphing skins would likely be hierarchical or heterogeneous structures, and not a simple homogeneous material.

A major literature review about morphing aircraft has been performed by Barbarino et al. (2011b). The authors classify the morphing aircraft literature into three distinct categories, in accordance with the type of morphing implemented, which might be: a) wing planform morphing, which encompass variable span, variable chord and variable sweep; b) wing out-of-plane transformations, such as wing twist, dihedral, and span-wise bending; or c) airfoil adjustments, with the main contributions being related to morphing camber. Barbarino et al. (2011b) verify that, despite big efforts already devoted to morphing aircraft research, few prototypes have been tested in wind tunnels, and a smaller quantity have performed any kind of flight test. They also report on the contributions that have been and still are provided by smart materials to the morphing aircraft research studies. Piezoelectric and SMA actuators, for example, allow for new design perspectives, as they are able to provide small added mass, relatively high actuation capabilities, and distributed actuation. Still according to Barbarino et al. (2011b), difficulties arise from the multidisciplinary behavior inherent to adaptive smart structures. These should be taken into account during early design stages of morphing aircraft, and thus stand for a significant increase in complexity.

Weisshaar (2013), on the other hand, provides an interesting historical view about morphing aircraft. The author details the beginnings of flight, and argues about morphing being the solution to a problem, instead of the contrary. Developments along the 20th century are discussed, and slats and flaps are presented as successful morphing aircraft components. Examples are also given in which large-scale changes are considered, such as experimental and military aircraft that benefited from increased wing planform area for low-speed operations; and variable wing sweep, which enabled multipoint military and commercial missions. Modern morphing development through the use of smart materials is also covered, with the discussion of the NASA's Smart Structures Morphing Program (WLEZIEN et al., 1998); the DARPA Smart Materials and Smart Structures Program (SANDERS; CROWE; GARCIA, 2004); and the more recent DARPA Morphing Aircraft Structures Program (WEISSHAAR, 2006), which involved Lockheed Martin Company, NextGen Aeronautics Corporation, and Raytheon Missile Systems as participants, in an attempt to respond to defense technology objectives put forward by the USA Department of Defense. In all, the review indirectly addresses three myths related with morphing aircraft: a) morphing shape change is too expensive; b) morphing aircraft must weigh more than non-morphing aircraft; and c) morphing requires exotic materials and complex systems. Weisshaar (2013) argues there have been designs where this is true, even when the aircraft mission does not require morphing. Furthermore, according to him, history have showed, more often than not, that modern aircraft do require some features that are definitely classified as morphing. Despite some disputes related to the classification of what can and what cannot be considered as morphing technology, he concludes that, in the end, after a few decades of use, morphing will be accepted and viewed as ordinary.

Friswell (2014) presents his personal view on the developments in morphing aircraft, by considering several sensitive questions related to the matter. He ponders on: a) what is a morphing aircraft; b) what they try to achieve; c) if bio-inspiration is useful; d) if UAVs are good vehicles for development; e) what concepts might work for large aircraft; f) the emphasis given to morphing wings; g) actuation requirements; h) how morphing aircraft should be operated; i) requirements for software tools; and j) the outlook for morphing aircraft. As pointed out by him, the future of morphing aircraft is uncertain. For instance, conventional aircraft design procedures usually are more attractive than morphing, which might not have reason to be considered. Emphasis is also given to the complexity related to the integration of morphing systems onto an aircraft wing. In his conclusions, Friswell (2014) verifies that the technology readiness level is still very low, and that significant research must still be performed to tackle aspects related to skins, actuation and mechanisms, and control theory related to morphing applications.

The previous discussion allows for the following general conclusions:

a) much research still needs to be performed so that morphing aircraft technologies can be considered in aircraft designs;
b) much likely, morphing in large-scale commercial aviation will not be seen in the near future, while smaller aircraft are more solid candidates for morphing technology development and application;
c) smart materials seem to be the most researched actuators for enabling morphing technologies, for the benefits they provide; and
d) morphing technologies should be seen as an alternative strategy in aircraft design, and not a replacement for traditional approaches.

2.2 Multistability

After having gone through the main aspects related to morphing aircraft research, multistability is now considered. As will be seen, it has been adopted as a design approach in several applications.

Vangbo (1998) considers the modeling of the snap-through behavior of a double-clamped beam. The classical theory for slender beams is extended by the author so the compression effort is also taken into account. This significantly improves the model predictions of the snap-through behavior path, which might change due to the compression loads. The snapping mechanism itself can be modified, such that the maximum force is due to compression, rather than being related to the Euler critical buckling load.

Pham and Wang (2011) develop a quadristable mechanism based on a bistable structure that is embedded in a surrounding beam support structure. The authors argue that multistable mechanisms can allow for the design of systems with both power efficiency and kinematic versatility. Furthermore, a low number of mechanisms with four or more mechanically stable configurations have been reported in the literature. In the design they proposed, multistability is achieved trough the buckling of curved-beam structures that compose the mechanism. The behavior of the system is analyzed through finite element simulations for static loading conditions. A design strategy based on optimization is also presented, and prototypes are manufactured and tested, which allow to verify the effectiveness of the proposed approach. The design has no movable joints and can be miniaturized, and therefore there is potential for its application in microactuators, microsensors and micro-electromechanical systems (MEMS).

Qiu, Lang, and Slocum (2004) present a mechanically-bistable mechanism that does not rely on residual stress, and, instead, is based upon the use of two curved centrally-clamped parallel beams. The bistable behavior is explained and analyzed through modal analysis and finite element simulations of the curved beam. Fabrication of microscale prototypes is performed, which are used to validate analytical predictions. Suggestions for the improvement of the bistable behavior are also considered. Qiu et al. (2005) report on the use of this previous bistable mechanism as a MEMS relay for power applications. Attention is given to the design and modeling of the adopted U-shaped transient thermal actuators.

Lei and Yao (2010) consider the use of bistability in deployable composite shell structures, which are analyzed through experimental tests. Thin-walled carbon/epoxy and glass/epoxy composite shell structures are manufactured, and then deployable behaviors are investigated while considering the deployable process, bending moment, and flexural radius. Critical conditions for bistable behavior are discussed, and enable to verify that these are directly related to the material type, material properties and lay-ups adopted in the shell structures. Xiong, Lei, and Yao (2011) perform further analyzes in order to characterize the dynamic behavior associated with the previous deployable composite shells.

Hufenbach, Gude, and Kroll (2002) consider the design of multistable composites for application in adaptive structures. An optimization procedure is developed and experimentally tested so as to determine the laminate lay-up configuration that allows for desired curvatures. Multistability in this case is driven by unsymmetric lay-up; inhomogeneous residual stresses, which are primarily due to thermal effects; moisture absorption; and chemical shrinkage. Snap-through is observed between stable deformation states, which consists of distinct cylindrical configurations.

King et al. (2005) provide an overview on systems with multistable equilibrium configurations, their application, and their design. For this purpose, a numerical optimization synthesis methodology is proposed, which is adopted in an example system containing energy storage elements from various energy domains, including mechanical rotation, mechanical translation, and magnetism. While a simple problem has been considered as an example, the methodology can be used in more complex problems, as discussed by the authors.

The work of Daynes, Potter, and Weaver (2008) discusses bistable prestressed buckled laminates. Instead of relying on geometric non-linear behavior and thermal residual stresses, they propose a new type of bistable laminate that has a symmetric lay-up. Bistability in this case can be achieved through the manipulation of the residual stresses that happen across the width of the laminate. During manufacturing, prestress is applied to specific fibres of the laminate before curing. After cure has completed and the laminate has cooled down, prestress is removed. As a result, the specimen buckles, thereby providing two bistable cylindrical configurations. Modeling is performed to provide a better comprehension of the underlying mechanism, and morphing aircraft skins are indicated as a potential application.

Hu and Burgueño (2015) provide a review on buckling-induced smart applications. They point out that buckling and other elastic instabilities can be exploited in advantageous manners, and constitute a promising technique that has not been completely investigated. Their review classify the literature according to four aspects, which are the application purposes, the application scales, the structural prototypes, and the material prototypes. They highlight that snap-buckling instabilities can be adopted in motion related applications, such as morphing, adaptive, and deployable structures, which have been covered in the previous paragraphs to some extent.

The works related to multistability that have been reviewed thus far are based exclusively on mechanical nonlinearities, such as buckling. Although the number of sample publications analyzed is relatively small, most applications reported in the literature consider this approach for achieving mechanical multistable behavior. Still, some publications make use of permanent magnets, and are addressed in the following. The adoption of multistability in combination with smart materials is considered afterwards.

2.2.1 Multistability Driven by Permanent Magnets

Fu et al. (2007) consider a new type of electromagnetic bistable MEMS relay. Because of its bistability, such device does not consume power when actuation current is not provided. Fast response, low energy consumption, large load current and ease of fabrication and realization are reported as characteristics of the prototype, which are observed in part as a consequence of the bistability design architecture being based on an arrangement that makes use of permanent magnets.

The publication of Zhao et al. (2013) addresses a bidirectional acceleration switch that incorporates a tristable mechanism that is based upon magnetic-fields that are due to permanent magnets. It is able to meet the requirements of low energy consumption and sensing in two directions. High position accuracy and repeatability are reported, and are attributed to the use of permanent magnets in the multistability setup that has been adopted. The acceleration switch itself consists basically of an inertial mass that is anchored to two parallel elastic beams, two metal contact points, and four permanent magnets, with one embedded in the inertial mass, and the other three fixed in the surrounding case. A nonlinear model is proposed for design by considering contributions that are due to elastic, magnetic, contact and inertial forces. A prototype is manufactured and used to validate the design procedure, and tests show a good agreement between experimental data and design goals. The authors also report that fine tuning of the device can be performed by modifying the location of the magnets.

Zhao et al. (2014a) consider a multistable mechanism that is based on the use of symmetric 3D magnetic structures. The prototype adopted in their work consists of an elastic rod that supports a magnetic ring at its tip, which directly faces a cylindrical magnet that is attached to a fixed base. This design allows the triggering of multistability from all in-plane directions. Multistability itself is based upon nonlinear interactions between inertial, elastic and magnetic forces. The coupled multi-physics of the system is analyzed, and the nonlinear force behavior as a function of the beam tip displacement is obtained both numerically and experimentally. Good predictions are reported for the proposed model.

Zhao et al. (2014b) propose a large stroke pentastable mechanism that is able to switch to quadristability. In this design, the authors consider the use of beams that are capable of large deformations, which are combined with permanent magnets. The nonlinear force-displacement characteristics of the system have been obtained numerically through an analytical model, which shows good agreement with finite element and experimental results. The switch from pentastability to quadristability is only analyzed theoretically, and such capability should be possible by simply modifying the magnetization direction of moving magnets.

Zhao et al. (2015) consider large deformation multistable mechanisms that are also based on the use of permanent magnets. An accurate mathematical model is established for the analysis of the nonlinear magnetic-mechanical coupling mechanics that arise in the system considered by the authors. It consists of a rotation constrained tristable mechanism. Experimental results are used to validate the proposed modeling approach, which is in good agreement.

Multistability driven by permanent magnets has not been given much attention in the scientific literature. As reported in this Subsection, applications are relatively simple; those considered deal with a MEMS relay, and an acceleration based switch. Other works simply address modeling aspects, and then use an example mechanism in order to validate proposed approaches. Nevertheless, all works describe benefits such as simple mechanical construction, low power consumption, high repeatability, and high accuracy for the permanent magnets based multistable systems. This should encourage their use in other situations.

2.2.2 Piezoelectric Actuators and Multistability for Energy Harvesting

One type of multistable smart structure that has received great attention in the literature combines piezoelectric actuators with permanent magnets for energy harvesting. Some publications on this matter are considered next.

Karami, Varoto, and Inman (2011) perform an experimental nonlinear vibration analysis of a hybrid energy harvester. The device considers the simultaneous use of piezoelectric patches and electromagnetic principles for harvesting electrical energy from ambient vibrations. Permanent magnets are mounted in a way such that they are able to reduce the resonant frequency of the harvester, and also promote broadband operation. Mono and bistable configurations are considered. In the case of bistability, the authors report the occurrence of chaotic vibrations and limit cycle oscillations, depending on excitation levels.

Avvari et al. (2013) consider energy harvesting through the use of piezoelectric materials and by exploring nonlinear vibrations. A piezoelectric cantilever beam with a magnet at its tip with surrounding magnets is adopted in order to achieve a multistable configuration for the harvester. According to the authors, in this scenario the multistability system property provides a wider bandwidth when compared to traditional linear devices, and also an increased voltage output in relationship with several other harvesters. An optimal configuration is derived after experimental parametric studies, so that performance is increased. Magnetostatic interactions and the various nonlinear multistable system configurations are also briefly discussed.

Harne and Wang (2013) perform a review about recent research on vibration energy harvesting via bistable systems. As discussed by the authors, bistable systems are able to snap-through two equilibrium configurations, with large motion amplitude and dramatically increased power generation. Furthermore, nonlinear behavior favors broadband operation. An analytical modeling framework is presented to deal with bistable electromechanical dynamics. The review addresses proposed designs, which can be based on magnetic attraction or repulsion, or on mechanical arrangements, such as the one obtained with a clamped-clamped beam that is buckled by an axial load, or through composite laminate shells with unsymmetric layup. Challenges in these types of systems involve maintaining high-energy dynamical orbits, their consistent operation in stochastic vibratory environments, among others. Yet another review on bistable vibration energy harvesters is performed by Pellegrini et al. (2013). The authors address the same topics covered by Harne and Wang (2013), and therefore strengthen the points discussed previously.

Kim and Seok (2014) consider the dynamic modeling and the bifurcation analysis of a multistable harvester. It consists of a bimorph cantilever beam that has a soft magnet at its tip, which is surrounded by fixed magnets that are arranged in an attractive configuration. The magnetic force and moment that are exerted on the cantilever tip results highly dependent on the magnetic field induced by the external magnets. The dynamic and energetic characteristics of the multistable piezoelectric harvester are extensively examined through potential energy diagrams, and by considering numerical simulations as well. Results are compared with those available for equivalent bistable harvesters too.

As can be seen from the previous works, piezoelectric materials and permanent magnets have been extensively adopted in energy harvesters, specially when one realizes that two literature reviews discuss the matter. In these cases, multistability is desired since snap-through can allow for large amounts of harvested energy. Furthermore, nonlinear behavior is an intrinsic feature of multistability, and therefore broadband operation of harvesters is also favored. In conclusion, it can be said that multistable energy harvesters stand for a successful application that adopts piezoelectric materials and permanent magnets. As an outcome, they serve as inspiration for the adoption of permanent magnets in conjunction with other smart materials in other applications.

2.2.3 Shape Memory Alloys and Multistability

Several reviews dedicated to SMAs detail the advantages and disadvantages they possess when adopted as actuators. As discussed in Chapter I, SMA actuators suffer from low actuation frequency and low energy efficiency (BARBARINO et al., 2014; MOHD JANI et al., 2014). Particularly, system-level benefits due to morphing technologies are to be expected as long as power consumption can be reduced for SMA actuators. Multistability represents an interesting approach in this regard.

Ishii and Ting (2004) study the concept, analysis and design of compliant bistable mechanisms that are actuated by SMAs. As reported by the authors, compliant bistable mechanisms and SMA linear actuators have noteworthy advantages, which are preserved when they are employed together. Furthermore, some disadvantages related to SMAs can be eliminated. For instance, an SMA actuated bistable compliant mechanism does not require any external input in order to stay at one of its stable positions, and possess high repeatability in positioning, is lightweight and requires simple control algorithms. Additionally, several shortcomings of SMA actuators, such as short output stroke and small output force, are either eliminated or reduced in the proposed design. It is based upon a four-bar linkage, with a flexible link; an slider that is attached to a linear spring arranged in parallel with a SMA spring actuator; and a rocker that is treated as the system output. The bistability arises due to the flexible link used in the mechanism.

Gauthier et al. (2006) consider a multistable actuator based on magnetic SMAs. The proposed actuator works in a push-pull configuration, in which two magnetic SMA actuators act in opposition to each other. Magnetic coils are used to produce the magnetic fields needed for actuation. The system can keep stable positions when no current is passed through the referred coils as a consequence of the hysteresis associated to the magnetic SMA actuators.

Barth and Kohl (2010) adopt a novel approach in which they combine SMA microactuators with magnetic layers (ML). Because of this, a single SMA-ML component can be actuated through two distinct, intrinsic principles, and thus allows for increase functionality. The magnetic layers are produced by electroplating discs that are mounted onto the surface of microbridge structures. Two of the proposed SMA-ML microactuators are coupled in an antagonistic way, by adopting a spacer and applying prestrain to each of them. Bistability is shown when inhomogeneous magnetic fields are generated by permanent magnets near the electroplated discs. Significant performance improvement is reported with respect to the cases in which only SMA antagonistic microactuators are considered, without the introduction of ML. The novel design allows for increased bistable stroke and blocking force.

Barth, Krevet, and Kohl (2010) apply the same concept when proposing various layouts for a bistable microswitch. Antagonistic SMA actuation is supplemented with magnetic components that are able to maintain the system at its end positions when no actuation power is provided. Finite element simulations are adopted for the optimization of the ferromagnetic force in a specific design as well.

Barth, Megnin, and Kohl (2012) propose a microvalve that is also based on antagonistic SMAs for switching between its states, and magnetic layers for maintaining specific configurations during power off conditions. The layout, manufacturing and characterization of the device is considered. Bistable operation is achieved for differential pressures up to 300 kPa of N_2 gas at high flow rates.

Kim et al. (2010) consider the simultaneous use of SMA and piezoelectric smart materials for reversible actuation of bistable composites. Piezoelectric actuation is adopted to provide a rapid snap-through action between the available stable states, while SMA actuation is used to reverse this state change. Bistability is achieved through the adoption of an unsymmetric laminate. The intent in combining both actuation strategies is in oder to prevent the use of the piezoelectric actuator outside of its recommended operating range, which would be required if it was to be used to reset the system to its original stable configuration. Some degree of controllability has been observed within each of the stable configurations both for the piezoelectric and the SMA actuators.

Gall and Bolzmacher (2014) describe the design and characterization of a hybrid magnetic SMA-electromagnetic actuator for which multistability can be achieved. Precise positioning is reported, thanks to the modification of the material hysteresis curve that happens due to the arrangement promoted between the magnetic SMA and the electromagnetic actuators. Design is performed based on analytic models and numerical simulations. Application of the hybrid actuator is suggested in systems that demand precise positioning and medium frequency actuation. The authors also verify that several improvements can be performed to address energy consumption, heat transfer, and overall cost issues.

Schiepp et al. (2016) address the use of magnetic SMAs as multistable actuators in an novel airflow control valve. Multistability is obtained based on the hysteresis observed in the stress-strain relationship of the material. It is exploited in order to reduce energy losses of the valve when a specific airflow rate must be maintained.

From what has been presented, it is possible to verify that permanent magnets driven multistability has been integrated with SMA actuators in very few circumstances, which have been reported as successful. Other multistability works that adopt SMA actuators are based on unsymmetrical laminates, and do so only in order to circumvent force deficiencies of piezoelectric actuators, which would be adopted single-handedly otherwise. Finally, another set of studies that have been considered rely on the use of magnetic SMAs to achieve multistability, instead of considering the use of "conventional" NiTi SMAs in a multistable system.

2.3 Multistability in Morphing Applications

After reviewing the literature related to the use of multistability across several engineering applications, focus is given to their utilization for morphing.

Schultz and Hyer (2004) consider bistable unsymmetric composite laminates that are controlled by piezoelectric macro fiber composites (MFC) as a possible morphing structure. The MFC actuators are adopted to enable the snap-through between the stable configurations of the composite. Experimental tests are performed and used to validate two distinct modeling strategies, one of which is based on the Rayleigh-Ritz technique, while the other adopts the ABAQUS® finite element software package. Agreement between the modeling strategies is good, but the authors report that the Rayleigh-Ritz strategy is not able to predict certain aspects captured by the finite element code modeling. For instance, actuation voltage levels necessary for snap-through are under predicted.

Portela et al. (2008) report on a novel morphing structure concept, which is studied by making use of non-linear finite element analysis. The authors consider bistable unsymmetric laminates which are snapped between its stable configurations through MFC actuation. Finite element analysis was adopted to predict the stable configurations of the structure, for understanding the buckling mechanism associated with the snap-through phenomenon, and to evaluate the use of MFCs as viable actuators for switching between stable states. The authors conclude that it is difficult to design an MFC-based actuator that can switch the laminate in both directions between its stable configurations, mainly because of the low force provided by the actuator.

Diaconu, Weaver, and Mattioni (2008) investigate concepts for morphing airfoil sections that make use of bistable laminated composite structures. Thermal curing is used to induce residual stresses into unsymmetric laminates for this purpose. Authors consider three concepts for achieving morphing of a flap-like structure, as well as camber and chord morphing of an airfoil section. Nonlinear finite element static analysis is considered in the investigation they perform, which considers several geometries and laminate configurations. Manufacturability aspects related to the production of viable morphing mechanisms within the airfoil section are also discussed. The bistability phenomenon associated with the concepts is reported as an advantage. Additional locking mechanisms are suggested in order to tackle the high compliance of the investigated concepts and the loads that are typically required in most practical applications. No particular actuation device is considered in the publication, but suggestions are given towards the use of piezoelectric devices, SMAs, and electrical drives.

Mattioni et al. (2008a) perform the analysis of thermally induced multistable composites. Finite element modeling is considered for the investigation of the effects that thermal stresses have on the potential multiple shapes of unsymmetric laminates. A methodology that allows for the computation of both stable branches in static analyses is proposed.

Mattioni et al. (2008b) consider three concepts for morphing aircraft based on multistable structures, namely a variable sweep wing, bistable blended winglets, and a variable camber trailing edge. All of the concepts benefit from unsymmetric laminates to achieve bistability. Experiments and numerical simulations are performed. The authors also address that, in principle, it is possible to achieved $2N$ stable configurations if N bistable components are combined. Nevertheless, unpredictable interactions could arise between each stable state, and so caution should be taken when multistable structures are considered.

Mattioni, Weaver, and Friswell (2009) consider the modeling of the nonlinear out-of-plane displacements related to partially unsymmetric laminates by using finite elements and an analytical method. The effects of thermal stresses on the structural behavior is addressed. A square plate is adopted as an example. Experimental tests and finite element results are used to validate the simplified modeling strategy. Investigations that consider parametric variation of the fibres orientation and laminate thickness are also performed. Authors claim that the introduction of bistable composites within structures allow for systems that are both flexible and stiff, depending on the loading environment.

Arrieta, Wagg, and Neild (2011) address the dynamic snap-through for morphing of bistable composite plates. The authors consider how the actuation system can benefit from external vibration energy in order to switch between stable states. This becomes interesting when MFC actuators are adopted, since they usually require high voltage levels to achieve significant control authority. When help is provided, lower voltages can be adopted for actuation, or stiffer laminates can be considered. Two distinct laminates are tested, and enable the authors to show that significant reduction can be achieved for the force that is required to change between stable configurations when dynamic excitation is used to assist the process led by an MFC actuator. Potential is shown for the adoption of such strategy in morphing bistable composites.

Arrieta et al. (2014) consider passive load alleviation in an airfoil concept developed based on multistable composites. The airfoil has a rigid front end, and a compliant trailing edge, in which a variable stiffness multistable element is embedded. Load alleviation can then be achieved in this cases as a consequence of the snap-through associated with the multistable laminate. The interest in such an approach is based on the fact that large loads that are due to fluid-structure interaction can lead to fatigue failure. The strategy the authors propose exploits the energy of the flow, such that load alleviation is achieved passively. The integration of the morphing laminate result in a lighter and simpler design in comparison to actively actuated solutions. For demonstration, numerical and experimental results are provided for a simple load case of the considered variable stiffness airfoil design.

Lee et al. (2014) investigate a bistable morphing panel that is actuated by a SMA spring actuator. As noticed by the authors, bistable structures are attractive in morphing applications since they are able to switch between stable configurations through an external action, and maintain one of such states without the need of continuous power supply. While most of the unsymmetric laminated bistable composites are cylindrical in shape, the authors consider a saddle-shaped bistable panel. Its mechanics are investigated through the use of the Rayleigh-Ritz method. An analytical model is developed and validated through numerical simulations based on finite elements. The proposed modeling is able to predict saddle bistability and associated deformations. The snap-through of a saddle-shaped bistable composite by an SMA spring actuator is also simulated through finite elements. Despite the simple geometry considered in their work, the authors expect that their new saddle-shaped bistable panel and the proposed morphing concept that employs an SMA spring will offer potential for new smart structures.

Lee, Moosavian, and Inman (2017) consider analytical and experimental results of bistability generated by piezoelectric, MFC actuators. In the study performed by them, two MFCs are bonded in their actuated states, and voltage is released after completion of the curing process. This allows for in-plane residual stresses, which, similar to what occur in unsymmetric laminated composites, provide for two cylindrical stable configurations. The MFCs are able to snap the structure between these. Modeling and experimental characterization are performed. As noted by the authors, the snap-through capability allows full configuration control necessary in morphing, without continuous energy input or any mechanical assistance.

By analyzing the previous references, it can be seen that multistable morphing structures promote alleviation of energetic requirements. Furthermore, only nonlinear structural phenomena has been considered so far in order to achieve multistability when it comes to morphing applications. Moreover, the vast majority of studies consider simple plate and/or shell composite laminates, their modeling, and actuation requirements. Only Mattioni et al. (2008b) and Arrieta et al. (2014) have integrated this type of structural arrangement into actual airfoil prototypes.

2.4 Shape Memory Alloy Based Morphing Airfoils, Unit Cell Designs and Metastructures

In this Section, one addresses studies that share some of the inspirations that have been considered in the design procedures proposed in this Thesis. Some publications that deal with morphing airfoils that rely on SMA actuation are also discussed, as they possess some similarities with this work.

Barbarino et al. (2009) present a morphing wing trailing edge concept. The considered design aims to replace a conventional flap. The airfoil itself consists of a compliant rib structure that is actuated by SMAs. Finite element simulations are used to obtain numerical results, which include the trailing edge displacement and the overall airfoil morphed shape. The compliant rib consists of a serial arrangement of elastic hinges along the airfoil chord, which are made of crossed thin plates. The authors mention that the rib design and functionality could be further improved.

Barbarino et al. (2011a) consider the replacement of a traditional split flap of a civil regional transportation aircraft by a hingeless, smooth morphed flap. The intention is to control the airfoil camber at the wing trailing edge. The authors present the development and testing of an actuator device based on a SMA ribbon, that is capable of rotations up to 5 degrees. An experimental flap test rig is designed and tested under static loading conditions. The prototype is built based on a serial arrangement of the previously considered SMA-based compliant actuator devices. Aero-thermo-mechanical simulations are conducted based on finite element modeling. Good correlation is reported between experimental and numerical results for the unloaded case. The authors also report that the proposed structure is extremely flexible and its elastic behavior must be taken into account during an actual design. Real applications would demand dynamic behavior analysis, including aeroelastic instabilities, which have not been performed. Barbarino et al. (2011a) also detail several possible improvements for the proposed design.

An emerging area in structural dynamics is of the so-called metastructures. These are proposed with inspiration based on metamaterials, and, due to periodic geometrical arrangements, can provide interesting behaviors in applications that aim vibration mitigation.

For instance, Chen, Hu, and Huang (2016) report about a new class of adaptive beam metastructures. Their adaptivity arise from the use of hybrid shunting circuits, which are able to realize super broadband Lamb-wave band gaps at extreme subwavelength scales. The metastructure itself comprises a a homogeneous host beam on which tunable local resonators consisting of hybrid shunted piezoelectric stacks with proof masses are attached. The shunt circuits are based on the parallel or series attachment of negative-capacitance and/or negative-inductance elements that allow for tuning of the local dynamic stiffness. High-pass and low-pass wave filtering capabilities are shown via numerical simulations, which confirm extremely broadband flexural-wave/vibration attenuation capabilities. No prototypes are built or tested.

Hobeck and Inman (2017) consider a multifunctional structural design that not only absorbs vibration at desired frequency bands, but also extracts significant amounts of electrical energy. An array of low-frequency resonators are integrated into a larger host structure, and are able to work as a distributed system of passive vibration absorbers. The authors point out that structures having these distributed vibration absorber systems are known as metastructures. Energy harvesting in this situation is possible because of the integration of piezoelectric patches in the vibration absorbers. Furthermore, low resonant frequencies are achieved for the resonators since these are based on a series of beams connected in a zigzag shape. A numerical modeling strategy is proposed, and experimental results are used to validate the adopted strategy.

Reichl and Inman (2017) consider the implementation of a control system to a longitudinal metastructure bar. The active control system is implemented by adding piezoelectric materials to one of the distributed absorbers that make up the metastructure, so as to render it active. Numerical comparisons are performed between the active and the passive metastructures.

Ueda, Secord, and Asada (2010) consider the design and analysis of piezoelectric actuators that are able to achieve 20% effective strain capabilities. An exponential strain amplification mechanism is proposed, in a “nested rombus” multilayer mechanism. The authors report on a prototype-nested PZT cellular actuator that has been constructed, and weighs only 15 g. It was able to produce 21% effective strain and a blocking force of 1.7 N.

Haghpanah et al. (2016) address multistable shape-reconfigurable architected materials. In the novel approach the authors propose, materials encompass living hinges that enable simultaneous high strength, high volumetric change, and complex shape-morphing configurations. The mechanical behavior of proposed materials is investigated both analytically and numerically, and experimental validation is also performed. As discussed by the authors, such architected materials can be made from any base material, and consider any length scale and dimensionality. The design is based on multistable structural unit cells, but actuation and/or active reconfiguration is not addressed at all.

The studies reviewed in this Section allows one to verify that new type of structures have been developed by taking metamaterials as inspiration. More specifically, repetitive geometrical arrangements have been adopted in order to allow for distributed implementation of features such as vibration absorbers and shunt electrical circuits in applications that pursue vibration attenuation. The morphing airfoils proposed by Barbarino et al. (2009) and Barbarino et al. (2011a) follow this line of reasoning to some extent, as their construction is based on distributed SMA actuators along the airfoil chord.

Because of the benefits provided by distributed actuation systems, and in special because of the possibilities for localized control, this approach is later considered in the morphing airfoil design proposed in this work.

2.5 Summary

Considering the brief review presented previously about the themes related to this Thesis, the following general comments can be made:

a) morphing aircraft research still needs to go a long way before this kind of technology can be adopted during the design of an aircraft;

b) smart materials are considered fundamental for achieving lightweight morphing concepts by some authors;

c) multistability consists of an interesting approach for enabling low energy consumption in morphing applications;

d) permanent magnets can be efficiently used in order to achieve multistable designs, that have been used in piezoelectric harvesters, MEMS relays, acceleration based switches, and other mechanisms;

e) permanent magnets have been previously coupled with SMAs in multistable microactuators, microvalves, microswitches, among others;
f) to the author's best knowledge, no morphing application has investigated the simultaneous use of permanent magnets and SMA actuators; and
g) periodic geometrical arrangements have been adopted in the proposition of metastructures, which benefit from possessing an array of integrated features, such as vibration resonators, for example.

CHAPTER III

MATHEMATICAL MODELING

In this Chapter, mathematical modeling is addressed, such that tools that have been used to perform numerical simulations are described. The type of system one is interested in has been briefly considered previously, and an schematic illustration is provided in Fig. 3.1. It possesses permanent magnets that interact between themselves, SMA wires that are used as actuators, as well as some sort of stiffness, that might be either lumped and/or distributed. Yet another modeling procedure that is also covered in this Chapter is contact simulation. The reason for considering this topic resides in the fact that the loads that happen between permanent magnets may lead to such condition — depending on the geometric arrangement of the system, of course.

The Chapter is organized as follows. First, in Section 3.1, a nonlinear beam finite element model is considered. Then a thermomechanical model for the constitutive behavior of

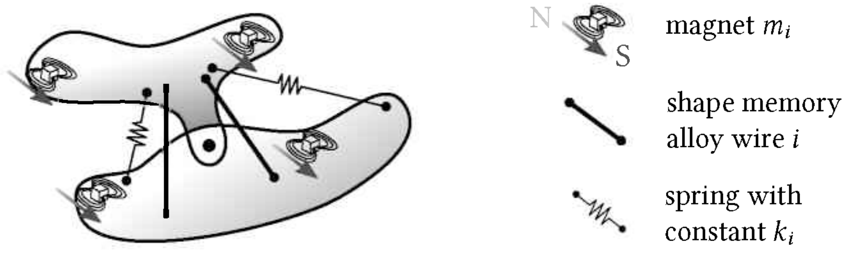

Figure 3.1 – Schematic illustration of a generic system containing permanent magnets and shape memory alloy wires

NiTi SMAs is addressed, which is directly applied to model a wire, in Section 3.2. In Section 3.3, a model for the loads developed due to the interaction between a pair of cuboidal permanent magnets is considered. The contact algorithm used during simulations is addressed in Section 3.4. Finally, in Section 3.5, the procedures used to compute the solution of the complete coupled model are presented.

3.1 Nonlinear Beam Finite Element Model

To deal with structural modeling, a 2D nonlinear beam finite element model is considered in this Thesis. It is based on the geometrically nonlinear Reissner beam theory, and further details concerning the formulation can be obtained by consulting the literature (REISSNER, 1972; WRIGGERS, 2008).

The choice for this approach is based on the geometry that is later considered in the proposed design for a morphing airfoil. Nevertheless, any other structural modeling strategy can be adopted within the framework of the solution algorithm described in Section 3.5.

First, it is important to highlight the hypotheses of the proposed model. They are as follows: a) deformations are confined to the plane on which the beam initially lies upon; b) plane cross-sections remain plane after deformation; and c) herein, initially, the beam is straight.

The beam deformation is schematically shown in Fig. 3.2. Also shown in this figure is the vector basis $(\mathbf{i}_1, \mathbf{i}_2)$, related to the beam local coordinate system. The deformed position of a point on the beam can be computed through:

$$x_1 = X_1 + u_1 (X_1) - X_2 \sin [\psi (X_1)] ; \tag{3.1}$$

$$x_2 = u_2 (X_1) + X_2 \cos [\psi (X_1)] , \tag{3.2}$$

where (X_1, X_2) are the coordinates of a material point in the reference, undeformed configuration, (x_1, x_2) are the coordinates associated with this point after deformation has occurred, and u_1, u_2, and ψ are the longitudinal, transversal, and rotational displacement fields, respectively.

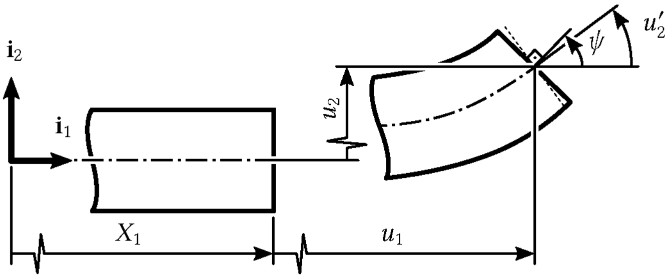

Figure 3.2 – Deformation experienced by a beam according to Reissner theory

Based on Eqs. (3.1) and (3.2), the following strain measures can be established (WRIGGERS, 2008):

$$\boldsymbol{\epsilon} = \begin{bmatrix} \epsilon \\ \gamma \\ \kappa \end{bmatrix} = \begin{bmatrix} (1+u_1')\cos\psi + u_2'\sin\psi - 1 \\ u_2'\cos\psi - (1+u_1')\sin\psi \\ \psi' \end{bmatrix}, \tag{3.3}$$

where $(\,)' \equiv \partial(\,)/\partial X_1$, and ϵ, γ, and κ are the axial strain, shear strain, and curvature, respectively.

As for the material constitutive law, a linear relationship is chosen:

$$\begin{bmatrix} T_{11} \\ T_{12} \end{bmatrix} = \begin{bmatrix} E & 0 \\ 0 & G \end{bmatrix} \begin{bmatrix} \epsilon + X_2\kappa \\ \gamma \end{bmatrix}, \tag{3.4}$$

where T_{11} and T_{12} can be seen as components of the Biot stress tensor, and E and G are the material Young's and transversal moduli, respectively. Although the beam model allows for large displacements and rotations, only small strains are assumed to occur.

Integration of the stress components along the beam cross-section leads to:

$$\begin{bmatrix} N \\ Q \\ M \end{bmatrix} = \begin{bmatrix} EA & 0 & 0 \\ 0 & GA_s & 0 \\ 0 & 0 & EI \end{bmatrix} \begin{bmatrix} \epsilon \\ \gamma \\ \kappa \end{bmatrix} \quad \Leftrightarrow \quad \mathbf{S} = \mathbf{D}\boldsymbol{\epsilon}, \tag{3.5}$$

where A and I are the cross section area, and area moment of inertia, respectively, whilst A_s is the cross section area corrected for shear effects. N, Q, and M denote the beam internal axial force, shear force, and bending moment, respectively, that result due to external loading.

Finite element discretization is performed for the u_1, u_2, and ψ displacement fields, for $0 \leq X_1^{(e)} \leq L^{(e)}$, according to:

$$\begin{bmatrix} u_1^{(e)} \\ u_2^{(e)} \\ \psi^{(e)} \end{bmatrix} = \sum_{k=1}^{n^{(e)}} \left[N_k^{(e)}\left(X_1^{(e)}\right) \mathrm{I}_3 \right] \begin{bmatrix} (u_1)_k^{(e)} \\ (u_2)_k^{(e)} \\ \psi_k^{(e)} \end{bmatrix} = \mathrm{N}^{(e)}\mathbf{u}^{(e)}, \tag{3.6}$$

where I_3 denotes the 3×3 identity matrix, $\mathrm{N}^{(e)} \in \mathbb{R}^{3 \times 3n^{(e)}}$ is the shape function matrix,

$$\mathbf{u}^{(e)} = \left[\begin{array}{ccccccc} (u_1)_1^{(e)} & (u_2)_1^{(e)} & \psi_1^{(e)} & \cdots & (u_1)_{n^{(e)}}^{(e)} & (u_2)_{n^{(e)}}^{(e)} & \psi_{n^{(e)}}^{(e)} \end{array} \right]^{\mathrm{T}} \tag{3.7}$$

is the element nodal degrees of freedom vector, and $n^{(e)}$ is the number of nodes of the element. Throughout the Thesis, superscript $(\ )^{\mathrm{T}}$ is used to indicate the transpose of a matrix. Also, the superscript $(\ )^{(e)}$ is used to denote element-related quantities, and the subscript $(\ )_k$ to indicate association with node k. $L^{(e)}$ stands for the undeformed beam element length. The shape functions $N_k^{(e)}$, $k = \left\{1, \ldots, n^{(e)}\right\}$ are chosen based on the isoparametric finite element formulation (WRIGGERS, 2008).

The nonlinear algebraic equilibrium equations at the element level can be obtained after considering the Principle of Virtual Work. By adopting the total Lagrangian approach, in which the initial undeformed configuration is used as a reference, it is possible to obtain:

$$\mathrm{R}^{(e)} = \mathrm{F}_{\mathrm{int}}^{(e)} - \mathrm{F}_{\mathrm{ext}}^{(e)} = \mathbf{0}, \tag{3.8}$$

where $\mathrm{F}_{\mathrm{int}}^{(e)}$ is the vector of internal loads, owed to the stresses that develop within the material, given by:

$$\mathrm{F}_{\mathrm{int}}^{(e)} = \int_0^{L^{(e)}} \mathrm{B}^{(e)\mathrm{T}} \mathrm{S}^{(e)} \mathrm{d}X_1^{(e)}. \tag{3.9}$$

$\mathrm{S}^{(e)}$ denotes the stress resultants inside the element domain, given in Eq. (3.5), and $\mathrm{B}^{(e)} = \mathrm{B}^{(e)}\left(\mathbf{u}^{(e)}\right)$ is the strain-displacement matrix. It can be obtained if one considers the virtual variation of the strains that result from a virtual variation imposed on the displacement fields.

Starting from Eq. (3.3), and accounting for Eq. (3.6):

$$\delta\boldsymbol{\epsilon}^{(e)} = \mathbf{B}^{(e)}\delta\mathbf{u}^{(e)}. \tag{3.10}$$

On the other hand, $\mathbf{F}_{\text{ext}}^{(e)}$ accounts for the external loads, and is computed from:

$$\mathbf{F}_{\text{ext}}^{(e)} = \int_0^{L^{(e)}} \mathbf{N}^{(e)\mathrm{T}} \begin{bmatrix} n & q & m \end{bmatrix}^{\mathrm{T}} \mathrm{d}X_1^{(e)}, \tag{3.11}$$

where $n = n\left(X_1^{(e)}\right)$, $q = q\left(X_1^{(e)}\right)$, and $m = m\left(X_1^{(e)}\right)$ are the applied axial, shear, and moment distributed loads.

From the equilibrium equations established for a single element, global ones can be obtained by making use of usual methods. For instance, the vector of degrees of freedom is transformed from the local finite element coordinate system to the global inertial frame. Following this step, element connectivity can be considered for direct assembly of the global equations.

More in-depth details of the formulation and its implementation aspects are provided by Wriggers (2008). Although inertial effects have been disregarded, they can be easily accounted for in the adopted modeling approach.

3.2 Shape Memory Alloy Thermomechanical Model

Complete modeling of the behavior of SMAs is rather challenging, since several details must be faced altogether, such as temperature and stress-induced martensite transformations, stress induced martensite reorientation, transformation-induced plasticity, load rate dependency, etc. (PAIVA; SAVI, 2006; LAGOUDAS et al., 2012; AURICCHIO et al., 2014). Even when dealing with wire actuators, unusual behavior such as transformation-front propagation phenomena can arise, as reported by Chang, Shaw, and Iadicola (2006).

Here, a model that considers only the most relevant of such aspects is selected, in favor of simplicity. It is based on the articles by Chang, Shaw, and Iadicola (2006) and Shaw and Churchill (2009), which can be consulted for more in-depth details and discussion. It is able to represent both shape memory effect, and pseudo-elastic behaviors.

An SMA wire actuator is considered, for which gradients along its length are neglected. The specific Helmholtz free energy is assumed to be given by:

$$\begin{aligned}\phi\left(\epsilon,\boldsymbol{\xi},T\right) = \left(2\rho\right)^{-1}\left[E_A + \left(\xi_1+\xi_2\right)\left(E_M - E_A\right)\right]\left[\epsilon - \left(\xi_1-\xi_2\right)\beta\right]^2 - \left(T - T_R\right)\left(\xi_1+\xi_2\right)\Delta s \\ + c_I\left(1-\xi_1-\xi_2\right)\left(\xi_1+\xi_2\right) + \left(c_0 - s_0\right)\left(T-T_R\right) - c_0\ln\left(T/T_R\right), \quad (3.12)\end{aligned}$$

where $\epsilon = \epsilon\left(t\right)$ is the strain, $\xi_1 = \xi_1\left(t\right)$ and $\xi_2 = \xi_2\left(t\right)$ are the volumetric phase fractions of tensile and compressive martensite variants, respectively, $T = T\left(t\right)$ is the temperature, and t denotes time. The material parameters are the specific mass ρ, the austenite and martensite stiffness moduli E_A and E_M, respectively, the stress-free transformation strain β, the reference transformation temperature T_R, the specific entropy change from austenite to martensite $\Delta s \equiv s_M - s_A$, and the constant c_I, which controls hardening during phase transformation. Finally, c_0 and s_0 are the initial state reference specific heat and specific entropy, respectively.

Based on Eq. (3.12), the stress-strain law can be obtained as:

$$\sigma = \frac{1}{\rho}\frac{\partial\phi}{\partial\epsilon} = E\left(\boldsymbol{\xi}\right)\left[\epsilon - \left(\xi_1-\xi_2\right)\beta\right], \tag{3.13}$$

where $E\left(\boldsymbol{\xi}\right) = E_A + \left(\xi_1+\xi_2\right)\Delta E$, with $\boldsymbol{\xi} = \left[\begin{array}{cc}\xi_1 & \xi_2\end{array}\right]^{\mathrm{T}}$, and $\Delta E = E_M - E_A$.

Moreover, the thermodynamic driving forces can be obtained from:

$$\mu_1 = -\frac{\partial\phi}{\partial\xi_1} = \frac{\beta\sigma}{\rho} - \frac{\Delta E}{2\rho}\left[\frac{\sigma}{E\left(\boldsymbol{\xi}\right)}\right]^2 + \left(T-T_R\right)\Delta s - c_I\left(1-2\xi_1-2\xi_2\right); \tag{3.14a}$$

$$\mu_2 = -\frac{\partial\phi}{\partial\xi_2} = -\frac{\beta\sigma}{\rho} - \frac{\Delta E}{2\rho}\left[\frac{\sigma}{E\left(\boldsymbol{\xi}\right)}\right]^2 + \left(T-T_R\right)\Delta s - c_I\left(1-2\xi_1-2\xi_2\right). \tag{3.14b}$$

To comply with the Second Law of Thermodynamics, a piecewise linear kinetic law is chosen for $\boldsymbol{\xi}$, such that:

$$\dot{\boldsymbol{\xi}} \equiv \frac{\mathrm{d}\boldsymbol{\xi}}{\mathrm{d}t} = \begin{cases} v_0\left(\boldsymbol{\mu}^{\mathrm{T}}\mathbf{m} - \mu_c\right)\mathbf{m} & \text{if } \boldsymbol{\mu}^{\mathrm{T}}\mathbf{m} > \mu_c; \\ 0 & \text{otherwise,}\end{cases} \tag{3.15}$$

where $\boldsymbol{\mu} = \left[\begin{array}{cc}\mu_1 & \mu_2\end{array}\right]^{\mathrm{T}}$, and μ_c is a critical value for the thermodynamic driving force, based on which hysteretic phase transformation takes place. The parameter v_0 can be used to control the speed with which transformation occurs. Furthermore, the vector $\mathbf{m}$ gives the direction along which transformation happens in the (ξ_1, ξ_2) space. It is defined according to the following (CHANG; SHAW; IADICOLA, 2006):

$$\text{If } \xi_i > 0 \text{ for } i = \{1,2,3\}: \quad \mathrm{m} = \boldsymbol{\mu}/\|\boldsymbol{\mu}\|; \tag{3.16a}$$

$$\text{If } \xi_i = 0 \text{ for a single } i: \qquad \mathrm{m} = \begin{cases} \boldsymbol{\mu}/\|\boldsymbol{\mu}\| & \text{if } \boldsymbol{\mu}^{\mathrm{T}}\boldsymbol{n}^{(i)} < 0; \\ \boldsymbol{t}^{(i)} & \text{otherwise}; \end{cases} \tag{3.16b}$$

$$\text{If } \xi_i = \xi_j = 0 \text{ for } i \neq j: \qquad \mathrm{m} = \begin{cases} \boldsymbol{\mu}/\|\boldsymbol{\mu}\| & \text{if } \boldsymbol{\mu}^{\mathrm{T}}\boldsymbol{n}^{(i)} < 0 \wedge \boldsymbol{\mu}^{\mathrm{T}}\boldsymbol{n}^{(j)} < 0; \\ \boldsymbol{t}^{(k)} & \text{if } \boldsymbol{\mu}^{\mathrm{T}}\boldsymbol{n}^{(k)} \geq 0 \wedge \boldsymbol{\mu}^{\mathrm{T}}\boldsymbol{t}^{(k)} > 0 \text{ for } k = \{i,j\}; \\ 0 & \text{otherwise}, \end{cases} \tag{3.16c}$$

where $\xi_3 = 1 - \xi_1 - \xi_2$ represents the austenite volumetric phase fraction, $\|\ \|$ denotes the Euclidean norm, and $\boldsymbol{n}^{(i)}$ and $\boldsymbol{t}^{(i)}$ are unit vectors that are outward normal and tangent to the admissible space for (ξ_1, ξ_2), respectively. Figure 3.3 shows these vectors when they are to be used in Eq. (3.16c). As can be seen, the direction of $\boldsymbol{t}^{(i)}$ depends on which values of i and j satisfy the condition $\xi_i = \xi_j = 0$. In contrast, when Eq. (3.16b) is considered, the direction of $\boldsymbol{t}^{(i)}$ must be chosen such that $\boldsymbol{\mu}^{\mathrm{T}}\boldsymbol{t}^{(i)} \geq 0$.

Model completeness still requires additional equations. The first one is related to mechanical equilibrium, and is considered later in Section 3.5. The second is established based on the energy conservation principle. One assumes that the SMA wire actuator has an initial

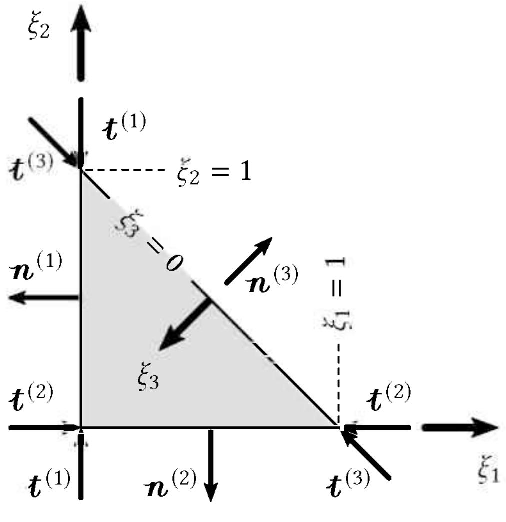

Figure 3.3 – Admissible (ξ_1, ξ_2) space, and corresponding $\boldsymbol{n}^{(i)}$ and $\boldsymbol{t}^{(i)}$ vectors

(undeformed) length L_0 and diameter d_0. In deriving the rate equation for T, it is assumed that these remain constant (CHANG; SHAW; IADICOLA, 2006; SHAW; CHURCHILL, 2009). It holds that:

$$\rho c_0 A_0 L_0 \dot{T} = \rho A_0 L_0 \left(\boldsymbol{\mu} - T\, \partial \boldsymbol{\mu}/\partial T\right)^{\mathrm{T}} \dot{\boldsymbol{\xi}} - h \pi d_0 L_0 \left(T - T_\infty\right) + P_E, \tag{3.17}$$

where $A_0 = \pi d_0^2/4$, h is the convective film coefficient, T_∞ is the ambient temperature, and P_E is the power input term. The wire is assumed to be heated through Joule effect.

3.3 Interacting Permanent Magnets Model

Analytical equations have been reported in the literature for the calculation of forces and moments that result from interacting permanent magnets. Usually, cylindrical (VOKOUN; BELEGGIA; ŠITTNER, 2009) or rectangular-parallelepiped (ALLAG; YONNET, 2009) geometry is assumed for the magnets. In the latter case, loads can be computed for arbitrary magnetization directions if the concerned magnets have parallel sides, for example.

While this is useful in several circumstances, when moving magnets are considered, they are likely to experience change in orientation. In this case, closed-form analytical solutions for the loads are not available, and must be pursued numerically (MONTALVO, 2014).

Figure 3.4 shows two magnets, labeled as magnets m_1 and m_2. Three different coordinate frames can be identified by their respective vector basis (${}^{g}\mathbf{i}_i$, ${}^{m_1}\mathbf{i}_i$, ${}^{m_2}\mathbf{i}_i$, with $i = \{1, 2, 3\}$), each one of them related either to the global, magnet m_1, or magnet m_2 systems of reference. While the origin of the global frame is arbitrary, the origins of the reference frames related to the magnets are coincident with their respective centroids. Herein, left superscripts are used to identify the coordinate system in which vector coordinates are expressed. Hypotheses related to the formulation are that magnets are rigid, and their residual magnetizations have constant amplitude and direction with respect to the local auxiliary coordinate frames.

Figure 3.4 also identifies the rotation matrices ${}^{m_1}\Phi^{g}$ and ${}^{m_2}\Phi^{g}$, based on which coordinate transformation can be performed for the components of a vector between the global and auxiliary frames. Vectors $\mathbf{r}_{m_1}$ and $\mathbf{r}_{m_2}$ represent the positions occupied by the centroids of magnets

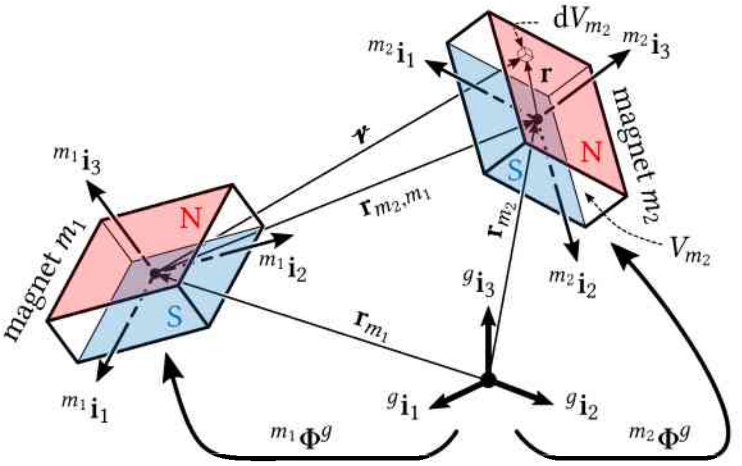

Figure 3.4 – Schematic representation for the interaction between two rectangular-parallelepiped-shaped magnets

m_1 and m_2, respectively, with respect to the global frame origin; $\mathbf{r}_{m_2,m_1}$ represents the relative position of the centroid of m_2 with respect to the centroid of m_1; and $\mathbf{r}$ is the position occupied by a differential element of volume dV_{m_2} with respect to the centroid of magnet m_2.

Along this Section, subscripts $(\,)_{m_1}$ and $(\,)_{m_2}$ are used to relate quantities to the magnets m_1 and m_2, respectively. Not shown in the Fig. 3.4 are the dimensions of the two magnets, defined as $2(l_1)_{m_1}$, $2(l_2)_{m_1}$, and $2(l_3)_{m_1}$, along the directions $^{m_1}\mathbf{i}_1$, $^{m_1}\mathbf{i}_2$, and $^{m_1}\mathbf{i}_3$, respectively, for magnet m_1, and similarly for magnet m_2, by replacing the m_1 in the subscripts and left superscripts by m_2.

To derive expressions for the forces and moments resulting from the interaction between the two magnets, it is first noted that the force acting on the differential element of volume dV_{m_2} of magnet m_2, due to the magnetic field of magnet m_1, can be evaluated through:

$$ {}^{m_1}\bar{\mathbf{F}}_{m_2,m_1} = {}^{m_1}\boldsymbol{\nabla}\left({}^{m_1}\mathbf{B}_{m_2}^{\mathrm{T}}\;{}^{m_1}\mathbf{H}_{m_1}\right), \tag{3.18} $$

where $\mathbf{B}_{m_2}$ is the residual magnetization vector of magnet m_2, $\mathbf{H}_{m_1}$ is the magnetic field produced by magnet m_1, and $\boldsymbol{\nabla}(\,) = \begin{bmatrix} \partial(\,)/\partial X_1 & \partial(\,)/\partial X_2 & \partial(\,)/\partial X_3 \end{bmatrix}^{\mathrm{T}}$ is the nabla operator.

The coordinates of the residual magnetization vector of magnet m_2 are given by $^{m_2}\mathbf{B}_{m_2} = \begin{bmatrix} 0 & 0 & B_{m_2} \end{bmatrix}^{\mathrm{T}}$ in the reference frame attached to its centroid, such that B_{m_2} denotes its residual magnetization. To obtain $^{m_1}\mathbf{B}_{m_2}$, as required in Eq. (3.18), the rotation matrices $^{m_1}\Phi^{g}$ and

${}^{m_2}\Phi^{g}$ can be used:

$$ {}^{m_1}\mathrm{B}_{m_2} = \left({}^{m_1}\Phi^{g}\right)\,{}^{g}\mathrm{B}_{m_2}; \tag{3.19} $$

$$ {}^{m_2}\mathrm{B}_{m_2} = \left({}^{m_2}\Phi^{g}\right)\,{}^{g}\mathrm{B}_{m_2}; \tag{3.20} $$

$$ {}^{m_1}\mathrm{B}_{m_2} = \left({}^{m_1}\Phi^{m_2}\right)\,{}^{m_2}\mathrm{B}_{m_2} = \left({}^{m_1}\Phi^{g}\right)\left({}^{m_2}\Phi^{g}\right)^{-1}\,{}^{m_2}\mathrm{B}_{m_2}. \tag{3.21} $$

For the magnetic field vector H_{m_1}, the following analytic expression holds (YONNET; ALLAG, 2009):

$$ {}^{m_1}\mathrm{H}_{m_1} = \frac{B_{m_1}}{4\pi\mu_0} \sum_{k_1=0}^{1}\sum_{k_2=0}^{1}\sum_{k_3=0}^{1} \Big\{(-1)^{k_1+k_2+k_3} \times \\ \left[\ \ln(\bar{r}-\bar{r}_2)\quad \ln(\bar{r}-\bar{r}_3)\quad \tan^{-1}\{\bar{r}_1\bar{r}_2/(\bar{r}\bar{r}_3)\}\ \right]^{\mathrm{T}}\Big\}, \tag{3.22} $$

where $\mu_0 = 4\pi \times 10^{-7}$ N/A^2 is the vacuum permeability, B_{m_1} is the residual magnetization of magnet m_1, and:

$$ \bar{r}_1 = r_1 - (-1)^{k_1}(l_1)_{m_1}; \tag{3.23} $$

$$ \bar{r}_2 = r_2 - (-1)^{k_2}(l_2)_{m_1}; \tag{3.24} $$

$$ \bar{r}_3 = r_3 - (-1)^{k_3}(l_3)_{m_1}; \tag{3.25} $$

$$ \bar{r} = \sqrt{\bar{r}_1^2 + \bar{r}_2^2 + \bar{r}_3^2}, \tag{3.26} $$

in which the coordinates r_i, $i = \{1, 2, 3\}$, identify the location at which ${}^{m_1}\mathrm{H}_{m_1}$ is to be evaluated, and are measured with respect to the coordinate frame related to magnet m_1, as shown in Fig. 3.4. Derivatives appearing in Eq. (3.18) can be computed analytically or through a symbolic manipulation software. It should be noted that ${}^{m_1}\bar{\mathrm{F}}_{m_2,m_1}$ depends on the relative orientation of the magnets due to Eq. (3.21).

The total force and moment acting on the magnet m_2 due to magnet m_1 can then be computed via:

$$ {}^{m_1}\mathrm{F}_{m_2,m_1} = \int_{V_{m_2}} {}^{m_1}\bar{\mathrm{F}}_{m_2,m_1}\mathrm{d}V_{m_2}; \tag{3.27} $$

$$ {}^{m_1}\mathbf{M}_{m_2,m_1} = \int_{V_{m_2}} {}^{m_1}\tilde{\mathrm{r}}\ {}^{m_1}\bar{\mathrm{F}}_{m_2,m_1}\mathrm{d}V_{m_2}, \tag{3.28} $$

where $\tilde{\mathbf{r}}$ is the skew-symmetric matrix assembled from the components r_i, $i = \{1, 2, 3\}$, of the vector $\mathbf{r}$, shown in Fig. 3.4, such that:

$$\tilde{\mathbf{r}} = \begin{bmatrix} 0 & -r_3 & r_2 \\ r_3 & 0 & -r_1 \\ -r_2 & r_1 & 0 \end{bmatrix}. \tag{3.29}$$

Integrals shown in Eqs. (3.27) and (3.28) can be evaluated using Gauss-Legendre quadrature. These are easier to evaluate in the magnet m_2 coordinate system, as in this case the orientation of the volume of integration is coincident with the frame directions. In this approach, for the computation of ${}^{m_1}\bar{\mathrm{F}}_{m_2,m_1}$, it is necessary to evaluate the vector:

$${}^{m_1}\boldsymbol{r} = {}^{m_1}\mathbf{r}_{m_2,m_1} + {}^{m_1}\mathbf{r} = {}^{m_1}\mathbf{r}_{m_2,m_1} + \left({}^{m_1}\Phi^g\right)\left({}^{m_2}\Phi^g\right)^{-1}\,{}^{m_2}\mathbf{r}, \tag{3.30}$$

whose components are needed for computing Eqs. (3.23) – (3.25).

After evaluation of ${}^{m_1}\mathrm{F}_{m_2,m_1}$ and ${}^{m_1}\mathbf{M}_{m_2,m_1}$, coordinate transformation can be performed so these loads can be expressed in the global coordinate system. Additionally, loads acting on magnet m_1 can be obtained by using:

$$\mathrm{F}_{m_1,m_2} = -\mathrm{F}_{m_2,m_1}; \tag{3.31}$$

$$\mathbf{M}_{m_1,m_2} = -\mathbf{M}_{m_2,m_1}. \tag{3.32}$$

The formulation described previously considers that permanent magnets interact in pairs. If more than two magnets are to be accounted for, the total loads that result from their interactions can be obtained by assuming linear superposition.

3.4 Finite Element Node-to-Element Contact Model

To account for contact conditions during simulations, an algorithm that deals with the case of node-to-element contact, based on inequality constraint functions, has been considered. Complete formulation can be found in Eterovic and Bathe (1991) and Bathe and Bouzinov (1997).

Figure 3.5 shows some useful information for the contact problem. The vector ${}^{b_2}\mathbf{f}_{b_1,b_2}$ contains the loads due to the surface tractions that happen on body b_2 due to the contact between bodies b_1 and b_2. The loads on body b_1 are denoted by the vector ${}^{b_1}\mathbf{f}_{b_1,b_2}$, such that ${}^{b_1}\mathbf{f}_{b_1,b_2} = -\left({}^{b_2}\mathbf{f}_{b_1,b_2}\right)$. Notice that, contrary to the notation that was adopted in the previous Section, left superscripts are now used to indicate the body at which a load vector is applied to.

It is compelling to express ${}^{b_2}\mathbf{f}_{b_1,b_2}$ through its normal and tangent contributions as follows:

$$
{}^{b_2}\mathbf{f}_{b_1,b_2} = \lambda\hat{\mathbf{n}} + \tau\hat{\mathbf{s}}, \tag{3.33}
$$

where λ is the amplitude of the normal component of the contact force, τ is the amplitude of its tangent component, and unit vectors $\hat{\mathbf{n}}$ and $\hat{\mathbf{s}}$ are normal and tangent to the target contact surface, respectively.

The gap function g can be computed by (ETEROVIC; BATHE, 1991):

$$
g(\mathbf{x}, t) = \left[\mathbf{x} - \mathbf{y}^*(\mathbf{x}, t)\right]^{\mathrm{T}} \hat{\mathbf{n}}\left(\mathbf{y}^*(\mathbf{x}, t)\right), \tag{3.34}
$$

where $\mathbf{x}$ is the location of a point on the contactor surface ∂V_{b_2}, and $\mathbf{y}^*$ is defined as the closest location on the target surface ∂V_{b_1} with respect to the chosen point $\mathbf{x}$, i.e.:

$$
\mathbf{y}^* = \arg\min\left\{\|\mathbf{x} - \mathbf{y}\| : \mathbf{y} \in \partial V_{b_1}\right\}. \tag{3.35}
$$

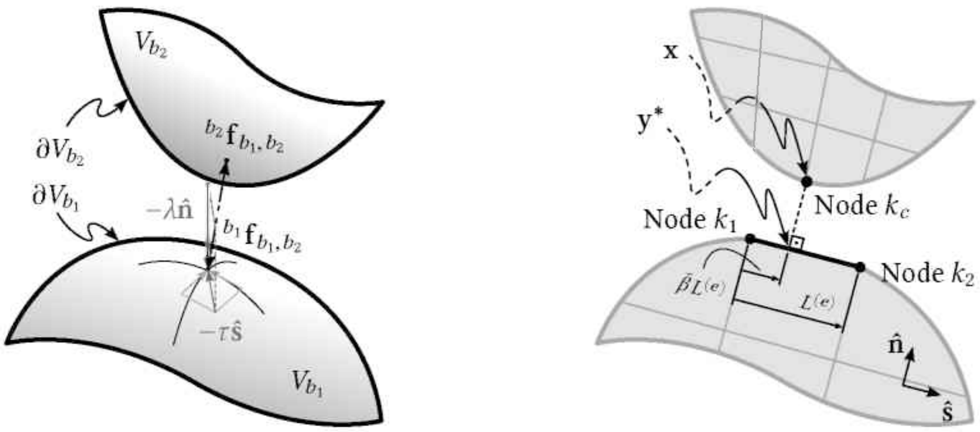

Figure 3.5 – Contact problem loads and geometry

Based on Eqs. (3.33) and (3.34), normal contact conditions can be expressed by means of the following constraints:

$$g \geq 0 \quad : \quad \text{there must be no surface inter-penetration;} \tag{3.36}$$

$$\lambda \geq 0 \quad : \quad \text{contact must imply a compressive normal load;} \tag{3.37}$$

$$g\lambda = 0 \quad : \quad \text{there must be either some gap with null } \lambda\text{, or no gap with } \lambda \neq 0. \tag{3.38}$$

Friction during contact can be considered by means of Coulomb's law. One introduces the normalized variable $\bar{\tau} \equiv \tau / (\bar{\mu}\lambda)$, where $\bar{\mu}$ is the (dynamic) coefficient of friction between the surfaces ∂V_{b_1} and ∂V_{b_2}. The relative velocity $\dot{\mathbf{u}}_{b_2,b_1}$ between the contacting surfaces is obtained through:

$$\dot{\mathbf{u}}_{b_2,b_1}(\mathbf{x}, t) = \dot{\mathbf{u}}_{b_2}(\mathbf{y}^*(\mathbf{x}, t), t) - \dot{\mathbf{u}}_{b_1}(\mathbf{x}, t), \tag{3.39}$$

where $\dot{\mathbf{u}}_{b_i}$ is the velocity of a point on ∂V_{b_i}, $i = \{1, 2\}$. The magnitude of the relative tangential velocity $\dot{u}$ then reads:

$$\dot{u}(\mathbf{x}, t) = \left[\dot{\mathbf{u}}_{b_2,b_1}(\mathbf{x}, t)\right]^{\mathrm{T}} \hat{\mathbf{s}}(\mathbf{y}^*(\mathbf{x}, t)). \tag{3.40}$$

Coulomb's law of friction implies:

$$|\bar{\tau}| \leq 1 \quad \text{such that:} \tag{3.41}$$

$$|\bar{\tau}| < 1 \quad \Rightarrow \quad \dot{u} = 0; \tag{3.42}$$

$$|\bar{\tau}| = 1 \quad \Rightarrow \quad \operatorname{sgn}(\dot{u}) = \operatorname{sgn}(\bar{\tau}). \tag{3.43}$$

To make the constraints given in Eqs. (3.36) – (3.38) suitable for incorporation in variational formulations such as the Finite Element Method, a function $w_n(g, \lambda)$ can be defined such that Eqs. (3.36) – (3.38) are satisfied when $w_n(g, \lambda) = 0$. First, one considers the regularized function:

$$\lambda = \epsilon_n / g, \tag{3.44}$$

where $\epsilon_n \ll 1$, which approximately satisfies the conditions given in Eqs. (3.36) – (3.38), as shown in Fig. 3.6. Then, from Eq. (3.44), a viable expression for $w_n(g, \lambda)$ is:

$$w_n(g, \lambda) = (g + \lambda)/2 - \sqrt{(g - \lambda)^2/4 + \epsilon_n}. \tag{3.45}$$

The same procedure can be used to address friction related constraints. Instead of relying on Eqs. (3.41) – (3.43), one uses the regularized function:

$$\bar{\tau} = 2/\pi \ \tan^{-1}\{\dot{u}/\epsilon_s\}, \tag{3.46}$$

where $\epsilon_s \ll 1$, which is also shown in Fig. 3.6. From Eq. (3.46), the following implicit definition can be used to establish $w_s = w_s(\dot{u}, \bar{\tau})$:

$$\bar{\tau} + w_s - 2/\pi \ \tan^{-1}\{(\dot{u} - w_s)/\epsilon_s\} = 0. \tag{3.47}$$

Then, Eqs. (3.41) – (3.43) are approximately satisfied when $w_s = 0$.

In the Finite Element Method, the position vector $\mathbf{x}$ related to the contactor point is translated to the location occupied by the contactor node k_c, as shown in Fig. 3.5. The closest point location $\mathbf{y}^*$ on the target surface can be obtained via the interpolation procedures admitted for the target finite element. In the case depicted in Fig. 3.5, where an isoparametric element with two nodes k_1 and k_2 is considered, $\mathbf{y}^*$ can be computed as:

$$\mathbf{y}^* = \left(1 - \bar{\beta}\right) \left[\ (x_1)_{k_1} \quad (x_2)_{k_1}\ \right]^{\mathrm{T}} + \bar{\beta} \left[\ (x_1)_{k_2} \quad (x_2)_{k_2}\ \right]^{\mathrm{T}}, \tag{3.48}$$

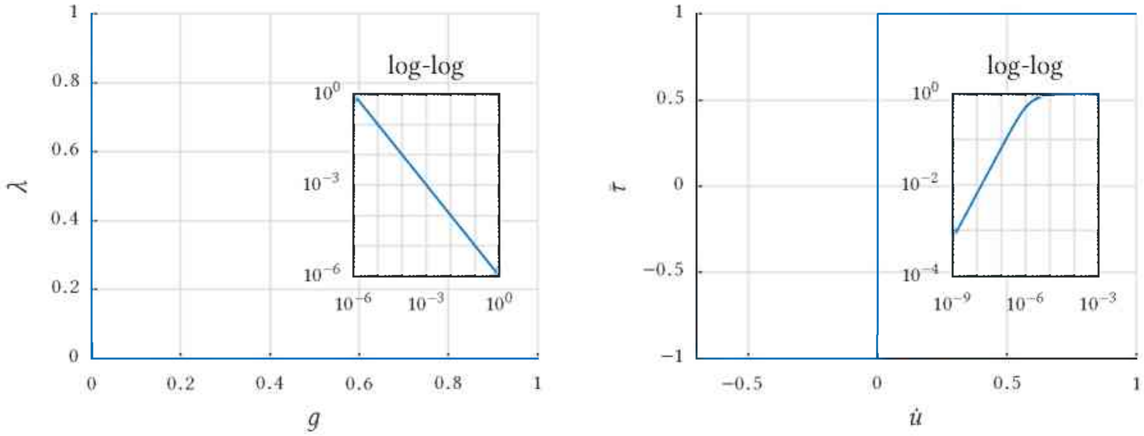

Figure 3.6 – Regularized functions used to enforce contact conditions ($\epsilon_n = \epsilon_s = 10^{-6}$)

with $(x_i)_k = (X_i)_k + (u_i)_k$, where $(X_i)_k$ and $(u_i)_k$, with $i = \{1, 2\}$ and $k = \{k_1, k_2\}$, denote the initial position and displacement in direction i of node k, respectively. $\bar{\beta}$ is a weighting coefficient that can be determined, in this specific case, by means of:

$$\bar{\beta} = \left\{ \left[\begin{array}{cc} (x_1)_{k_c} & (x_2)_{k_c} \end{array} \right] - \left[\begin{array}{cc} (x_1)_{k_1} & (x_2)_{k_1} \end{array} \right] \right\} \hat{\mathrm{s}} \left(\mathrm{y}^* \left(\mathrm{x}, t \right) \right). \tag{3.49}$$

The unit vectors $\hat{\mathrm{n}}$ and $\hat{\mathrm{s}}$ can be computed based on the target element current configuration, through the use of the interpolation functions. In the general case, the problem becomes nonlinear, as expressed in Eq. (3.35). If the target element is as shown in Fig. 3.5, it is possible to obtain:

$$\mathrm{s} = \left[\begin{array}{cc} (x_1)_{k_2} & (x_2)_{k_2} \end{array} \right]^{\mathrm{T}} - \left[\begin{array}{cc} (x_1)_{k_1} & (x_2)_{k_1} \end{array} \right]^{\mathrm{T}} ; \tag{3.50}$$

$$\hat{\mathrm{s}} = \mathrm{s} / ||\mathrm{s}|| ; \tag{3.51}$$

$$\hat{\mathrm{n}} = \pm \left[\begin{array}{cc} 0 & -1 \\ 1 & 0 \end{array} \right] \hat{\mathrm{s}}, \tag{3.52}$$

where, in Eq. (3.52), the ± symbol is used to indicate that the choice of an outward unit normal depends on the orientation assumed by $\hat{\mathrm{s}}$.

After these considerations, the contact loads acting on the contactor node k_c and on the target element nodes k_1 and k_2 can be computed as:

$$(\mathrm{F}_{\text{contact}})_{k_c} = -\lambda \left(\hat{\mathrm{n}} + \bar{\mu} \bar{\tau} \hat{\mathrm{s}} \right) ; \tag{3.53}$$

$$(\mathrm{F}_{\text{contact}})_{k_1} = \left(1 - \bar{\beta} \right) \lambda \left(\hat{\mathrm{n}} + \bar{\mu} \bar{\tau} \hat{\mathrm{s}} \right) ; \tag{3.54}$$

$$(\mathrm{F}_{\text{contact}})_{k_2} = \bar{\beta} \lambda \left(\hat{\mathrm{n}} + \bar{\mu} \bar{\tau} \hat{\mathrm{s}} \right) . \tag{3.55}$$

In the general case, of a target element with more than two nodes, the contact load should be distributed among all the nodes of the target element by considering the interpolation procedure used to compute y^* (ETEROVIC; BATHE, 1991).

Finally, the contact conditions can be incorporated into a finite element formulation through:

a) the application of the contact forces to the relevant finite element mesh degrees of freedom; and

b) the enforcement of the constraints given in Eqs. (3.45) and (3.47).

Herein, an augmented Lagrange multiplier approach is adopted, such that λ and $\bar{\mu}$ are determined during the solution process, and the nonlinear constraints are solved simultaneously with the finite element equations.

3.5 Coupling and Solution Procedures

In this Section, the coupling between the previously presented models is considered. An augmented approach has been favored because of its general nature, despite possible concerns about computational cost. Also, since the problem is nonlinear, based on the loads due to interacting magnets and the SMA constitutive behavior, a Newton-Raphson iterative procedure has been adopted for carrying out solution computations.

3.5.1 SMA Actuators Coupling and Residual Equations

The SMA wire modeling strategy presented previously in Section 3.2 can be coupled with the structural finite element model equations by simultaneously considering:

a) the kinetic evolution equations for ξ, Eq. (3.15);

b) the wire thermal equilibrium rate equation, Eq. (3.17); and

c) its mechanical equilibrium equation, as well, that hasn't yet been established.

For this purpose, one recognizes that the longitudinal strain in an SMA wire can be expressed as:

$$\epsilon = (L - L_0)/L_0, \tag{3.56}$$

where L denotes its length at a given instant of time.

Herein, the SMA wire is coupled to a structure whose behavior is modeled through finite elements. By considering this, L will be given by $L = L(\mathbf{u}_{\text{SMA}})$, where the displacements' vector $\mathbf{u}_{\text{SMA}}$ corresponds to a subset of the finite element nodal degrees of freedom vector, denoted by $\mathbf{u}$.

By assuming that the end points of an SMA wire are attached to two distinct nodes k_1 and k_2 of the finite element mesh, then, in the 2D case:

$$\mathbf{u}_{\text{SMA}} = \begin{bmatrix} (u_1)_{k_1} & (u_2)_{k_1} & (u_1)_{k_2} & (u_2)_{k_2} \end{bmatrix}^{\text{T}}, \tag{3.57}$$

and L can be obtained through:

$$L = \sqrt{\left[(x_1)_{k_2} - (x_1)_{k_1}\right]^2 + \left[(x_2)_{k_2} - (x_2)_{k_1}\right]^2}, \tag{3.58}$$

where it should be recalled that $(x_i)_k = (X_i)_k + (u_i)_k$ for $i = \{1, 2\}$ and $k = \{k_1, k_2\}$.

The mechanical coupling of an SMA wire with the structure is completed by deriving the force the former applies upon the latter, according to:

$$(\mathbf{F}_{\text{SMA}})_{k_1} = \begin{bmatrix} (F_1)_{k_1} & (F_2)_{k_1} \end{bmatrix}^{\text{T}} = (\sigma A_0)\, \hat{\mathbf{r}}_{k_1,k_2}; \tag{3.59}$$

$$(\mathbf{F}_{\text{SMA}})_{k_2} = \begin{bmatrix} (F_1)_{k_2} & (F_2)_{k_2} \end{bmatrix}^{\text{T}} = -(\sigma A_0)\, \hat{\mathbf{r}}_{k_1,k_2}, \tag{3.60}$$

where $(\mathbf{F}_{\text{SMA}})_k$ is the vector of forces applied on node k due to the SMA wire, and σ denotes the stress, given by Eq. (3.13). To comply with the condition of a wire actuator, in the implemented algorithm it is enforced that $\sigma \geq 0$ for all times. $(F_i)_k$ denotes the force applied on node k along direction i, and $\hat{\mathbf{r}}_{k_1,k_2}$ is the unit vector pointing from node k_1 to node k_2, given by:

$$\hat{\mathbf{r}}_{k_1,k_2} = \begin{bmatrix} \cos\theta & \sin\theta \end{bmatrix}^{\text{T}}; \tag{3.61}$$

$$\theta = \text{atan2}\left\{(x_2)_{k_2} - (x_2)_{k_1}, (x_1)_{k_2} - (x_1)_{k_1}\right\}, \tag{3.62}$$

where atan2$\{d, n\}$ is used to evaluate $\tan^{-1}\{n/d\}$ and produce results in the $[-\pi, \pi)$ range.

Figure 3.7 shows a schematic illustration of this coupling procedure. The wire is replaced by a statically equivalent system of forces, that are transferred to the finite element nodes according to the procedure outlined previously: the SMA material constitutive equation is used in deriving the forces that are applied to the model; and the wire strain is computed by taking into account the displacements of its supporting nodes. These explanations clearly lay emphasis on the bidirectional coupling nature of the adopted approach.

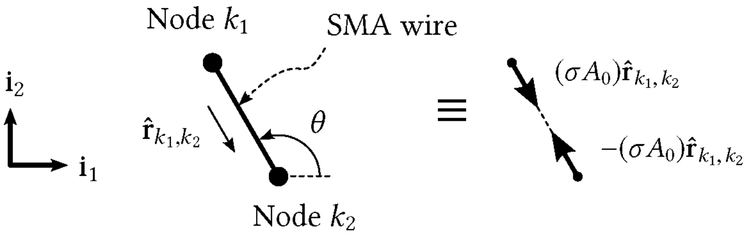

Figure 3.7 – SMA wire attached to FE mesh nodes, the unit vector $\hat{\mathbf{r}}_{k_1,k_2}$, and the equivalent system of forces by which the wire can be replaced

A final observation about the load vectors $(\mathrm{F}_{\mathrm{SMA}})_k$, $k = \{k_1, k_2\}$, reflects their nodal nature. Appropriate degree of freedom compatibility should be taken into account for transferring these to the global finite element equations.

Attention is now devoted to the rate equations previously given for $\dot{\xi}$ and $\dot{T}$. These differential equations can be expressed in the form of nonlinear algebraic equations by considering a set of integration formulas. Here, one considers:

$$\xi|_{n+1} = \xi|_n + \Delta t \left\{ \alpha \, \dot{\xi}\big|_{n+1} + (1-\alpha) \, \dot{\xi}\big|_n \right\}; \tag{3.63}$$

$$T|_{n+1} = T|_n + \Delta t \left\{ \alpha \, \dot{T}\big|_{n+1} + (1-\alpha) \, \dot{T}\big|_n \right\}, \tag{3.64}$$

where Δt is the time discretization increment, and α is a constant that controls the integration rule that is used. More specifically, $\alpha = \left\{0, \frac{1}{2}, 1\right\}$ implies the use of forward Euler, trapezoidal rule, and backward Euler methods, respectively. Also, subscripts $(\,)_n$ and $(\,)_{n+1}$ represent indexes for time discretization, such that $t_n = n\Delta t$, with $n = \{0, \ldots, N_{\max}\}$, $N_{\max}$ being the maximum number of integration time steps. Furthermore, the notation $(\,)|_n$ is used to indicate the evaluation of a given variable at t_n.

From Eqs. (3.63) and (3.64), it is possible to establish the residual equations:

$$\mathrm{R}_{\xi}\big|_{n+1} = \xi|_{n+1} - \xi|_n - \Delta t \left\{ \alpha \, \dot{\xi}\big|_{n+1} + (1-\alpha) \, \dot{\xi}\big|_n \right\} = 0; \tag{3.65}$$

$$R_T|_{n+1} = T|_{n+1} - T|_n - \Delta t \left\{ \alpha \, \dot{T}\big|_{n+1} + (1-\alpha) \, \dot{T}\big|_n \right\} = 0, \tag{3.66}$$

where derivatives are evaluated with the help of Eqs. (3.15) and (3.17). This system of equations is coupled, and must be solved while simultaneously considering the mechanical equilibrium equations for $\mathbf{u}$, since the SMA wire strain is a function of $\mathbf{u}_{\mathrm{SMA}}$.

3.5.2 *Permanent Magnets Coupling*

The loads that are due to interacting magnets are applied to the finite element model by considering that each magnet centroid is coincident with a mesh node. This procedure assumes that each magnet is rigidly attached to the structure, and interface effects are disregarded.

As a magnet centroid is attached to a mesh node, the loads that result from the interaction of two magnets become displacement dependent. They can be evaluated as described previously in Section 3.3.

First, it should be noted that, in Eq. (3.30), $\mathbf{r}_{m_2,m_1}$ can be expressed, in the global finite element coordinate system, as:

$$^{g}\mathbf{r}_{m_2,m_1} = \left[\ (x_1)_{m_2} \quad (x_2)_{m_2}\ \right]^{\mathrm{T}} - \left[\ (x_1)_{m_1} \quad (x_2)_{m_1}\ \right]^{\mathrm{T}}, \tag{3.67}$$

where the subscripts m_1 and m_2 are used to identify the nodes to which the magnets' centroids are attached to.

Additionally, it should be noted that the rotation matrices $^{m_1}\Phi^{g}$ and $^{m_2}\Phi^{g}$ are dependent on the nodal angular displacements ψ_{m_1} and ψ_{m_2}, respectively.

After the determination of these, coordinate transformations can be carried out. Then, Eq. (3.30) can be evaluated for distinct values of $^{m_2}\mathbf{r}$; corresponding values are obtained for $^{m_1}\bar{\mathrm{F}}_{m_2,m_1}$, with which numerical integration is performed for the determination of $^{m_1}\mathrm{F}_{m_2,m_1}$ and $^{m_1}\mathbf{M}_{m_2,m_1}$, from Eqs. (3.27) and (3.28). Further coordinate transformation leads to the availability of $^{g}\mathrm{F}_{m_2,m_1}$ and $^{g}\mathbf{M}_{m_2,m_1}$, which are the force and moment loads in the global finite element coordinate system — produced on magnet m_2 due to magnet m_1.

Then, in the case of the 2D beam finite element considered on Section 3.1, the load vector:

$$\mathrm{F}_{m_2} = \left[\ \left(\mathrm{F}_{m_2,m_1}\right)_1 \quad \left(\mathrm{F}_{m_2,m_1}\right)_2 \quad \left(\mathbf{M}_{m_2,m_1}\right)_3\ \right]^{\mathrm{T}} \tag{3.68}$$

is applied to the node at which the magnet m_2 centroid is attached to, where $(\ )_i$ is used to denote the i-th component of a given vector quantity, for $i = \{1, 2, 3\}$. The computation of F_{m_1}, which is applied to the node where the centroid of the magnet m_1 is located, can be performed in an analogous manner.

3.5.3 *Contact Model Coupling*

The contact modeling strategy directly exposes the coupling procedures that need to be adopted for its implementation.

From what has been shown in Section 3.4, it can be seen that most of the computations rely on the availability of the displacements of the contactor node k_c, and of the nodes k_1 and k_2 of the target element. Also, the contact unknowns λ and $\bar{\tau}$ directly affect the value of the contact force, and the constraint equations that need to be solved together with the finite element residual equations.

The contact loads are applied to the finite element model together with the other acting loads. Residues that need to be evaluated are:

$$R_\lambda = w_n = 0; \tag{3.69}$$

$$R_{\bar{\tau}} = w_s = 0, \tag{3.70}$$

with w_n defined in Eq. (3.45), and w_s implicitly defined in Eq. (3.47).

3.5.4 *Solution Algorithm*

The Newton-Raphson method has been adopted for the solution of the nonlinear algebraic equations that result from considering the coupling procedures addressed before.

The unknowns of the problem are the finite element nodal degrees of freedom, $\mathbf{u}$; the ensemble of normal, and normalized tangential loads, for all of the contact pairs, $\boldsymbol{\lambda}$ and $\bar{\boldsymbol{\tau}}$, respectively; and the ensemble of martensite volumetric fractions, and temperatures, for all of the SMA actuators, $\boldsymbol{\xi}$ and T, respectively. More precisely, the vectors $\boldsymbol{\lambda}$, $\bar{\boldsymbol{\tau}}$, $\boldsymbol{\xi}$, and T are such that:

$$\boldsymbol{\lambda} = \begin{bmatrix} \lambda_{c_1} & \lambda_{c_2} & \cdots & \lambda_{c_{N_c}} \end{bmatrix}^{\mathrm{T}}; \tag{3.71}$$

$$\bar{\boldsymbol{\tau}} = \begin{bmatrix} \bar{\tau}_{c_1} & \bar{\tau}_{c_2} & \cdots & \bar{\tau}_{c_{N_c}} \end{bmatrix}^{\mathrm{T}}; \tag{3.72}$$

$$\boldsymbol{\xi} = \begin{bmatrix} \xi_{a_1}^{\mathrm{T}} & \xi_{a_2}^{\mathrm{T}} & \cdots & \xi_{a_{N_a}}^{\mathrm{T}} \end{bmatrix}^{\mathrm{T}}; \tag{3.73}$$

$$\mathrm{T} = \begin{bmatrix} T_{a_1} & T_{a_2} & \cdots & T_{a_{N_a}} \end{bmatrix}^{\mathrm{T}}, \tag{3.74}$$

where λ_c and $\bar{\tau}_c$ are associated with the contact pair c, ξ_a and T_a are related to the SMA wire actuator a, and N_c and N_a designate the total number of contact pairs, and SMA wire actuators, respectively, that are part of the system.

The equations to be solved can be expressed as the residual:

$$\mathrm{R}_{\text{system}} = \begin{bmatrix} \mathrm{R}_{\mathbf{u}}^{\mathrm{T}} & \mathrm{R}_{\boldsymbol{\lambda}}^{\mathrm{T}} & \mathrm{R}_{\bar{\boldsymbol{\tau}}}^{\mathrm{T}} & \mathrm{R}_{\boldsymbol{\xi}}^{\mathrm{T}} & \mathrm{R}_{\mathrm{T}}^{\mathrm{T}} \end{bmatrix}^{\mathrm{T}} = 0, \tag{3.75}$$

with:

$$\begin{aligned} \mathrm{R}_{\mathbf{u}} = \mathrm{F}_{\text{int}} - \mathrm{F}_{\text{ext}} - \sum\nolimits_{i=1}^{N_a} \left\{ \left[(\mathrm{F}_{\text{SMA}})_{k_1} \right]_{a_i} + \left[(\mathrm{F}_{\text{SMA}})_{k_2} \right]_{a_i} \right\} - \sum\nolimits_{i=1}^{N_p} \left\{ \left(\mathrm{F}_{m_1} \right)_{p_i} + \left(\mathrm{F}_{m_2} \right)_{p_i} \right\} \\ + \sum\nolimits_{i=1}^{N_c} \left\{ \left[(\mathrm{F}_{\text{contact}})_{k_c} \right]_{c_i} + \left[(\mathrm{F}_{\text{contact}})_{k_1} \right]_{c_i} + \left[(\mathrm{F}_{\text{contact}})_{k_2} \right]_{c_i} \right\}; \end{aligned} \tag{3.76}$$

$$\mathrm{R}_{\boldsymbol{\lambda}} = \begin{bmatrix} (R_\lambda)_{c_1} & (R_\lambda)_{c_2} & \cdots & (R_\lambda)_{c_{N_c}} \end{bmatrix}^{\mathrm{T}}; \tag{3.77}$$

$$\mathrm{R}_{\bar{\boldsymbol{\tau}}} = \begin{bmatrix} (R_{\bar{\tau}})_{c_1} & (R_{\bar{\tau}})_{c_2} & \cdots & (R_{\bar{\tau}})_{c_{N_c}} \end{bmatrix}^{\mathrm{T}}; \tag{3.78}$$

$$\mathrm{R}_{\boldsymbol{\xi}} = \begin{bmatrix} (\mathrm{R}_{\xi})_{a_1}^{\mathrm{T}} & (\mathrm{R}_{\xi})_{a_2}^{\mathrm{T}} & \cdots & (\mathrm{R}_{\xi})_{a_{N_a}}^{\mathrm{T}} \end{bmatrix}^{\mathrm{T}}; \tag{3.79}$$

$$\mathrm{R}_{\mathrm{T}} = \begin{bmatrix} (R_T)_{a_1} & (R_T)_{a_2} & \cdots & (R_T)_{a_{N_a}} \end{bmatrix}^{\mathrm{T}}, \tag{3.80}$$

where $\mathrm{R}_{\mathbf{u}}$ is the residual vector related to the global finite element equations, $\mathrm{R}_{\boldsymbol{\lambda}}$ and $\mathrm{R}_{\bar{\boldsymbol{\tau}}}$ are the residual vectors related to the constraints imposed by the contact pairs, and $\mathrm{R}_{\boldsymbol{\xi}}$ and R_{T} are the residual vectors associated with the rate equations for the martensite fractions and temperatures of the SMA wire actuators. In Eq. (3.76), $[(\mathrm{F}_{\text{SMA}})_k]_a$ denotes the loads the SMA wire actuator a applies on its anchoring node k, $(\mathrm{F}_m)_p$ represents the loads acting on magnet m of the p-th pair of magnets, and $[(\mathrm{F}_{\text{contact}})_k]_c$ designates the contact loads applied to node k of the contact pair c. In Eqs. (3.77) – (3.80), the subscripts c_i, $i = \{1, \ldots, N_c\}$, and a_i, $i = \{1, \ldots, N_a\}$, are used to distinguish between the several contact pairs and SMA wire actuators that are considered in the system. Expressions that are used for computing the residues have been presented along this Chapter.

Figure 3.8 presents a simplified block diagram of the code that has been implemented in MATLAB® for computing the system residual vector. It shows the order at which computations are performed within one iteration of the solver, and provide a better understanding of what has been discussed in Subsections 3.5.1 – 3.5.3.

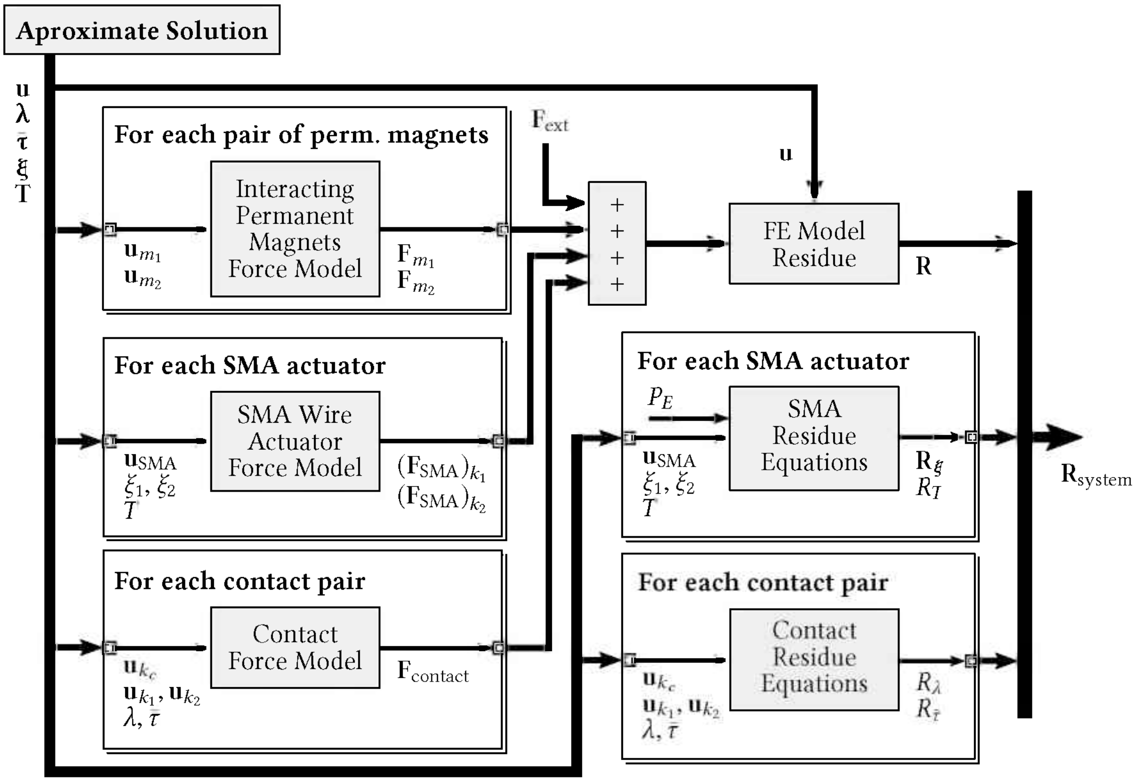

Figure 3.8 – Simplified block diagram for the implemented model

Considering what has been shown in Subsection 3.5.1, one sees that, given values for $\mathbf{u}_{\text{SMA}}$, ξ, and T, the forces related to an actuator, $(\mathbf{F}_{\text{SMA}})_k$, $k = \{k_1, k_2\}$, can be computed, and added to the other loads that are applied to the finite element model. Furthermore, the SMA residue equations can also be evaluated, if the power input term P_E is provided. This procedure is performed for each of the SMA actuators in the system.

With regards to interacting pairs of magnets, still referring to Fig. 3.8, it can be seen that $\mathbf{F}_{m_1}$ and $\mathbf{F}_{m_2}$ are computed depending on the availability of $\mathbf{u}_{m_1}$ and $\mathbf{u}_{m_2}$, as discussed in Subsection 3.5.2. Note that the components of $\mathbf{u}_{m_i}$, $i = \{1, 2\}$, are $(u_1)_{m_i}$, $(u_2)_{m_i}$, and also ψ_{m_i}. Having evaluated the nodal load vectors $\mathbf{F}_{m_1}$ and $\mathbf{F}_{m_2}$, these are transferred from the nodal to the global finite element level framework. The procedure is performed for each pair of interacting magnets. The vector of accumulated loads is then applied to the structural finite element model, together with the other relevant loads.

Figure 3.8 also explicitly shows coupling dependencies for the node-to-element contact model, as pointed out in Subsection 3.5.3.

Since rate equations are associated with $\boldsymbol{\xi}$ and T, solution needs to be calculated based on successful incrementation of time steps, as indicated by what has been shown in Eqs. (3.65) and (3.66). Thus, the Newton-Raphson method is considered for each instant of time for which solution is to be computed.

It is supposed that the solution is known up until some time t_n, and that solution is to be computed for time $t_{n+1} = t_n + \Delta t$. It is also assumed that an approximate solution set, $\mathbf{u}_{\text{system}}\big|_{n+1}^{k}$, is available, where:

$$\mathbf{u}_{\text{system}} = \begin{bmatrix} \mathbf{u}^{\mathrm{T}} & \boldsymbol{\lambda}^{\mathrm{T}} & \bar{\boldsymbol{\tau}}^{\mathrm{T}} & \boldsymbol{\xi}^{\mathrm{T}} & \mathrm{T}^{\mathrm{T}} \end{bmatrix}^{\mathrm{T}}. \tag{3.81}$$

The superscript $(\,)\big|^{k}$ is used to index the approximation, whereas the subscript $(\,)\big|_{n}$ indexes time.

The system residual for t_{n+1} related to a more accurate solution approximation $k + 1$ can then be evaluated by considering its expansion in a Taylor series around the approximate solution k, such that:

$$\mathrm{R}_{\text{system}}\big|_{n+1}^{k+1} = \mathrm{R}_{\text{system}}\big|_{n+1}^{k} + \mathbf{K}_{\text{system}}\big|_{n+1}^{k} \Delta\mathbf{u}_{\text{system}} + \mathcal{O}\left(\Delta\mathbf{u}_{\text{system}}^{2}\right), \tag{3.82}$$

where:

$$\mathbf{K}_{\text{system}} = \frac{\partial \mathrm{R}_{\text{system}}}{\partial \mathbf{u}_{\text{system}}} \quad : \quad \left(\mathbf{K}_{\text{system}}\right)_{i,j} = \frac{\partial \left(\mathrm{R}_{\text{system}}\right)_{i}}{\partial \left(\mathbf{u}_{\text{system}}\right)_{j}} \tag{3.83}$$

denotes the system Jacobian matrix, and:

$$\Delta\mathbf{u}_{\text{system}} \equiv \mathbf{u}_{\text{system}}\big|_{n+1}^{k+1} - \mathbf{u}_{\text{system}}\big|_{n+1}^{k}. \tag{3.84}$$

Furthermore, $\mathcal{O}\left(\Delta\mathbf{u}_{\text{system}}^{2}\right)$ is used to denote contributions to the expansion that depend on powers of $\Delta\mathbf{u}_{\text{system}}$ that are greater than, or equal to 2.

By neglecting these contributions, since it is assumed that the approximate solution set is relatively close the true solution of the problem, and enforcing the requirement that $\mathrm{R}_{\text{system}}\big|_{n+1}^{k+1}$ should be null, it is possible to derive:

$$\Delta\mathbf{u}_{\text{system}} = -\left(\mathbf{K}_{\text{system}}\big|_{n+1}^{k}\right)^{-1} \mathrm{R}_{\text{system}}\big|_{n+1}^{k}, \tag{3.85}$$

from which:

$$\mathbf{u}_{\text{system}}\Big|_{n+1}^{k+1} = \mathbf{u}_{\text{system}}\Big|_{n+1}^{k} + \Delta\mathbf{u}_{\text{system}} \tag{3.86}$$

can be computed.

The procedure is repeated for successive values of k, until some convergence criteria, such as:

$$\left\| \mathbf{R}_{\text{system}}\Big|_{n+1}^{k+1} \right\| \leq \epsilon_{\text{abs}} \tag{3.87}$$

is met, where ϵ_{abs} denotes an absolute error tolerance.

The adoption of the Newton-Raphson method for solution computation can be hampered by some aspects. For instance, the evaluation of the Jacobian matrix can make the method cumbersome in many applications. However, convergence rate can be drastically improved if the problem is well-behaved. For this reason, analytical expressions have been derived for its calculation. This helps in avoiding common issues that are raised due to approximations based on the use of finite difference techniques.

Nevertheless, the physics considered herein pose a significant challenge for the successful application of the Newton-Raphson method. For instance, loads between interacting magnets get increasingly larger when opposing magnetic poles are pushed together, until contact happens. Contact separation results yet in another complication — since solution discontinuity can occur, initial approximations that are based on previous computed solutions can lead to poor convergence, or give rise to solution divergence. Another problem resides in the choice of a fixed time step integration algorithm.

To overcome these difficulties, a line search method has been incorporated into the solution algorithm. In this approach, the solution update procedure shown in Eq. (3.86) is replaced by:

$$\mathbf{u}_{\text{system}}\Big|_{n+1}^{k+1} = \mathbf{u}_{\text{system}}\Big|_{n+1}^{k} + \eta\Delta\mathbf{u}_{\text{system}}, \tag{3.88}$$

where η is determined by minimizing the system overall energy. This directly translates to solving:

$$a\left(\eta\right) = \Delta\mathbf{u}_{\text{system}}^{\mathrm{T}}\ \mathbf{R}_{\text{system}}\Big|_{n+1}^{k+1} = 0, \tag{3.89}$$

where the system residual is evaluated by considering the condition given in Eq. (3.88). Solution of Eq. (3.89) is performed by considering the regula falsi method, such that the overall procedure is similar to the one reported in the ANSYS® finite element software documentation (ANSYS, 2015).

Also, to alleviate further convergence issues during solution computation, numerical smoothing has been performed for several discontinuities included in the model. These involve, for instance, the rate equations for ξ, that are based on an if/else construction, as seen in Eq. (3.15). Another example is related to the vector $\mathbf{m}$, whose computation is also based on if/else statements, as shown in Eqs. (3.16a) – (3.16c). A final example concerns the modeling used for the SMA wire actuators, that calls for the condition $\sigma \geq 0$ — which can also be described as an if/else statement.

Discontinuities like these can be tackled by considering a smoothed Heaviside function $\tilde{H}$. It can be computed from the sigmoid:

$$\mathscr{s}(x) = \operatorname{erf}\left\{\sqrt{\pi}Kx/2\right\}, \tag{3.90}$$

where erf{ } denotes the error function, and K denotes a big number (herein, it has been adopted that $K = 10^4$). Then:

$$\tilde{H}(x) = \left[\mathscr{s}(x) + 1\right]/2. \tag{3.91}$$

A fictitious function whose construction is based on an if/else statement is considered as an example. Suppose that:

$$f\left(x\right) = \begin{cases} f_1\left(x\right) & \text{if } x \geq x_1; \\ f_2\left(x\right) & \text{otherwise,} \end{cases} \tag{3.92}$$

where f_1 and f_2 are each one continuous functions of x. Then:

$$f \approx \tilde{f}(x) = f_1(x)\ \tilde{H}(x - x_1) + f_2(x)\ \left[1 - \tilde{H}(x - x_1)\right] \tag{3.93}$$

represents a smooth, continuous approximation for f. In fact, $\tilde{f} \longrightarrow f$ as $K \longrightarrow +\infty$ in Eq. (3.90). In the case an if/elseif/.../else statement is adopted in the definition of a discontinuous function, then it its attractive to recast its definition by considering multiple nested if/else statements before applying the smoothing procedure just described.

Figure 3.9 shows a flowchart related to the solution algorithm just described. As can be seen, line-search is performed only if the Newton-Raphson algorithm has not converged within k_{LS} iterations. Furthermore, if the solution strategy exceeds $k_{\max}$ iterations, then it is considered to have diverged. In this case, the same procedure is applied once more, but with a different initial guess — namely, by considering $\mathbf{u}_{\text{system}}\big|_{n+1}^{0} = \mathbf{u}_{\text{system}}\big|_{0}$. If divergence still persists, the time step Δt gets reduced according to $(\Delta t)_{\text{new}} = (\Delta t)_{\text{old}} / k_{\Delta t}$. Then, after $k_{\Delta t}$ successful solution computations, the time step is changed back to its original value $(\Delta t)_{\text{old}}$. If divergence is detected when using a reduced time step, then the algorithm is stopped. Numerical results provided later have all been computed by considering $k_{\text{LS}} = 10$, $k_{\max} = 500$, and $k_{\Delta t} = 100$. It should be noted that a high value has been adopted for $k_{\max}$ since the line-search procedure that has been used can show slow convergence rates.

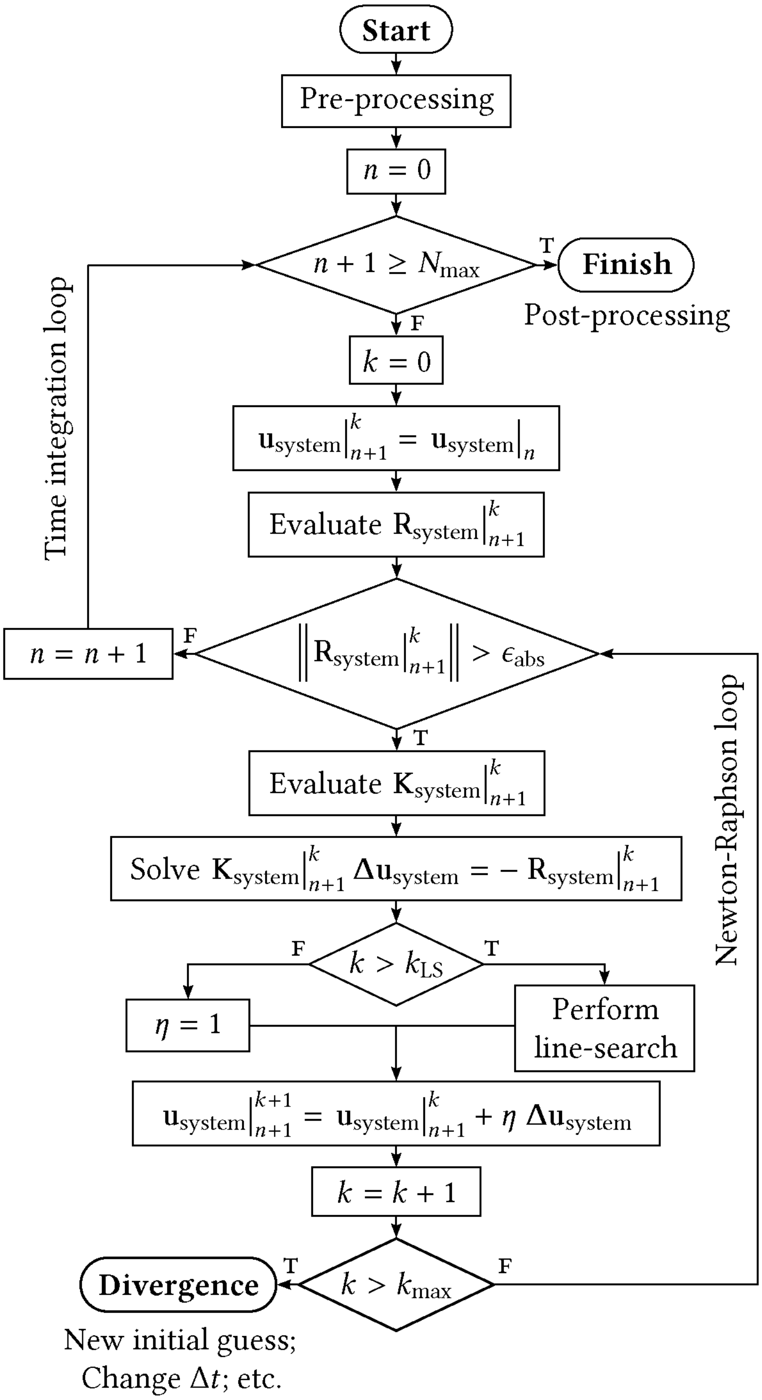

Figure 3.9 – Iterative solution algorithm flowchart

3.6 Summary

Along this Chapter, several modeling strategies have been considered. These embrace a geometrically nonlinear beam finite element; a thermomechanical constitutive relation for SMAs; the interaction of parallelepiped permanent magnets and resulting loads; and a strategy for enforcing node-to-element contact within finite element models. One also considered coupling aspects related to the framework proposed for magneto-thermo-mechanical simulations of systems that combine SMAs and permanent magnets. Finally, a solution strategy for the resulting nonlinear system of equations was discussed, by considering a iterative procedure based on the Newton-Raphson algorithm.

The adopted modeling approach is fairly general, since it relies on augmented Lagrangian-like coupling strategies. Because of this, substitution of one or more modeling schemes can be made while aiming for accuracy and/or speed improvements.

CHAPTER IV

SIMULTANEOUS USE OF SHAPE MEMORY ALLOY ACTUATORS AND PERMANENT MAGNETS IN A SLENDER BEAM

The simultaneous use of SMA wire actuators and permanent magnets is first investigated in this Chapter. A tristable smart structure is considered, which consists of a cantilever beam, to which antagonistic SMA wires and permanent magnets are attached to. As objectives, one considers the validation of the proposed concept, of combining SMA actuators and permanent magnets for multistability; and the verification of the modeling procedures addressed previously in Chapter III.

A description of the system that has been experimentally tested and the setups adopted for data acquisition are described in Section 4.1. Next, in Section 4.2, conditions considered for running numerical simulations are discussed. Results are provided, compared and discussed in Section 4.3. A summary is also given in Section 4.4.

4.1 System Description and Experimental Setup

The system considered in this Chapter is shown in Fig. 4.1. It consists of a relatively thin aluminum clamped-free beam, with two antagonistic SMA wire actuators (Muscle Wires® Flexinol 300 LT) attached to it through a bolt and jam nuts. N52 grade NdFeB permanent magnets were added near the end of the beam, and secured with the use of Loctite® Super Glue. Identical magnets have been kept stationary, positioned at convenient locations, to enable the

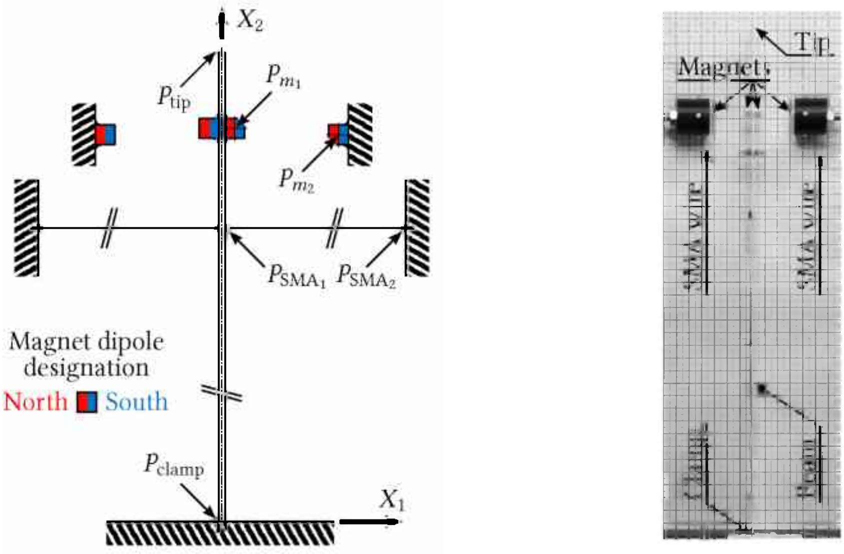

(a) Schematic drawing (b) System photograph

Figure 4.1 – System considered for testing

observation of the desired behavior for the system. The placement of the stationary magnets was performed with the help of auxiliary 3D printed parts, made out of ABS plastic.

Table 4.1 provides the values of the coordinates of the points identified in Fig. 4.1. The beam width and thickness are oriented along X_3 and X_1, and measure 28.5 mm and 1.2 mm, respectively. The diameter of the SMA wires is equal to 300 μm, and the permanent magnets have sides measuring 6.35 mm, or $\frac{1}{4}$ of an inch. The arrangement of all components is also such that there is symmetry with respect to the (X_1, X_2) plane. There is also symmetry with respect to the (X_2, X_3) plane, as indicated by the beam center line in the schematic drawing in Fig. 4.1(a), when the beam occupies a vertical position.

Table 4.1 – Coordinates of the points identified in Fig. 4.1(a)

Point	X_1 [mm]	X_2 [mm]
P_{clamp}	0.0	0.0
P_{tip}	0.0	400.0
P_{m_1}	3.775	330.0
P_{m_2}	34.0	328.0
P_{SMA_1}	4.775	300.0
P_{SMA_2}	1314.775	300.0

SMA wires have been installed as received from the manufacturer. According to it, the wires are trained while subjected to a 200 MPa load. In the experimental arrangement, actuators were routed through small pulleys covered with Kapton® tape, to provide thermal insulation at these points, as can be seen in Fig. 4.2. Considering the total length of the wires, and that only three pulleys were used to allow for a greater actuator length, the effect of these pulleys on performance is deemed negligible. The fixed end of each wire was anchored with jam nuts. Also, before securing them, a static pre-load of $\sigma_0 = 100$ MPa have been applied with the use of dead weights.

The conditions adopted for experimental characterization are now considered. Each of the SMA wire actuators have been subjected to their corresponding voltage loading patterns, which are shown in Fig. 4.3. As can be seen, a ramp loading/unloading condition is considered for each wire, with only one of them being actuated at a time.

It is clear from this figure that quasi-static loading conditions have been considered. The choice for such an approach is related to the fact that the behavior of SMA materials is rate-dependent (LAGOUDAS, 2008; CISSE; ZAKI; ZINEB, 2016b). The adopted SMA model can account for some variation in the speed with which thermomechanical transformation happens through the constant v_0, see Eq. (3.15), p. 34; and also through the constant c_I, see Eq. (3.12),

Figure 4.2 – Photograph of the system prior to the installation of magnets

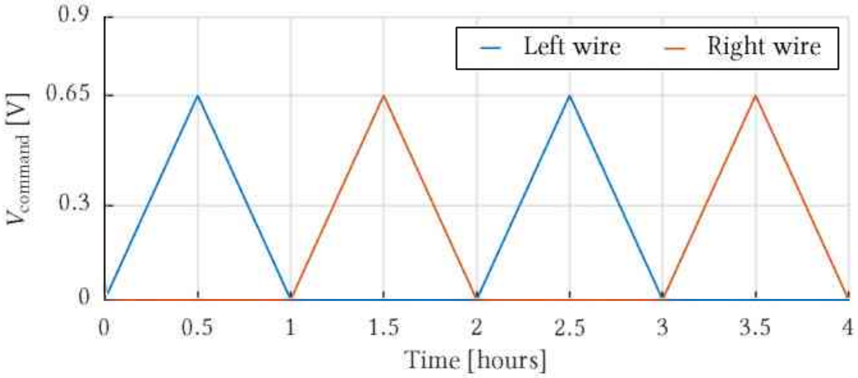

Figure 4.3 – Voltages adopted for driving the SMA wire actuators

that provides control for the transformation hardening behavior. Despite these capabilities presented by the model, a conservative approach has been selected while dealing with the tests for the system considered in this Chapter, since these were the first ones performed within the Thesis context. The scope of the tests is thus narrowed, such that additional hurdles owed to faster loading rate patterns could be avoided — the multi-physics nature of the studied system already proves itself rather complex.

Two configurations have been investigated, consisting of the system with and without permanent magnets. The consideration of both of these conditions allows for a direct comparison of results, thus making it possible to evaluate the influences that are due to the permanent magnets on the overall system behavior.

Regarding room temperature, it has been controlled by an air conditioning unit to be 20 °C during the whole length of the tests.

Attention is now devoted to the measurement and excitation systems used for testing. Acquisitions and recordings have been made possible with the help of a National Instruments® USB-6259 BNC DAQ device, and a personal laptop.

Temperatures, voltages and currents have been monitored on both SMA wires. Temperature measurements were performed with Omega® K type, 40 AWG wire (80 μm in diameter), thermocouples, which were paired with Analog Devices® AD8495 precision amplifiers, capable of performing cold junction compensation. The output of these amplifiers have been directly fed to analog input channels of the NI® USB-6259 BNC DAQ. Voltage drops along each of the actuators have been measured with the help of simple voltage dividers, which were used to prevent saturation on the input ports of the NI® DAQ board. Currents applied to the wires have also been recorded, now with the use of Texas Instruments® INA250 integrated circuits, whose outputs were also directly connected to the DAQ device.

The displacement field of the beam has also been captured. For this purpose, a Canon® EOS 1000D digital camera has been used, while coupled to an EF75–300mm f/4-5.6 lens. To mitigate visual distortion effects, the camera has been positioned as far away as possible from the system under test, at approximately 4 m. Photos were taken every 5 seconds, which has been deemed a sufficient rate for the adopted quasi-static SMA actuation pattern. The acquired images were then post-processed, and the displacement of specific locations have been determined with the use of the open-source Tracker software (BROWN, 2017). It consists of a video analysis and modeling tool that allows for, among other capabilities, manual and automated object tracking, with position, velocity and acceleration outputs.

The NI® USB-6259 BNC DAQ also provided the command voltage used to drive the SMA actuators. The analog output has been directed to a Labworks Inc. PA-138 Linear Power Amplifier. This equipment has been set up as a voltage source, with an amplification gain of approximately 29 V/V. A digital relay has been connected in series with the power amplifier output to direct the electrical current either through the left or the right actuator, as needed.

4.2 Numerical Simulations Setup

Conditions used for performing numerical simulations are now discussed. The implemented code is based on what has been presented previously in Chapter III.

The adopted finite element mesh is shown in Fig. 4.4. The beam has been discretized by considering 40 elements with three nodes each, such that parabolic interpolation is used for the description of the displacement fields along their length.

To connect the SMA wire actuators and permanent magnets coupling nodes to the beam mesh, and simultaneously account for small offsets observed in the experimental setup, some finite elements with two nodes each have been incorporated into the model. These can be observed in the zoomed plots provided in Fig. 4.4.

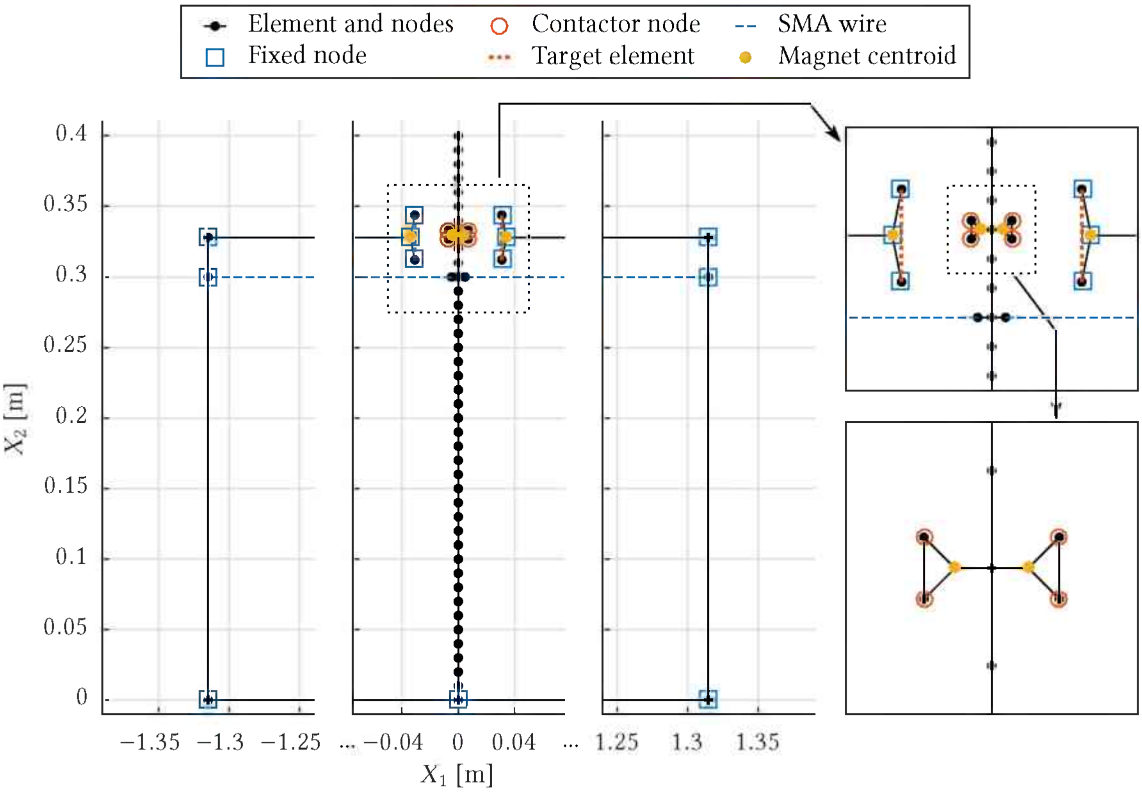

Figure 4.4 – Finite element mesh used for numerical simulations; internal finite element nodes are not shown

Finite elements with two nodes have also been considered for modeling the surfaces of the magnets that are subjected to contact, and accordingly treated as target elements.

All of these finite elements with two nodes were considered to possess higher values for EA, GA_s, and EI, in order to simulate rigid connections and surfaces, depending where they were used. Table 4.2 provides the numerical values adopted for model parameters.

The power input term P_E for each of the SMA wire actuators were specified after analyzing experimental data. Cubic polynomials were fitted to the observed electric power during the heating and cooling phases of the actuators. For the left wire:

$$\begin{aligned}(P_E)_{\text{left}} = \textstyle\sum_{k=1}^{\infty} \{ & f_{\text{left}}\{t - 30\,(4k-4)\}\,[H\{t-30\,(4k-4)\} - H\{t-30\,(4k-3)\}] \\ & + f_{\text{left}}\{30\,(4k-2)-t\}\,[H\{t-30\,(4k-3)\} - H\{t-30\,(4k-2)\}]\}\,, \end{aligned} \tag{4.1}$$

Table 4.2 – Model parameters used for conducting simulations

Scope	Parameter	Value	Units
Beam material			
	E	65	GPa
	G	24.38	GPa
SMA wire actuators			
	T_∞	20	°C
	h	0.240	$\mathrm{kW(m^2{\cdot}K)^{-1}}$
	d_0	0.300	mm
	β	0.0289	–
	E_A	75	GPa
	E_M	28	GPa
	T_R	15.44	°C
	Δs	−80.615	$\mathrm{J(kg{\cdot}K)^{-1}}$
	c_I	−0.7297	$\mathrm{kJ{\cdot}kg^{-1}}$
	c_0	0.500	$\mathrm{kJ(kg{\cdot}K)^{-1}}$
	ρ	6.450	$\mathrm{g{\cdot}cm^{-3}}$
	μ_c	0.6634	$\mathrm{kJ{\cdot}kg^{-1}}$
	ν_0	0.238	$\mathrm{g(J{\cdot}s)^{-1}}$

Scope	Parameter	Value	Units
Permanent magnets			
	B_{m_i}	1.43	T
	$(l_i)_{m_i}$	3.175	mm
Contact algorithm			
	$\bar{\mu}$	0.1	–
	ϵ_n	10^{-6}	–
	ϵ_s	10^{-6}	–
Solution algorithm			
	α	0.5	–
	Δt	1	s
	k_{LS}	10	–
	$k_{\max}$	500	–
	$k_{\Delta t}$	100	–
	ϵ_{abs}	10^{-6}	–

where k stands for a dummy counter index, t must be specified in minutes, $H\{\ \}$ denotes the Heaviside unit step function, and:

$$f_{\mathrm{left}}\{t\} = -0.04882t + 0.028845t^2 - 0.000071149t^3 \tag{4.2}$$

represents the fitted polynomial. As for the right actuator:

$$\begin{aligned}(P_E)_{\mathrm{right}} = \sum\nolimits_{k=1}^{\infty} \big\{ & f_{\mathrm{right}}\{t - 30\,(4k-2)\}\,[H\{t - 30\,(4k-2)\} - H\{t - 30\,(4k-1)\}] \\ & + f_{\mathrm{right}}\{30\,(4k) - t\}\,[H\{t - 30\,(4k-1)\} - H\{t - 30\,(4k)\}]\big\}\,,\end{aligned} \tag{4.3}$$

with t once again in minutes, and:

$$f_{\mathrm{right}}\{t\} = -0.03766t + 0.026060t^2 + 0.000011364t^3. \tag{4.4}$$

The value of the ambient temperature T_∞ has been considered equal to the one set on the air conditioning unit located at the room where tests were conducted. As to the convection film coefficient h, its value has been obtained by considering the slope of the plot of T versus P_E. If Eq. (3.17), p. 36, is considered, and transient effects are neglected, a linear fit can be performed on the experimental data such that h assumes the value provided in Tab. 4.2.

Characterization of the SMA wire actuators have not been performed prior to the tests reported in this Chapter. Because of this, the values provided in Tab. 4.2 for the actuators are a mix of: literature data, in the case of d_0, E_A, E_M, c_0, and ρ, as these were thought to be representative of the actual behavior of the SMA material; and fitted parameters, when β, T_R, Δs, c_I, μ_c, and ν_0 are considered.

For fitting these, an optimization problem has been considered. The chosen objective function evaluated to:

$$F = \sqrt{\frac{1}{N_{\max}} \sum_{n=1}^{N_{\max}} \left\{ \left[u_1 \left(X_1^*, X_2^*, t_n \right) \right]_{\text{model}} - \left[u_1 \left(X_1^*, X_2^*, t_n \right) \right]_{\text{exp}} \right\}^2}, \tag{4.5}$$

which represents the root-mean-square deviation associated with beam displacement u_1 evaluated at the SMA actuators attachment location, such that $X_1^* = 0$ mm, and $X_2^* = 300$ mm, cf. Tab. 4.1. As can be seen, the deviation is taken as the difference between the model calculated, and experimentally measured values, which are distinguished by the subscripts $[\;]_{\text{model}}$ and $[\;]_{\text{exp}}$, respectively.

The optimization problem has been solved by considering the differential evolution algorithm, with a population size of 18 individuals. The near-random initial population has been selected by making use of the latin hypercube sampling technique. The design space selected for optimum search has been defined by taking into account literature available data, e.g. (DYNALLOY, 2017). The `rand/1/bin` update scheme was adopted, with amplification factor and crossover probability both set equal to 0.8. The maximum number of iterations was set to 100, but after 30 the algorithm stalled, and stopped prematurely. The optimization solution algorithm that has been used is available as part of the SIMPLE Optimization ToolBox, which has been developed at the Federal University of Uberlândia. It is a MATLAB® add-on that allows for the creation and solution of optimization problems (VIANA, 2008).

The remaining values given in Tab. 4.2, which concern the beam material, the permanent magnets, and the contact algorithm, have been determined based on typical values reported for aluminum physical properties; on manufacturer data for permanent magnets (K&JMAGNETICS, 2017); and on numerical experimentation to achieve accurate contact modeling, respectively.

Regarding initial conditions for $\boldsymbol{\xi}$ and T, denoted by $\boldsymbol{\xi}_0 = [\ (\xi_1)_0 \quad (\xi_2)_0\ ]^{\mathrm{T}}$ and T_0, these were set equal to $[\ 1 \quad 0\ ]^{\mathrm{T}}$ and T_∞, respectively, for both SMA wire actuators.

With respect to the initial lengths of the SMA wire actuators, they have been determined by considering the pre-load $\sigma_0 = 100$ MPa that was applied during their installation prior to testing. It can be shown that:

$$L_0 = L_{\mathrm{SMA}} \left\{ \sigma_0 / E\left(\boldsymbol{\xi}_0\right) + \left[(\xi_1)_0 - (\xi_2)_0 \right] \beta + 1 \right\}^{-1}, \tag{4.6}$$

where $L_{\mathrm{SMA}} = 1.310$ m is the Euclidean distance between P_{SMA_1} and P_{SMA_2}, cf. Fig. 4.1(a) and Tab. 4.1.

4.3 Results and Discussion

Results are now provided. Figure 4.5 initially shows a comparison between experimental data collected for the system with and without permanent magnets, by considering the time history of three distinct points along the beam length. The time labels provided in Fig. 4.5(c) serve as references for the pictures of the system given in Fig. 4.6, from which the complete displacement field of the beam can be seen, thus allowing for an easier comparison and understanding of the results.

An important point must be considered for the analysis of the time history plots provided in Fig. 4.5. Because the voltage provided to the SMA actuators consists of a repetitive pattern with a period of 2 hours, as can be seen in Fig. 4.3, displacements for the second and subsequent actuation cycles are plotted by considering a different time reference, such that results overlap. For example, displacements corresponding to time instants between 2 and 4 hours are plotted as if they have occurred during the 0 to 2 hours time frame, as both of these periods of time

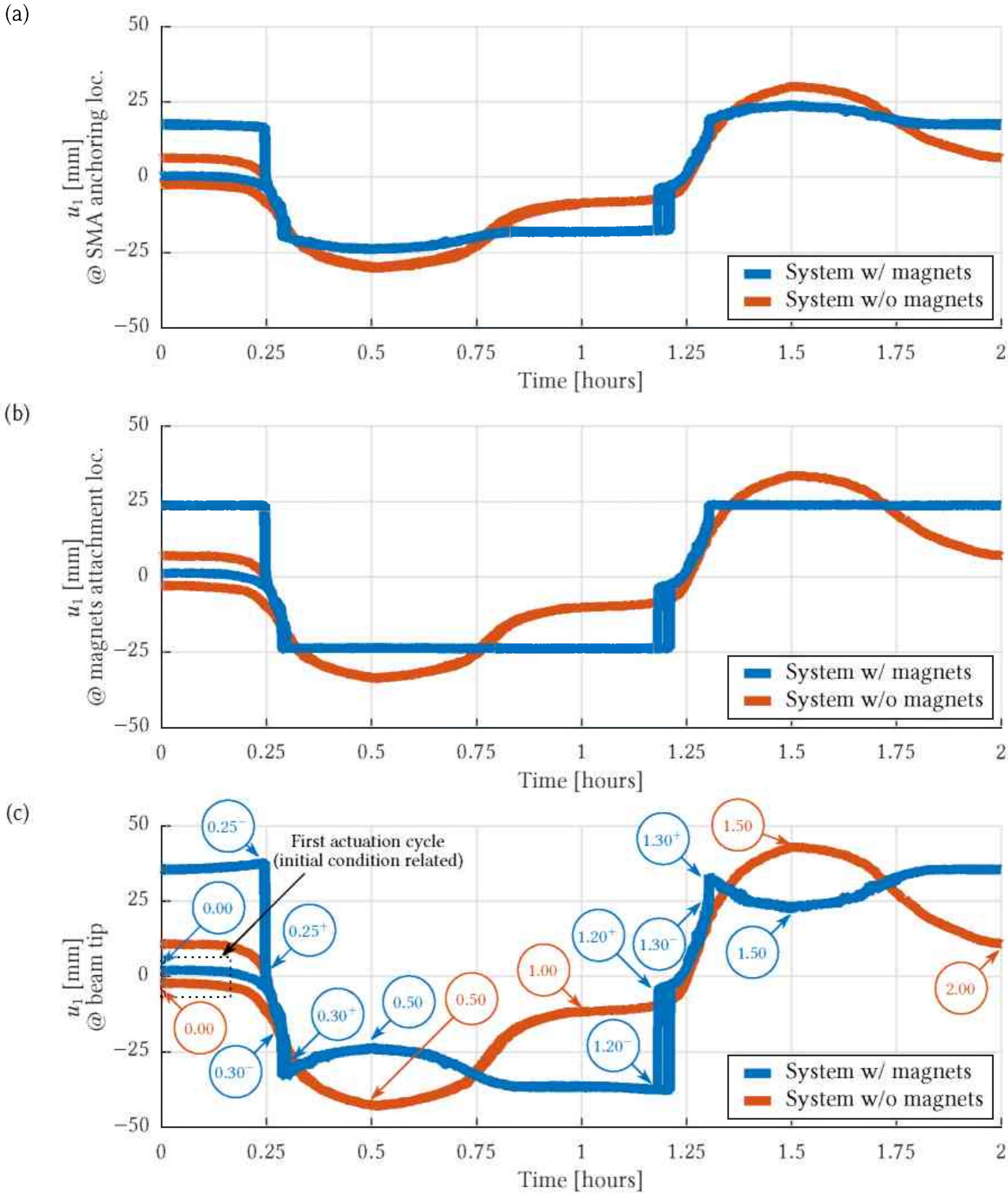

Figure 4.5 – Comparison between experimentally measured beam displacements for the system with and without magnets

(0 to 2 hours, and 2 to 4 hours) are associated with the same command voltages used for SMA actuation. Analogous reasoning is applied for the subsequent actuation cycles as well.

Furthermore, because the beam was close to a vertical position in the initial configuration for the tests that have been performed, distinct displacement paths can be seen for the

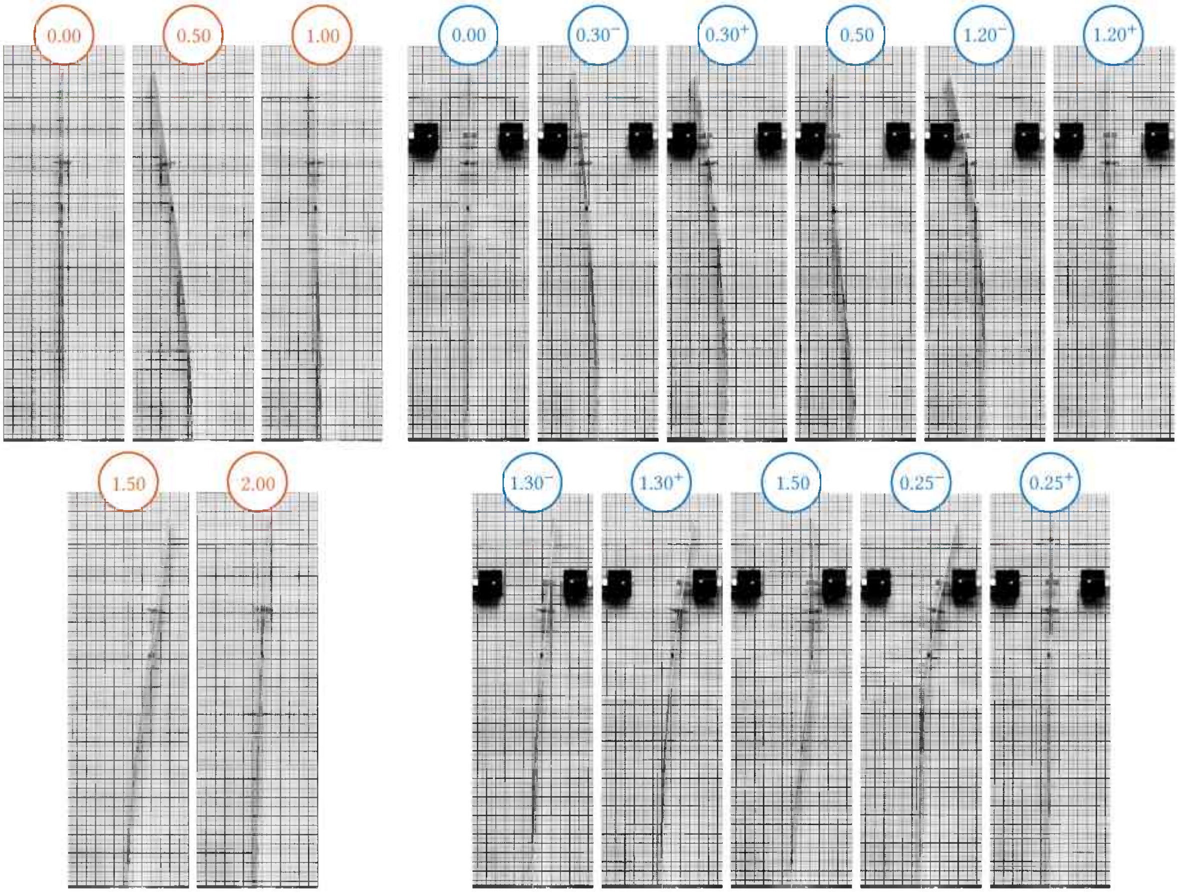

(a) System without magnets

(b) System with magnets

Figure 4.6 – System under test, at different actuation conditions, labeled according to time, in hours, cf. Fig. 4.5(c)

initial 20 minutes ≈ 0.33 h in the time histories that have been provided. An indication of this is only given in Fig. 4.5(c), despite the same being also true for all other provided plots.

Another valid clarification is in order for the line thicknesses that have been used in the plots shown in Fig. 4.5. These have been chosen so as to represent the maximum uncertainty associated with the measurements that have been made. The reasonably high variability is in account of the adoption of a camera setup, in conjunction with the use of an image tracking software, for the computation of the displacement field for the points of interest.

After these explanations, attention is finally devoted to discussion. It is directly evident from Fig. 4.5 that the permanent magnets are indeed able to provide two new equilibrium configurations for the system that has been tested. These are virtually similar to the configurations identified by the labels 1.20^- and 0.25^- shown in Fig. 4.6(b).

Another inference from the results given in Figs. 4.5 and 4.6 is that the system without magnets is able to achieve larger displacements when compared with the system with permanent magnets. This observation is directly related to the positions chosen for the placement of the permanent magnets. When a pair gets in contact, the motion of the beam is effectively constrained. Additional differences occurring after further actuation of the SMA wires can also be explained based on this observation. Nevertheless, in an actual use case of the tristable system, actuation would be interrupted just after the system had been moved to one of its stable configurations. Subsequent actuation could still be used as a means for controlling the stiffness of the structure in response to external actions, but is not required for maintaining the system in one of its new stable states.

A timeline of events is now considered for the two configurations adopted for the system. The one without permanent magnets is considered first.

The sequence is pretty straightforward, as the beam acts in response to the SMA wire actuators. The system departs from its initial condition shown in Fig. 4.6(a), labeled 0.00. The left SMA wire actuator is heated up due to the voltage that is supplied to it. In this process, because of the specific properties of the SMA wires that have been used, the material undergo phase transformation, departing from its martensite phase, aiming to arrive at a pure austenite condition. Simultaneously, the right SMA wire gets tensioned, and because of this, the tension on the left wire also rises. As a consequence, the transformation temperature for the left SMA wire gets increasingly larger as it contracts upon actuation. Much probably, a full austenite condition is not reached because of this. The maximum displacement condition is then achieved, which is shown in Fig. 4.6(a), identified by the label 0.50. From this point on, the left actuator has its temperature decreased, as a consequence of the decreasing value for the supplied actuation voltage. The beam starts to return to its initial position, but ends up in a slightly offset condition, identified by the label 1.00 in Fig. 4.6(a).

In the sequence, the same procedure is considered, but this time the right SMA actuator is the one that gets heated. It contracts due to phase transformation, while the left wire gets tensioned. The maximum displacement configuration, identified by the label 1.50 in Fig. 4.6(a), is eventually reached. Afterwards, the command voltage supplied to the right actuator is incrementally decreased. Its length starts increasing while the tension on the left wire gets reduced. An offset condition is once more achieved, which is identified in Fig. 4.6(a) by the label 2.00. From this configuration, another actuation cycle starts, leading the system once again through the states labeled 0.50, 1.00, 1.50, and 2.00, successively, regardless of the observed offsets in the configurations labeled 1.00 and 2.00.

The reason for the offset observed in the configuration labeled 1.00 in Fig. 4.6(a) can be attributed to several factors, but the most likely one considers an insufficient initial wire tension to promote full martensite reorientation of the SMA wires. Because of this, the right SMA wire still had some residual detwinned martensite after the initial setup of the experiment. Then, when the left actuator was heated up, and the right wire was further tensioned, this latter finally had martensite reorientation completed. When unloaded, an increased amount of prestrain should be associated with the right SMA wire, the effect of which appears in the considered offset. A more detailed explanation of this process can be found in the literature, for instance in the work of Sofla, Elzey, and Wadley (2008). The same reasoning explains the offset observed for the configuration identified by the label 2.00 in Fig. 4.6(a).

The timeline of the experiments performed with the system with permanent magnets is now addressed. It departs from the initial condition labeled 0.00 in Fig. 4.6(b). During the first half-hour, the left wire is heated, and contracts due to phase transformation. However, after the first initial 18 minutes of testing, the system experiences a snap-through, which is induced by the close proximity of the left pair of permanent magnets. The configurations immediately before and after contact between the NdFeB magnets can be seen in Fig. 4.6(b), and are labeled 0.30^{-} and 0.30^{+}, respectively. At this point, actuation could be interrupted, and the system would maintain its configuration. Nonetheless, the voltage supplied to the left SMA actuator continued to rise, since the same command voltage has been considered for response characterization of the system both with and without attached permanent magnets.

From this instant onward, the beam behaves as if it was constrained at the location where the magnet pair makes contact. Noticing that the SMA actuators were secured below the location at which magnets were attached to the beam, upon further contraction of the left wire, the beam tip starts to bend in the opposite direction. When the maximum command voltage is used, the beam shape is similar to an elongated “S”, which is identified by the label 0.50 in Fig. 4.6(b). In the sequence, the voltage provided for actuation is continually reduced, until it finally reaches a null value. The system, nevertheless, is able to maintain its new equilibrium state, thanks to the interacting pair of permanent magnets on the left. A picture for the 1 hour mark from the beginning of test is not provided in Fig 4.6(b), but the deformed configuration of the system at this time instant is almost identical to the one identified by the label 1.20^{-}.

Subsequently, the right SMA wire is actuated, much in the same way. After enough tension builds up due to its contraction, owed to phase transformation, the magnets that previously got together are able to separate. Configurations immediately before and after the snap-through are identified by the labels 1.20^{-} and 1.20^{+}, respectively, in Fig. 4.6(b). The voltage supplied to the right wire actuator then continues to increase, and the system eventually snaps-through one more time, when the permanent magnets on the right get too close to each other. The magnetic interaction is then able to overcome the beam restoring loads and the left SMA wire tension, so that the system departs from the configuration labeled 1.30^{-} to the one identified by the label 1.30^{+} in Fig. 4.6(b). The right SMA wire is still fed with increasing values of command voltage, until the configuration identified by the label 1.50 is achieved. Then, the command voltage starts to get reduced, until it reaches a null value once again. The system is able to maintain its new stable state, in which the beam is displaced to the right. At the 2 hours mark, the deformed configuration is virtually identical to that one identified by 0.25^{-} in Fig. 4.6(b).

Afterwards, the second actuation cycle is initiated. Differences with respect to the first actuation cycle are related to the initial condition assumed for the system. In that case, the beam configuration was almost straight, aligned to the vertical direction, and now it is deformed to the right. Because of this, when the left wire is heated, sufficient tension builds up, until the right pair of contacting magnets separate. This can be seen in Fig. 4.6(b) through the configurations labeled 0.25^{-} and 0.25^{+}. From this instant onward, the events considered previously start to occur once again, as can be checked by the overlapping curves shown in the plots of Fig. 4.5.

One important remark about the snap-through events that have been observed during experimental testing is related to vibrations. These have manifested more prominently when two contacting magnets detached, rather than when two magnets mutually attracted each other. No indication of vibratory motion appear in any of the displacement plots provided in this Chapter simply because of the sampling rate associated with the camera setup that have been used for image acquisition. Nevertheless, during testing it has been verified that the vibration just reported faded away very quickly. These indicate that inertial effects can clearly play a significant role in the case of faster SMA actuation times.

After having gone through this long explanation of experimental events, figures provided next compare numerical simulation results to the data collected experimentally. To allow for better interpretation, results are initially provided and discussed for the system without magnets. Later, the system with attached magnets is considered.

Figure 4.7 shows the displacements of the three distinct points along the beam length that have been considered previously: the location at which SMA wire actuators are attached to the beam; the location where permanent magnets are secured to the beam; and the beam tip. As can be seen by the provided plots, the displacements predicted by the numerical model present a good agreement with the collected experimental data, both qualitatively and quantitatively. The main differences that can be observed occur during SMA actuation, and are related to the phase transformation evolution law assumed by the adopted model.

Figure 4.8 shows the electric power provided for actuation of the SMA wires via Joule heating. As discussed in Section 4.2, the experimental values for power have been fitted, and the resulting expressions were used as inputs in the computation of numerical results. The fitted expressions for both input powers have been provided in Eqs. (4.1) – (4.4); a very good agreement has been achieved, as can be seen in the shown plots.

To get a better picture of the SMA phase transformation behavior, power versus displacement hysteresis loops are provided in Fig. 4.9. The plots show that the model adopted for the SMA wire constitutive behavior is able to predict hysteresis, but with some limitations. For instance, the numerical model displacements do not change past a certain electric power level ($>$ 17 W) because phase transformation had finished, which is not the case for experimental results. In this regard, transformation smoothing techniques could be adopted for the achievement of better agreement. The lack of a proper characterization of the SMA actuators also contribute to some extent for the disagreements that can be seen.

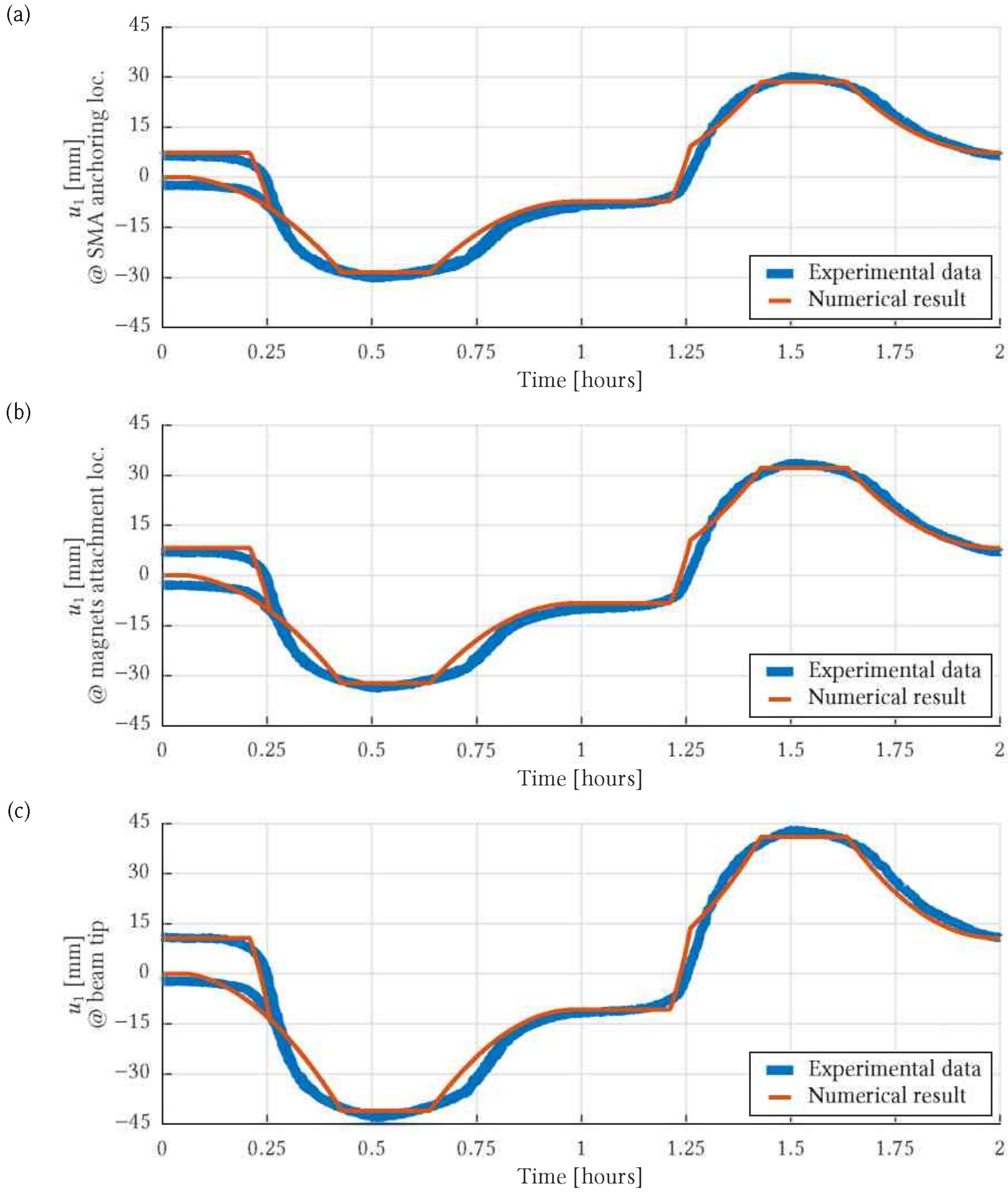

Figure 4.7 – Experimental and numerically computed beam displacements for the system without magnets

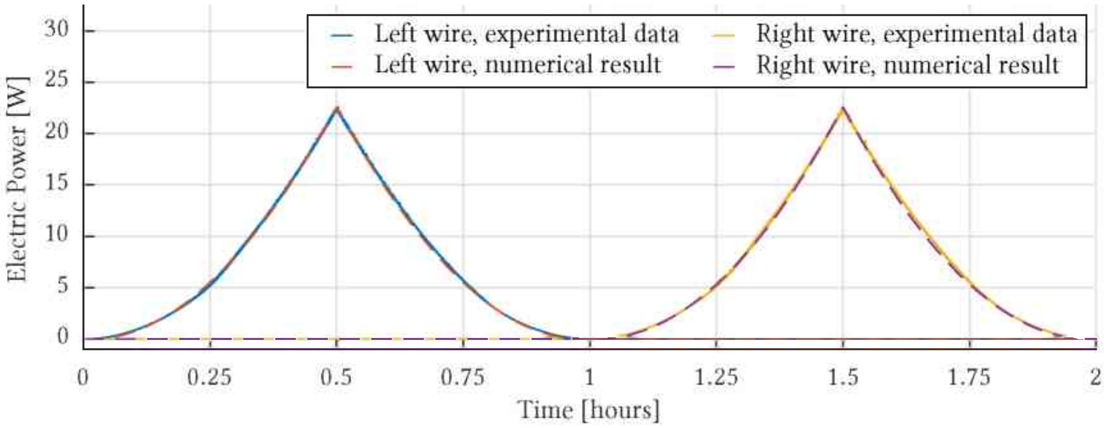

Figure 4.8 – Electric power input for the system without magnets

The electrical resistance of each SMA wire has been computed by dividing the measured voltage by the corresponding measured current observed during the SMA actuation cycles. Figure 4.10 provides plots of their time history, as well as of their relationship against the SMA anchoring point displacement. High uncertainty can be observed near the time instants of 0, 1 and 2 hours, because in these cases the current value gets very small as a consequence of the command voltage being driven towards a null value. Furthermore, because voltage was supplied only for the wire which was being actuated, there is no available data for the right wire resistance during the time period between 0 and 1 hour, neither for the left wire for instants comprehended between the 1 and 2 hour marks. It should also be noticed that, for clarity, effects related to the initial condition, which would appear during the 0 to ≈ 0.30 h time frame, have been omitted in both plots. Because of the insufficient prestress that has been considered during the experimental setup, which led to the offsets seen in the displacement results, as discussed previously, a small amount of hysteresis appear in Fig. 4.10(b). In an ideal setup, with increased initial prestress, the resistance versus displacement relationship would be almost linear for each of the SMA wires. This fact could be used for self-sensing, and control design, as has been reported in the literature, for example, by Ma, Song, and Lee (2003), Lan and Fan (2010a), and Lan and Fan (2010b).

The last results related to the condition in which permanent magnets were not attached to the system refer to the temperatures of the SMA wire actuators. Figure 4.11 provides both

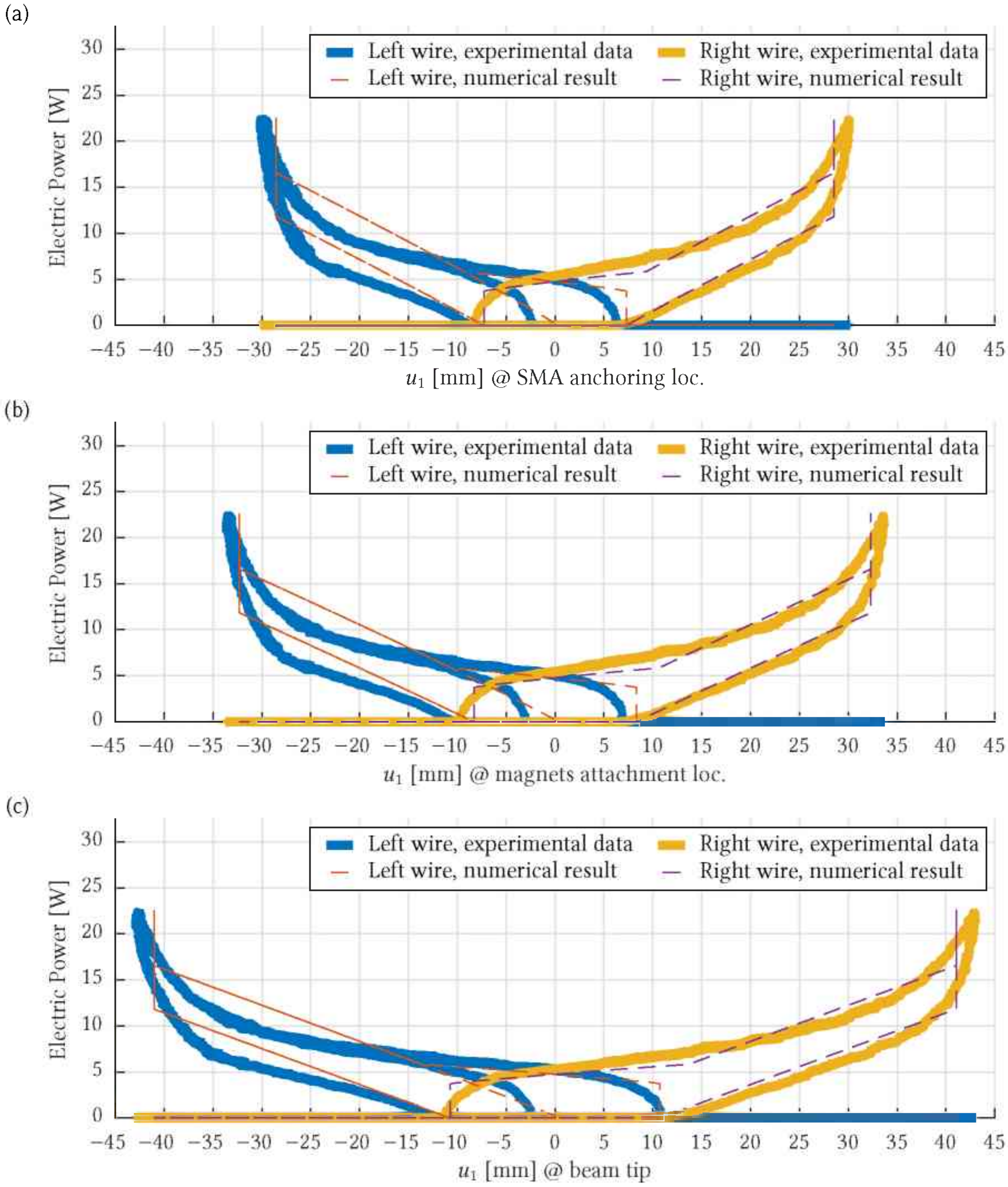

Figure 4.9 – Experimental and numerically computed electric power–displacement hysteresis loops for the system without magnets

the temperature time history and the temperature versus electrical power relationship. Agreement of numerical and experimental results is fairly good, as should be expected, since the value for the convective film coefficient h has been determined from a linear fit while considering the data shown in Fig. 4.11(b). The experimental temperature measurements are relatively noisy in account of the trouble involved in proper positioning of the thermocouples, since the

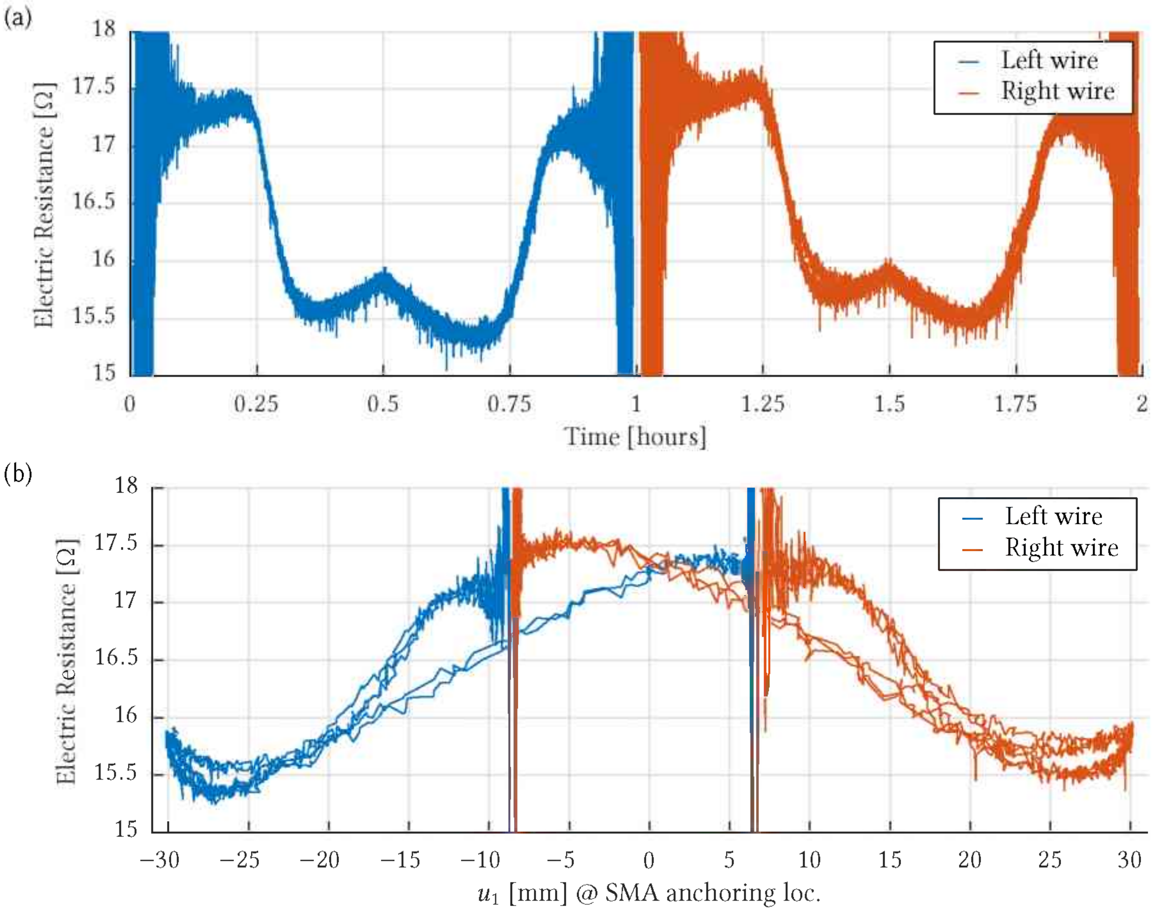

Figure 4.10 – Resistance time history, and resistance–displacement hysteresis loop for the system without magnets

SMA wires are relatively thin. This task has been made easier through the use of electrically non conductive thermal paste, but fluctuations still persisted in the measurements. Certainly, convection heat transfer might also be responsible for these.

Numerical and experimental results related to the condition in which permanent magnets were attached to the system are now considered and compared. Figure 4.12 initially provides the time history of the displacements of the SMA anchoring point, the magnets' attachment location, and the beam tip. Fairly good qualitative predictions are made by the numerical model. An exception can be pointed out for the instants at which the system experiences snap-through, which are over-predicted by the model. A possible explanation for this finding is related to the phase transformation behavior associated with the SMA constitutive model, which has been previously seen to be in some disagreement with the experimental results shown, for example, in Fig. 4.9.

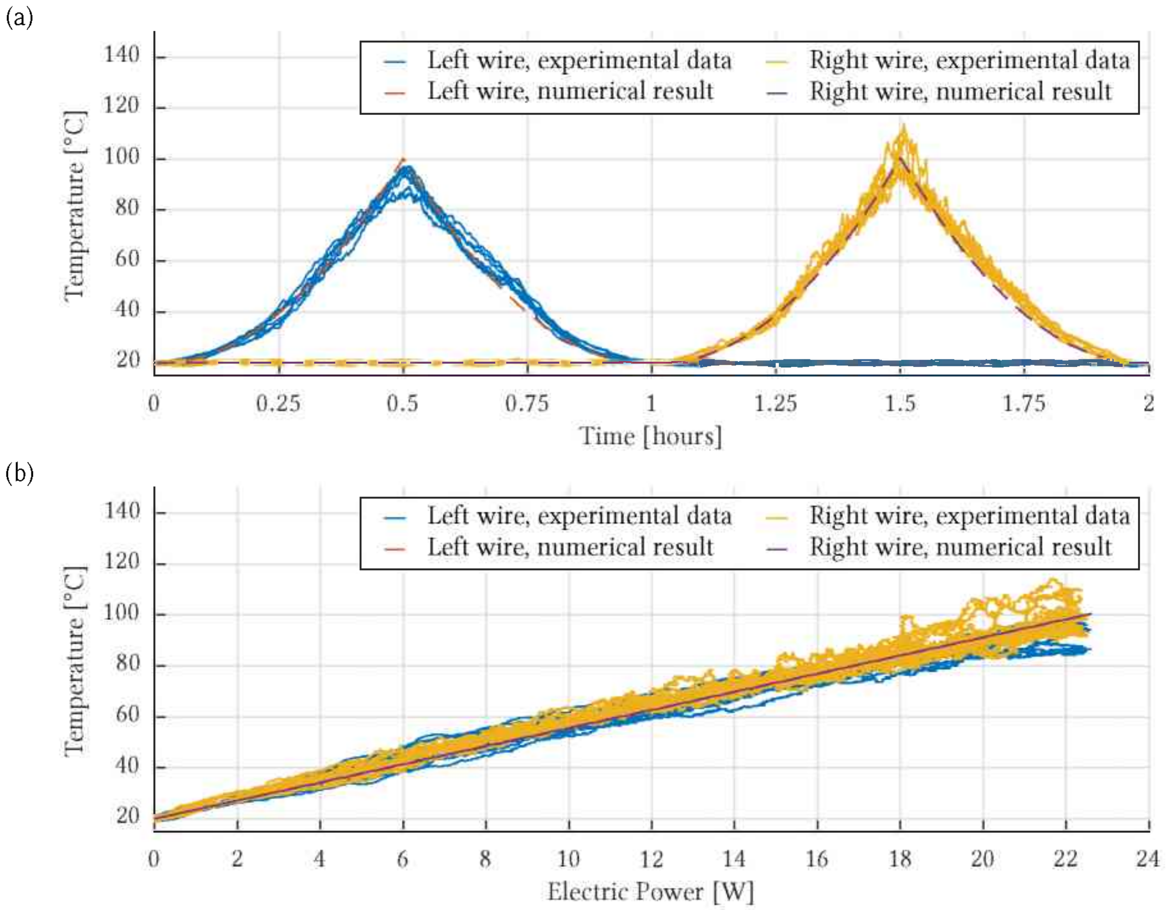

Figure 4.11 – Temperature time history, and temperature–electric power relationship for the system without magnets

Another possible issue related to the numerical predictions could bear foundation in the model adopted for the interaction between permanent magnets. Since it has been thoroughly tested against data provided by several papers available in the literature (AKOUN; YONNET, 1984; YONNET; ALLAG, 2009; ALLAG; YONNET, 2009; JANSSEN et al., 2009), this reasoning has been almost completely ruled out. Uncertainty related to the actual residual magnetization of the permanent magnets is the only possibility that would require further investigations. As the magnets have been acquired from a reputable provider (K&JMAGNETICS, 2017), and are classified according to a reliable grading system, it becomes very difficult to believe that this is the real reason behind the poor predictions of the snap-through events by the numerical model. In fact, these considerations suggest even more that the inconsistencies observed for the SMA phase transformation behavior (cf. Fig. 4.9) are the real culprit for the over-prediction of the snap-through conditions.

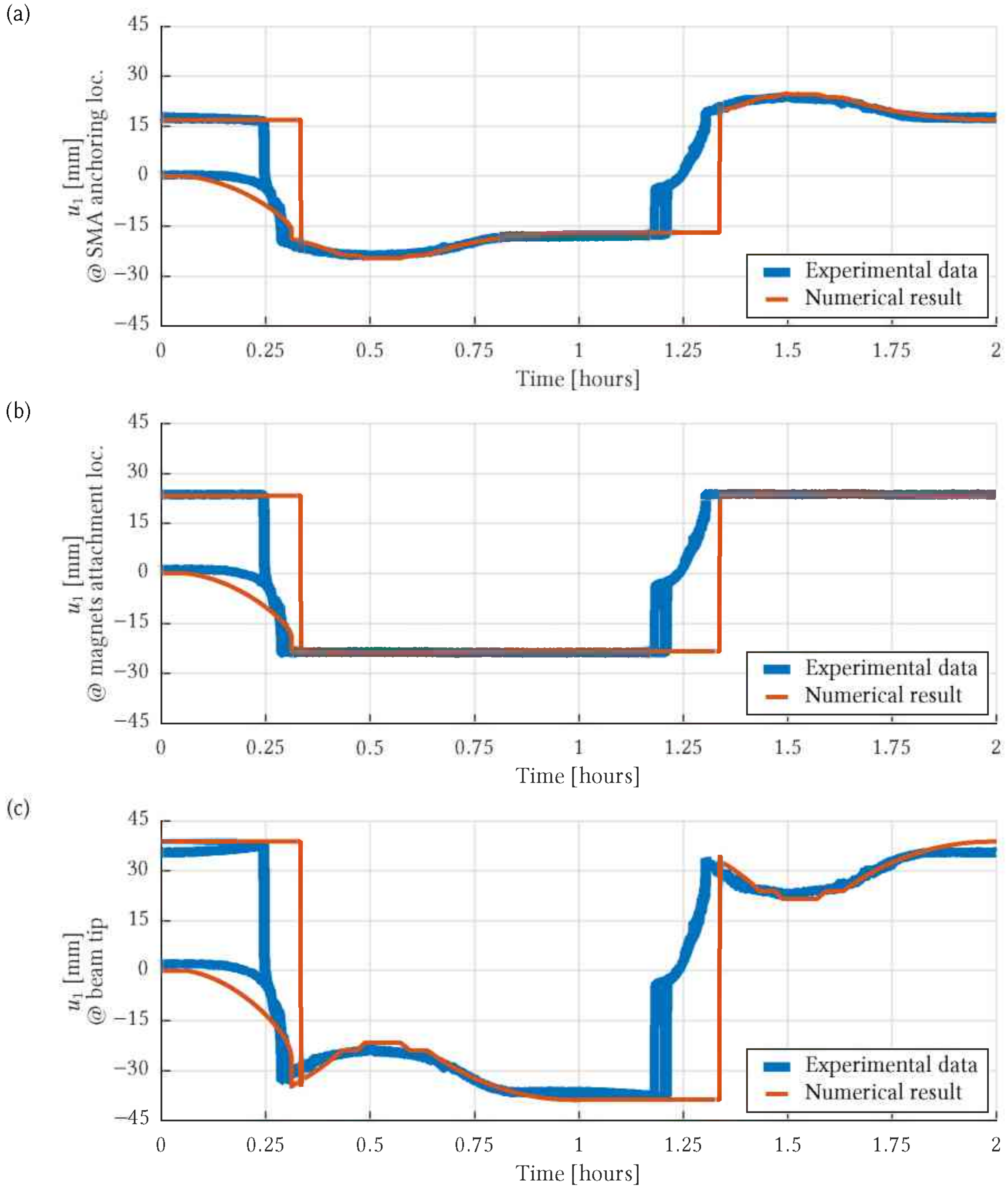

Figure 4.12 – Experimental and numerically computed beam displacements for the system with magnets

Nevertheless, since proper characterization of the SMA wire actuators has not been performed, conclusions can not be drawn in this regard. For instance, one recalls that some SMA-related parameters shown in Tab. 4.2 were identified while considering experimental results obtained when permanent magnets were not attached to the beam. Then, it consists of a possibility that the identified parameters are not representative of the actual behavior of the SMA material at hand. It should be expected, therefore, for numerical results to not be in complete agreement with experimentally obtained data for the condition in which permanent magnets were attached to the beam.

The electric powers used for actuation when permanent magnets were attached to the system are shown in Figure 4.13. The behavior is identical to the one presented previously in Fig. 4.8. Once again it can se been that the electric powers used for computation of numerical results match perfectly those measured experimentally.

Figure 4.14 considers the electric power as a function of the system displacements. Because of its multistability, it can be seen that the structure is able to stay at deformed configurations with no consumption of external power. For instance, the beam tip can be maintained displaced by amounts of approximately ±37 mm. Because of the small offsets that appeared during experimental testing near the vertical configuration of the beam, it is also possible for it to be positioned at any location within ±11 mm of tip displacement. These configurations can also be attained by the system without permanent magnets, as can be perceived by analysis of Fig. 4.9. More importantly, it can be seen from this same figure that a beam displacement of ±37 mm can only be achieved, for the system without permanent magnets, at the expense of roughly 7 or 12 W, depending if the SMA wire actuator is going through forward or reverse phase transformation, respectively. If this configuration needs to be maintained for longer periods of time, significant energy savings can be obtained by adopting the multistable design.

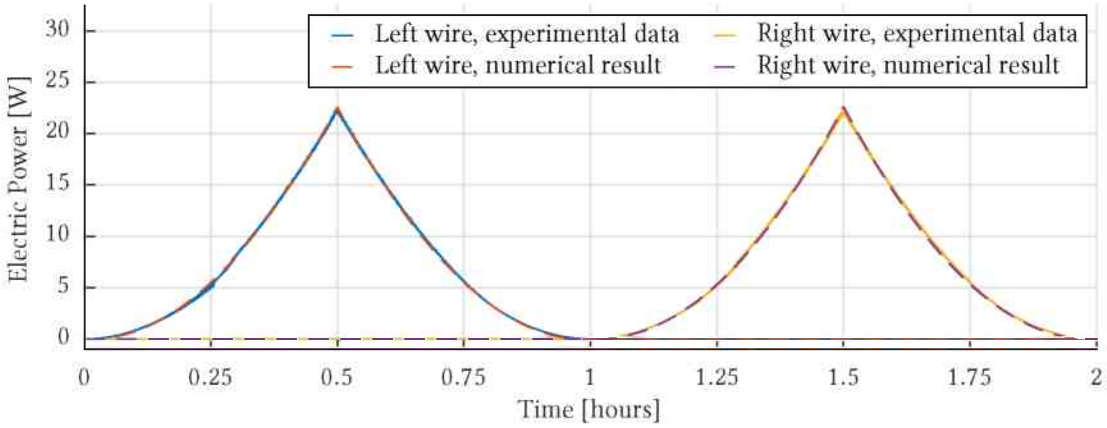

Figure 4.13 – Electric power input for the system with magnets

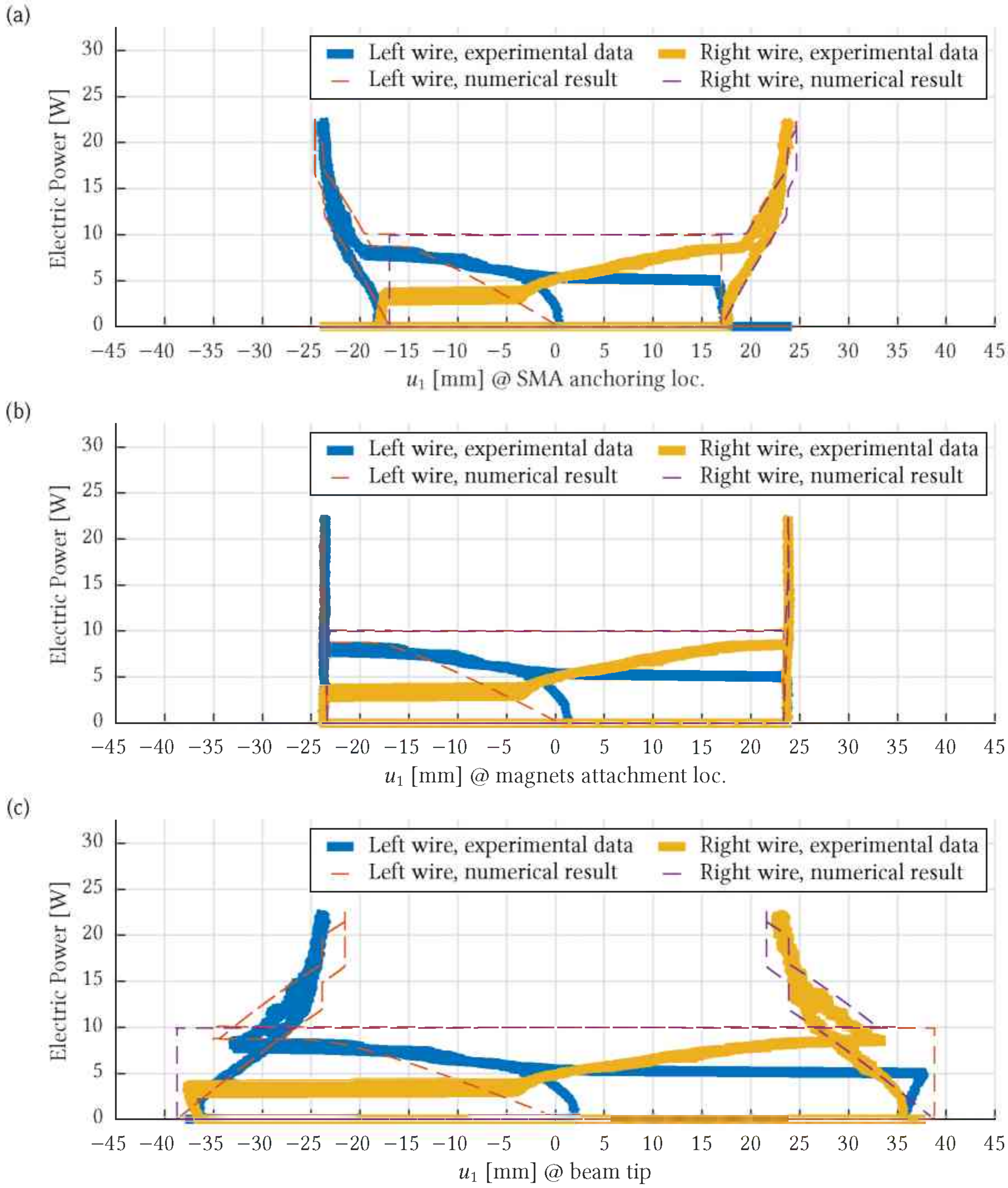

Figure 4.14 – Experimental and numerically computed electric power–displacement hysteresis loops for the system with magnets

Of course, the power-related numbers just provided are concerned with an SMA wire length of more than 1.3 m. Nevertheless, this does not change the fact that around 90% of the energy used for actuation is actually lost in the form of heat, as the typical efficiency of SMA actuators is below 10%.

The electrical resistances of the SMA wire actuators is provided in Fig. 4.15 for the case in which the system is equipped with permanent magnets. Both the time history and the relationship between electric resistance and the displacement of the SMA anchoring location are shown. The effects of the initial condition that appear on the first actuation cycle have been omitted for clarity. In the time history plot, it can be seen that jumps occur in the electrical resistance, which are due to the snap-throughs the structure is subjected to. It can be verified that these jumps are synchronized with those occurring in the displacement response, cf. Fig. 4.12(a). The electrical resistance relationship with the displacement bears little resemblance with the one previously seen in Fig. 4.10(b). It can be verified that regions of almost linear relationship exist between −2 and −18 mm for the left wire, and between −3 and 17 mm for the right wire. It can also be seen that the electrical resistance and displacement jumps are in full synchronism as well, since horizontal and vertical jumps do not occur in Fig. 4.15(b).

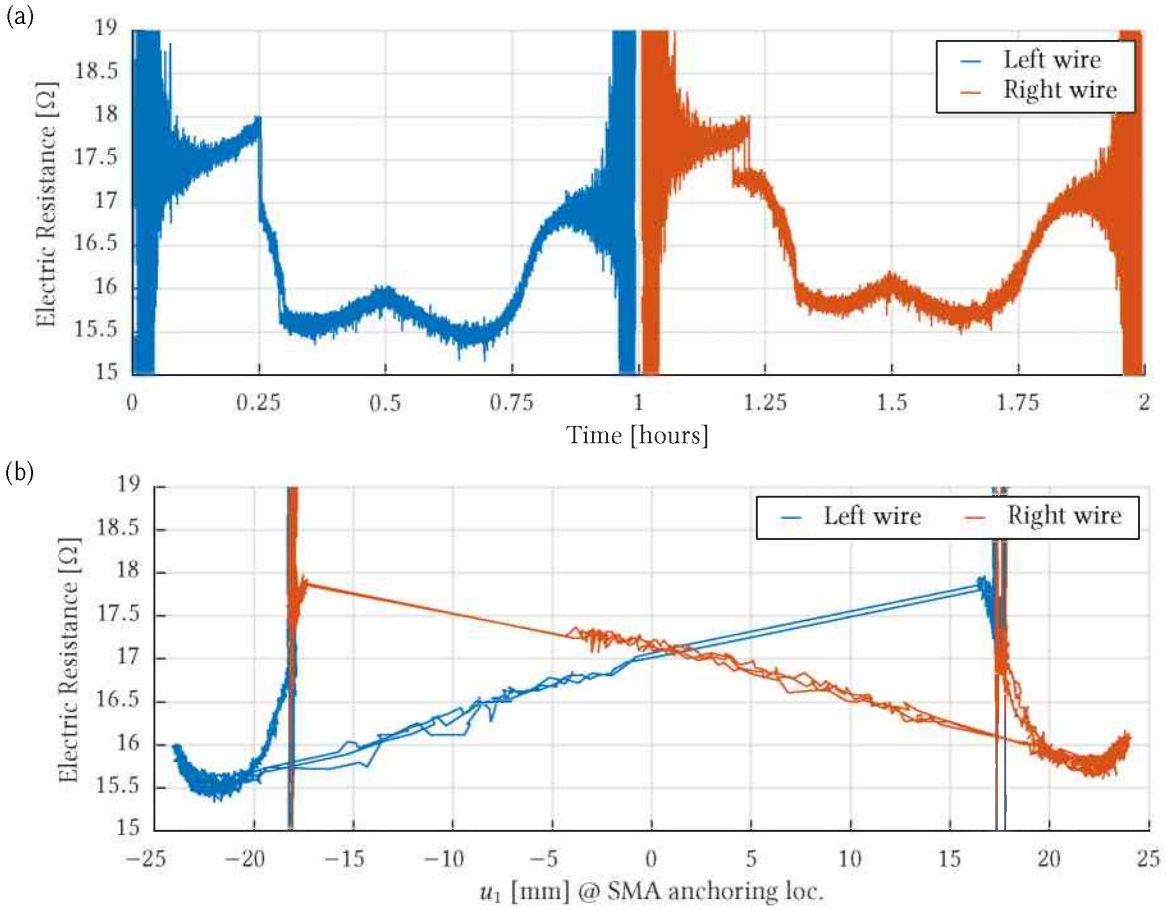

Figure 4.15 – Resistance time history, and resistance–displacement hysteresis loop for the system with magnets

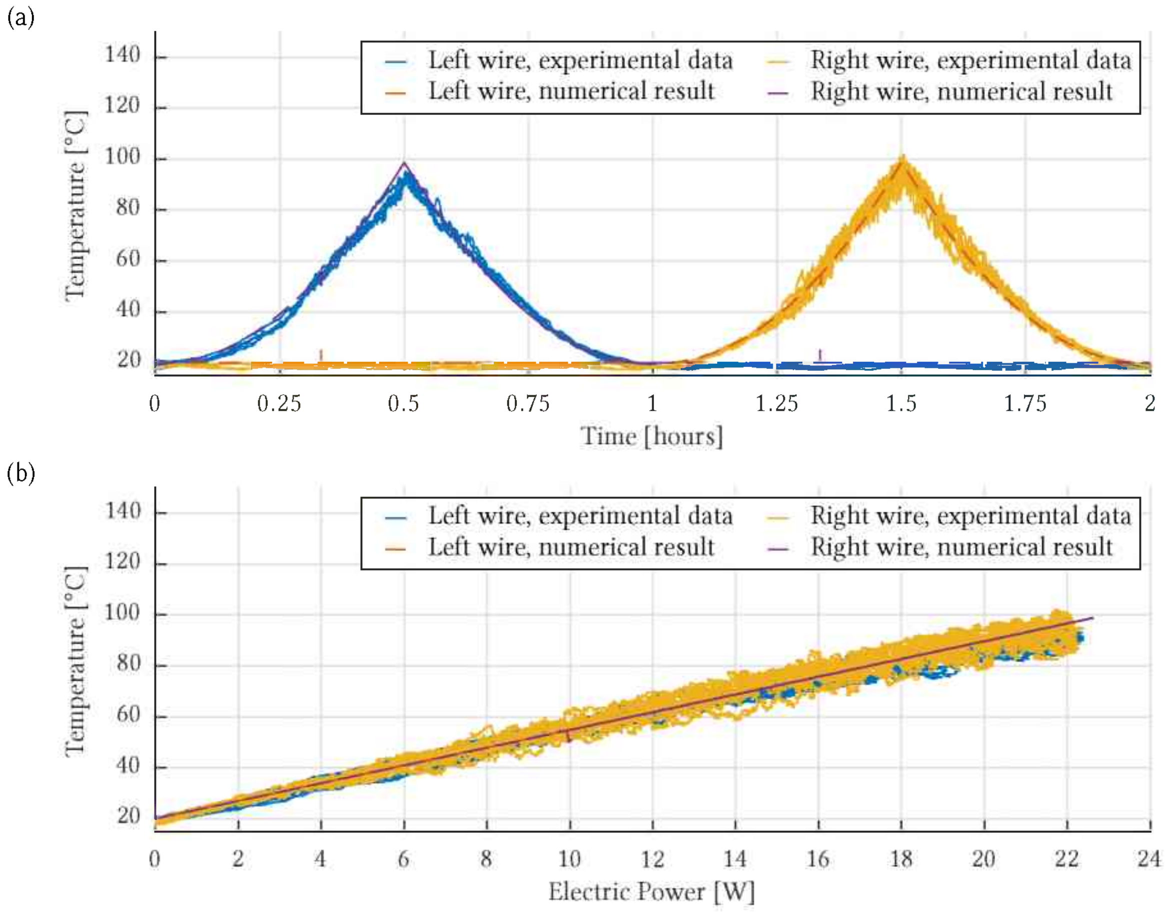

Figure 4.16 – Temperature time history, and temperature–electric power relationship for the system with magnets

The behavior seen in this plot makes one believe that self-sensing, while possible to some extent, in principle, would be of limited use. One potential application in which it can be useful though is in determining the stable state in which the system finds itself in.

Temperatures of the SMA wire actuators for the case in which magnets were attached to beam are finally provided in Fig. 4.16. The behavior is similar, if not identical, to the one seen in Fig. 4.11, for the case in which no magnets were added to the system. Numerical predictions are in good agreement with the experimental data for this case as well.

4.4 Summary

Albeit the system considered in this Chapter is of an illustrative purpose, it permitted one to verify that multistability can be achieved through the simultaneous use of SMA wire actuators and permanent magnets. It could be seen that the multistable behavior arises because of the interaction between NdFeB magnets. The resulting magnetic loads are able to successfully counteract the elastic restoring loads due to the beam itself, and to an SMA actuator arranged in an antagonistic manner. It has also been shown that SMA actuators were able to move the system between the distinct stable configurations it acquired after permanent magnets were added to it.

A diminished prestress level applied to the SMA actuators has been pointed out as a possible cause for offsets observed in experimental displacements. Higher prestress levels could have certainly been considered. This has not been done, however, to prevent the exposure of the SMA wire actuators to over-stress conditions during the experiments. The antagonistic arrangement that has been considered already led to significant stress levels during the tests that have been performed.

Another issue that has been reported is related to small vibrations that occurred during system snap-through. To prevent these, damping mechanisms would need to be added to the system. Modification of inertia properties might also be of interest in this respect.

The numerical modeling procedure proposed in the previous Chapter has been shown to accurately represent the system at hand. Deviations have been seen in the form of over-predictions for the conditions necessary for snap-through. These have been attributed: to the phase transformation law adopted in the SMA constitutive model, which can be improved, for instance, while considering smoothing strategies; as well as to the lack of previous characterization of the SMA material. Further investigations seem necessary for pinpointing the real reason behind the reported behavior.

Some asymmetries can also be seen in the experimental results that have been provided, although none of these have been discussed thus far. They are considered to be acceptable, since no special caution has been taken to ensure precise positioning of components during experimental setup. For instance, one of the SMA actuators might actually be slightly longer than the other.

CHAPTER V

DESIGN OF A MORPHING UNIT CELL AND ITS USE IN A THREE CELL MORPHING BEAM METASTRUCTURE

In the previous Chapter it has been shown that SMA actuators can be simultaneously used with permanent magnets for achieving a multistable smart structure. Now this concept is used in the proposition of a unit cell arrangement that is later adopted in the construction of a morphing beam metastructure.

Aspects related to the design of the proposed morphing unit cell are presented in Section 5.1. Next, in Section 5.2, topics related to fabrication and assembly of prototypes are addressed. The experimental setup is detailed in Section 5.3, and results are discussed in Section 5.4. Finally, a summary and conclusions are provided in Section 5.5.

5.1 Morphing Unit Cell Design

Figure 5.1 displays an schematic representation of the geometry adopted for the proposed unit cell. Its layout is based on the use of a rotational compliant joint. SMA actuators are used to displace the structure from its neutral position. Permanent magnets, which are shown in gray, are used to introduce two new stable equilibrium configurations in the system. The values of the geometric parameters and the coordinate locations for the final unit cell configuration are given in Tabs. 5.1 and 5.2, respectively; its width is equal to 10 mm.

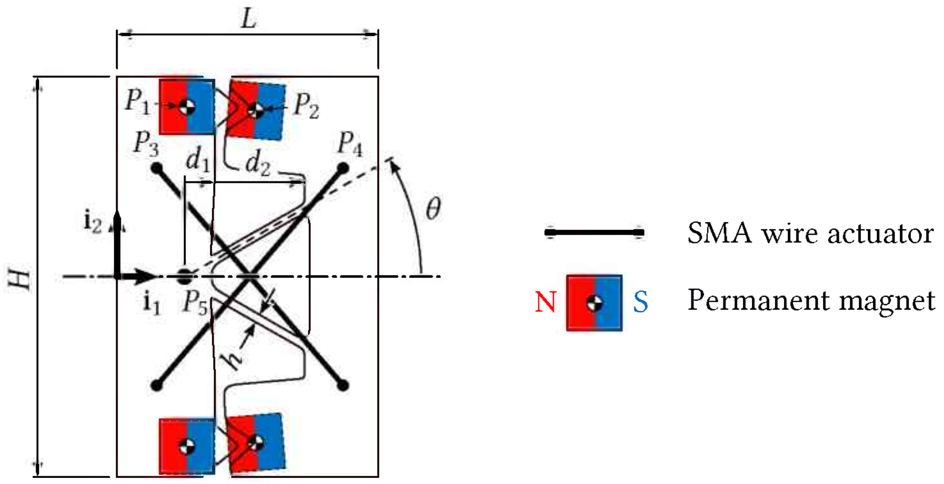

Figure 5.1 – Geometry of the proposed unit cell

Some aspects that deserve explanation are related to the selection of a compliant hinge for the design; the arrangement adopted for the SMA wires; and the positioning of permanent magnets. These are discussed in the following.

First, one considers the selection of the compliant hinge. A review on the matter has been recently presented by Machekposhti, Tolou, and Herder (2015). According to the authors, compliant mechanisms have the advantage of being monolithic (i.e. one piece), since hinges are not used in their design. As a result, it is possible to obtain reduced wear, friction and backlash, while maintaining increased mechanism precision. Reduced weight and motion smoothness are yet another benefits of flexure pivots. These aspects have motivated the selection of a compliant architecture instead of a hinged one. Nevertheless, it is also possible to conceive a morphing unit cell based on such type of construction.

Table 5.1 – Values of the geometric parameters shown in Fig. 5.1

Parameter	Value	Units
d_1	3	mm
d_2	12	mm
θ	30	°
h	0.75	mm
L	30	mm
H	48	mm

Table 5.2 – Coordinates of the points identified in Fig. 5.1

Point	X_1 [mm]	X_2 [mm]
P_1	6.825	20.325
P_2	14.921	19.666
P_3	3.377	12.040
P_4	25.179	12.040
P_5	6.50	0

The selection of the specific compliant joint shown in Fig. 5.1 has been made based on its simplicity. More elaborated configurations could certainly be adopted, to achieve smaller axis-drift, or larger off-axis stiffness, but these would certainly lead to more complex designs. The hinge in question consists of two leaf-type elements arranged in an isosceles-trapezoidal configuration. Studies reporting their simplified modeling and rotational precision can be found in the literature (XU et al., 2008a; XU et al., 2008b).

The design of the unit cell also considers maximum rotations limited to ±5°, which have been arbitrarily chosen. Larger values could have been selected, but the motivation for the final designs, when unit cells are combined in a beam metastructure, and in an morphing airfoil later, favors the adoption of small rotations distributed along the structure. This line of though also benefits smoother morphing shapes, since large discontinuities can be avoided. Surfaces have been designed to enter in contact and prevent rotations that are larger than the desired amount.

After having considered the reasons behind the selection of the specific compliant rotational joint seen in Fig. 5.1, aspects related to the SMA wire actuators are discussed.

In the first place, this type of actuators have been selected because one deals with morphing applications in this work, and these ask for reasonably large geometrical shape changes. As mentioned in previous Chapters, SMAs are able to recover significant amounts of strain, and provide reasonably high actuation forces. While piezoelectric actuators could in principle be used for actuation, some sort of displacement amplification mechanism would be required. This would end up leading to further complications in the design of the unit cell. The reasonably small design space that is available for integrating the unit cell in an airfoil makes the choice of piezoelectric actuators even harder to sustain, for this specific application, in the view of the author. [It should be noted, however, that successful morphing airfoil concepts, that do make use of piezoelectric actuators, have been reported in the literature (BARBARINO et al., 2011b).] Besides these two types of actuators, no other ones have been considered.

For the selection of the length, orientation and positioning of the SMA wires, the arguments that follow next have been considered.

First of all, one wanted to avoid what appears to be common practice in the design of antagonistic SMA actuation, which is to have wires placed almost parallel to each other, at large offsets from the rotation center. While this approach favors the torque provided by the actuators, it seems to be very ineffective from the actuation point of view, as the wire that is actuated has to overcome the stiffness of its antagonistic counterpart. Based on this, a setup with overlapping wires has been adopted. In this scenario, a smaller amount of axial deformation is inflicted on the opposing SMA wire during actuation. Optimization has not been performed for locating the wires inside of the available design space, and only a good guess has been considered.

A disadvantage of the proposed approach is that the wires cannot lie in the same plane. As a consequence, an offset needs to be introduced between them. In the specific case considered here, the wires are located in two distinct planes that are parallel to the one spanned by the $(\mathbf{i}_1, \mathbf{i}_2)$ basis vectors shown in Fig. 5.1. Because this offset can lead to torsion loads, an additional pair of wires is placed on the back of the unit cell, arranged symmetrically with respect to those in the front.

The length of the wires have been determined based on the amount of strain they are able to recover during phase transformation, while also accounting for the distance between the wires and the center of rotation, which is identified as P_5 in Fig. 5.1. This approach has been considered to ensure that the actuators would be able to move the unit cell through the specified rotation range of $\pm 5^\circ$.

As for the values of the geometric features related to the compliant hinge, their specification has to account for the relative orientation of the leaf beams with respect to the SMA wires. This aspect is of importance since buckling can be induced in the beam elements that compose the compliant hinge, depending on SMA wire prestress, for example.

Concerning permanent magnets, each pair was positioned such that magnetic dipoles were aligned in the deformed unit cell configurations. This reasoning allows for maximum magnetic forces in the deformed states, in an attempt to improve stability in these cases.

The main issue in designing the unit cell is related to the desire for its tristability property. Difficulties appear because of the limited space considered for its design. The choice for its relatively small size is based on the dimensions assumed for the morphing airfoil that was to be produced. The small dimensions of the unit cell makes the permanent magnets interfere, rather significantly, with the original stable state of the system, in which a neutral orientation, with a rotation of 0°, is observed.

To try to improve the stability at the neutral position, higher prestress can be applied to the SMA actuators. This can lead to buckling of the compliant joint, which can also be made stiffer. However, the overall stiffness at the neutral configuration of the unit cell can not be exceedingly high, otherwise the permanent magnets would not be able to allow for the new stable configurations at $\pm 5^\circ$.

Because of these complications, a numerical model was used to verify if the geometry proposed for the unit cell had multistability. Simple simulations were considered for this purpose. The compliant joint was modeled with the SMA wires and permanent magnets. Successive rotations were imposed to the compliant joint, with the unit cell starting in its neutral position and ending in a configuration with 5° of angular displacement. This allowed the computation of the reaction torques required to maintain each of the deformed rotation states. Then, the torque versus rotation curve could be constructed. To check if the resulting unit cell configuration possessed multistability or not, it was sufficient to verify if the aforementioned curve had a maximum. In this case, a snap-through should be expected to occur for the corresponding angular displacement. Otherwise, in the lack of a maximum in the torque versus rotation curve, system modifications would be required, so that the desired behavior would be seen. These were implemented based on the knowledge gathered from previous simulations, and on relationships of cause-and-effects observed during the adjustment of geometric parameters.

Several issues with this strategy can be reported, though. For instance, the procedure has been applied without proper knowledge of material properties, which had to be considered equal to those provided in manufacturer data sheets. Other contributions for the poor performance of the strategy adopted for achieving multistability is related to experimental construction issues, that will be discussed in the following.

5.2 Fabrication and Assembly of Morphing Beam Metastructure Prototypes

Prototypes have been fabricated via 3D printing. CAD files were handled to the University of Michigan 3D Lab (`http://um3d.dc.umich.edu/`), together with printing instructions. The manager of the laboratory himself was responsible for the manufacturing process.

Three distinct versions have been proposed for the unit cell design, as can be seen in Fig. 5.2. Improvements that have been introduced along iterations of the prototypes are mainly related to the method adopted for securing the SMA wires. The prototype for which results have been gathered uses metal nuts and screws for this purpose.

The size of the permanent magnets used in the prototypes have also changed, with the last design being equipped with cuboidal magnets of side equal to 6.35 mm $\approx \frac{1}{4}$ of an inch.

The first prototype was made from ABS plastic by a fused deposition modeling printer, while the second and third ones were manufactured from a proprietary UV-curable plastic, VisiJet M3 Crystal, on a ProJet 3500 HD Max 3D printer.

The adoption of 3D printing for prototype manufacturing consists of a reason, among others, that contributed to the design challenges that have been mentioned towards the end of the last Section. While this fabrication technique allows for increased creativity during design, material properties can vary significantly depending on the orientation assumed by the part during the printing process (CAZÓN; MORER; MATEY, 2014).

While the very first manufactured prototype consisted of a single unit cell, all the following ones were based on a series arrangement of three unit cells, as can be seen in Fig. 5.3.

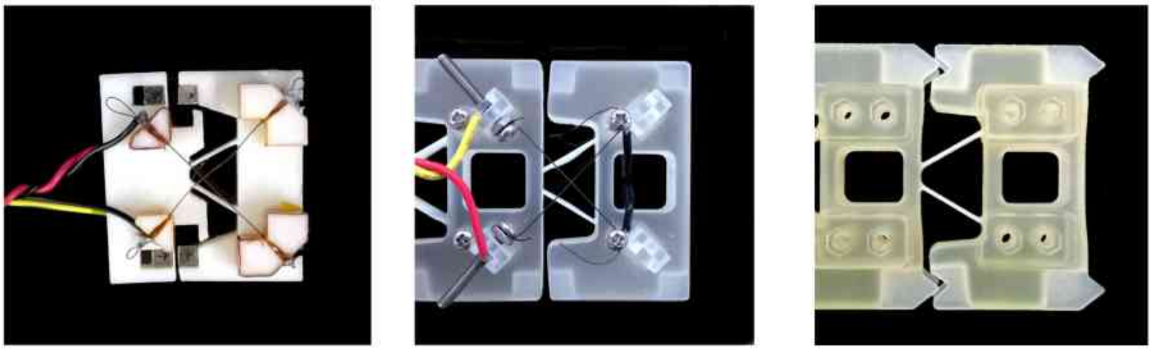
(a) 1st version (b) 2nd version (c) 3rd version

Figure 5.2 – Evolution of the design proposed for the morphing unit cell

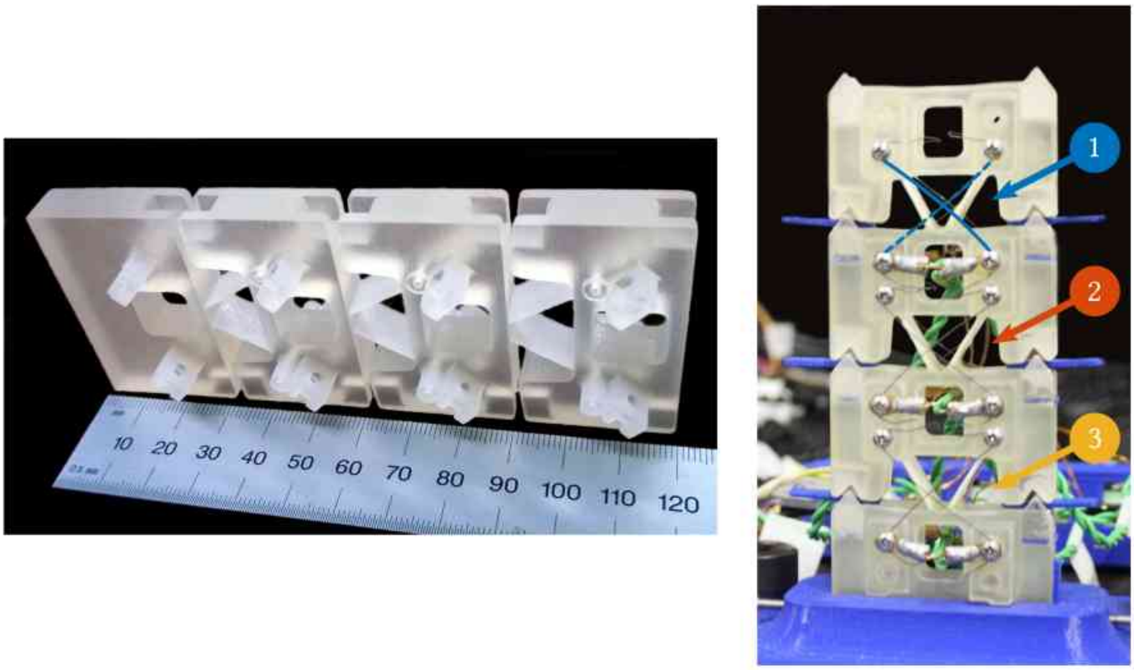

(a) 1st version, based on the unit cell shown in Fig. 5.2(b)

(b) 2nd version, based on the unit cell shown in Fig. 5.2(c)

Figure 5.3 – Morphing beam metastructure prototypes

The repetitive pattern that has been adopted allows for distributed shape morphing, and this architecture should thus see the benefits expected from distributed actuation. The unit cell and its arrangement have been thought from the beginning so that a one dimensional beam-like structure could be achieved. More complicated designs, that expand on the dimensionality and on the function of each unit cell could also be developed.

The terminology "metastructure" is adopted when one refers to structures that incorporate an array of distributed features, such as vibration resonators, for example, as has been reported by Hobeck and Inman (2017). In the specific case of this Thesis, morphing metastructures are considered, based on a 1D array of morphing unit cells.

Before considering experimental setups that have been adopted for testing, final remarks about assembly of the metastructure prototype are given. In the case of the tested version, metal nuts have been secured to the 3D printed part with Loctite® Super Glue. The hexagonal holes on which these nuts go can be seen in Fig. 5.2(c). SMA wires were then secured with the use of screws, as shown in Fig. 5.3(b). Precise control over the amount of applied prestress have not been guaranteed. Magnets were also attached with the use of Loctite® Super Glue. The prestress on the SMA wires were then manually adjusted so that multistable behavior could be observed. While some effort was spent in trying to make all the unit cells equal, some differences persisted, as results will show.

Each unit cell was equipped with 4 SMA wire actuators (two pairs electrically arranged in series), 8 nuts, and 8 screws, for a total of 12 SMA wire actuators, 24 nuts, and 24 screws for the complete metastructure. To make electrical connections easier, each SMA wire was screwed together with a ring wire terminal that had been previously crimped to electrical copper wires.

5.3 Experimental Setup

For performing the experiments that bear relationship with this Chapter, a different system has been considered for driving the SMA actuators, instead of relying on the linear power amplifier adopted in the context of Chapter IV. The new approach is based on the use of several current regulators arranged in parallel, with a single power supply being responsible for providing current to the SMA wire actuators, as is shown in Fig. 5.4.

As can be seen, each current regulator is based on the combination of a TIP121 NPN bipolar junction transistor, with a general purpose LM741 operational amplifier. Constant current operation is possible because the resistor voltage is connected to the inverting input of the LM741 component, providing negative feedback, and a control voltage is routed to its non-inverting input. Power resistors rated for 10 W operation, with 0.47 Ω, were used in each current regulator. To provide current to the SMA wire actuators, a B&K Precision® multi-range programmable DC power supply, model 9115, has been used. The LM741 amplifiers

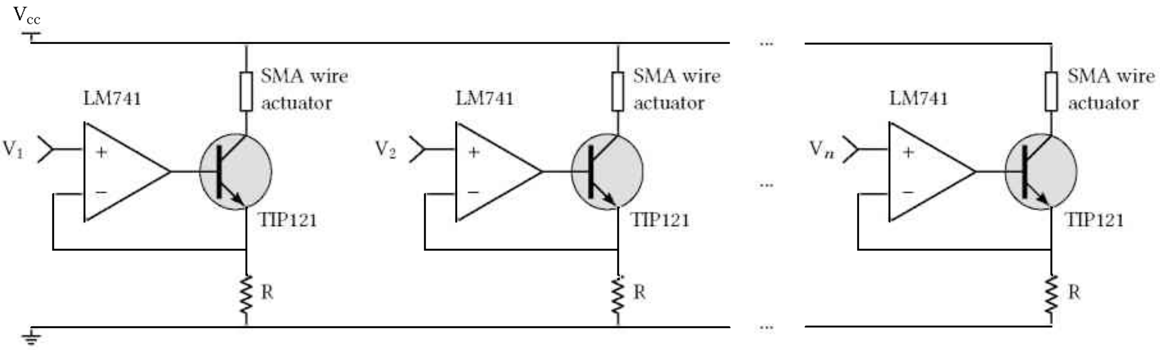

Figure 5.4 – Parallel arrangement of current regulators used for SMA actuation

have been powered with 15 V provided by a IMPAC® IP-302D supply. Prior to experiments, the behavior of each current regulator was checked with the use of a Tektronix® current probe system, models TCPA300 and TCP312.

Data gathered from the experiments include wire voltages, and the system displacement field. Voltages have been recorded with the NI® USB-6259 BNC DAQ. Displacement measurements were made by recording the experiment with a Sony® NEX-VG10 Handycam coupled to a 18–200 mm lens. Afterwards, videos were post-processed with the open source Tracker software. Its capabilities were used for tracking the positions occupied by the SMA anchoring screws through the tests. Based on these positions, the angular orientations of the unit cells have been determined experimentally.

The NI® USB-6259 BNC DAQ has also been used during the experiments to control the current sources considered in Fig. 5.4. Since this DAQ device has only four analog outputs, and SMA wires are more numerous, the arrangement shown in Fig. 5.5 was considered. In this setup, only two analog output signals, one high and the other one low, labeled AO_H and AO_L, respectively, need to be taken into account. These are routed through electromechanical relays. Their common terminal provide the control voltages V_1, V_2, ..., V_n for the LM741 operational amplifiers. For determining the common voltage value of each relay, digital output ports on the NI® DAQ are used — which are denoted by DO_1, DO_2, ..., DO_n in Fig. 5.5.

The adopted arrangement for SMA actuation introduces some limitations in the control system adopted for testing, since the wires will only be able to operate either with a low or with a high current value. However, in comparison to the alternative of using the system

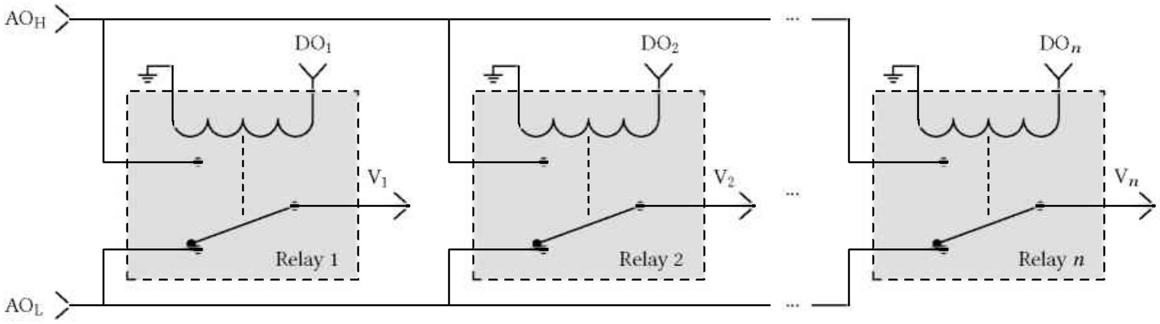

Figure 5.5 – Arrangement of electromechanical relays adopted for providing control voltages to the LM741 operational amplifiers shown in Fig. 5.4

considered in the previous Chapter, one has gained the possibility of actuating several wires simultaneously, and, more importantly, having individual control over each wire.

The adopted digital control signals have been kept the simplest. A pulse type signal has been considered, such that a high value of current is passed through the corresponding SMA wire during a defined amount of time. After this time has passed, a low current is provided to the wire with the sole purpose of monitoring its voltage.

Figure 5.6 provides a reasonably detailed look of the support hardware, while also identifying some signal cables and components of the experimental setup. Figure 5.7, on the other hand, shows a photograph that provides an overview of the test bed.

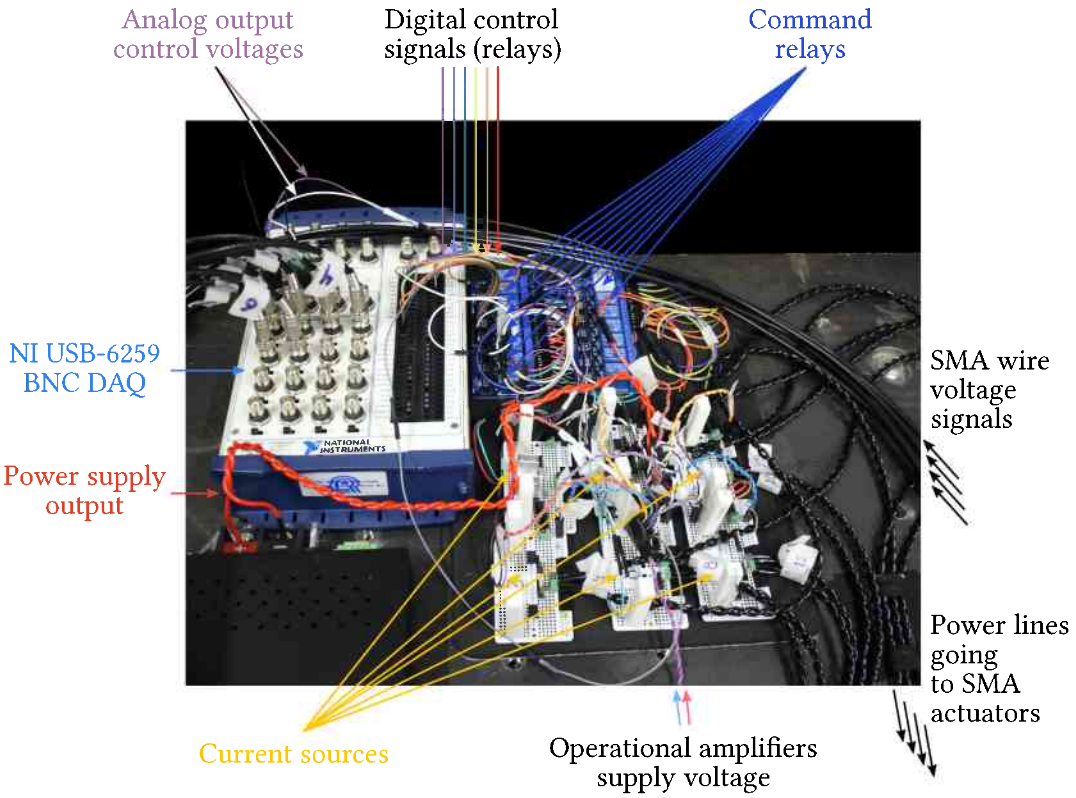

Figure 5.6 – Supporting hardware and routing of signals used during experiments

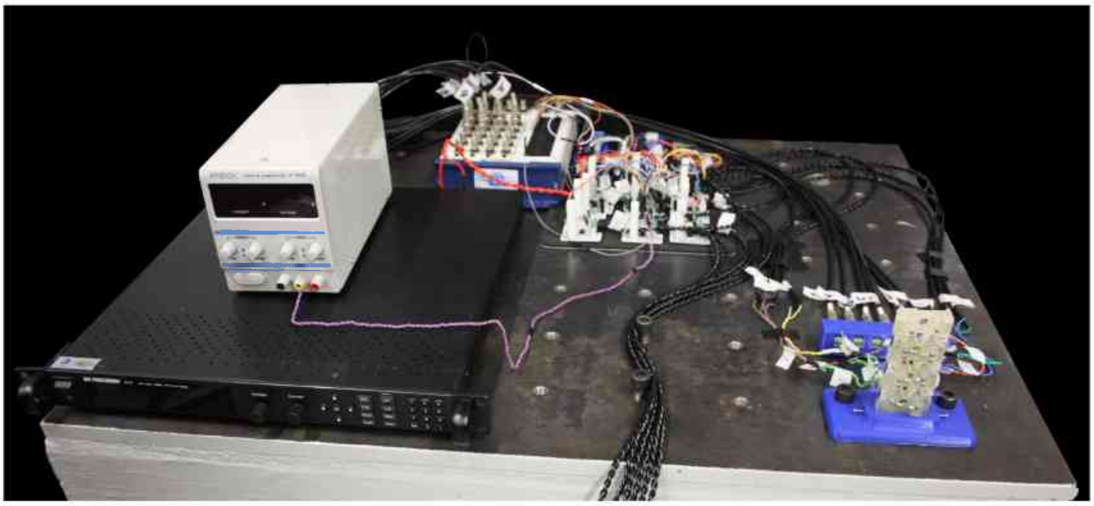

Figure 5.7 – An overview of the experimental setup

5.4 Morphing Beam Metastructure Experimental Results

Experiments have been performed with the morphing beam metastructure for evaluating its capabilities. The system was tested, as in the previous Chapter, with and without permanent magnets.

To guarantee the same conditions for the SMA wire actuators between these two configurations, permanent magnets were initially installed; wires were prestressed so multistable behavior could be observed for each unit cell; and experiments were conducted for this system condition. After tests were finished, permanent magnets were removed from the system, while taking care to not incur any loads on the SMA wires. Tests were then repeated with the system at its new configuration, without magnets.

An important point that deserves attention is related to the notation that has been used to distinguish between unit cells and SMA wires in the legends of the provided plots. Unit cell numbers increase from the metastructure free tip, to its fixed base. The SMA wires in each unit cell are referred to as "wire 1" and "wire 2", depending if they are oriented along the downward diagonal ($\diagdown$) or the upward diagonal ($\diagup$) directions, respectively, when looking at the metastructure from its front, and positioned in a vertical configuration, cf. Fig 5.3(b). Because of the adopted convention, wires 1 and 2 promote clockwise and counter-clockwise rotations of the system, respectively.

Figure 5.8 shows the currents that have been supplied to each of the actuators for testing the system with permanent magnets. It can be seen that the provided low and high current levels have been selected equal to 100 mA, and 1.25 A, respectively. Because of intrinsic differences related to components used in the current regulators, it can be seen that the currents vary by tiny amounts between SMA actuators. The actuation pattern that has been considered was selected in order to move the morphing metastructure between the maximum ±5° orientations considered for each unit cell. Tests were repeated a second time for each unit cell, as indicated by the dashed, black vertical line at 34 s. The pulse width considered for all actuators was set equal to 1.5 s.

Also, the time markings shown in this plot, and in all subsequent ones, are used as references for the start of an actuation command. As an example, consider the first pulse. It starts

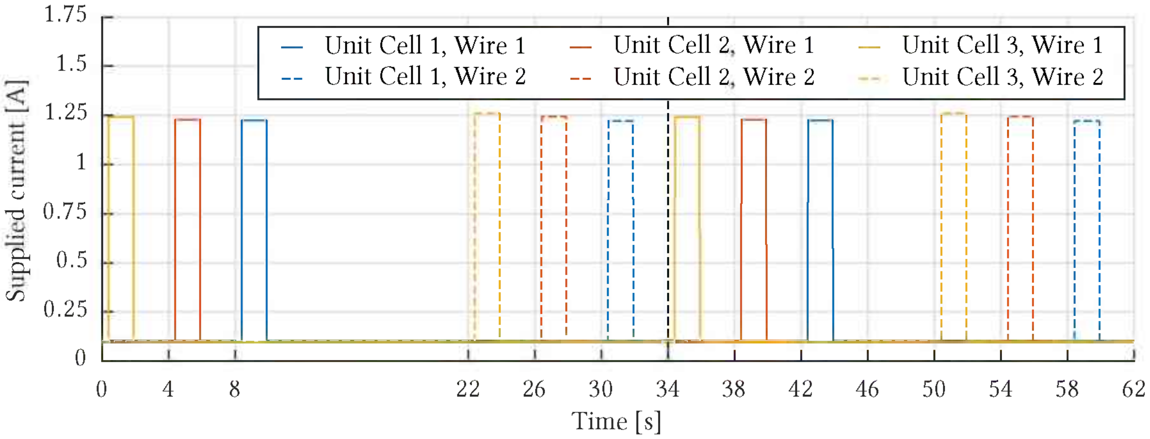

Figure 5.8 – Currents that have been supplied for SMA actuation of the morphing metastructure equipped with magnets

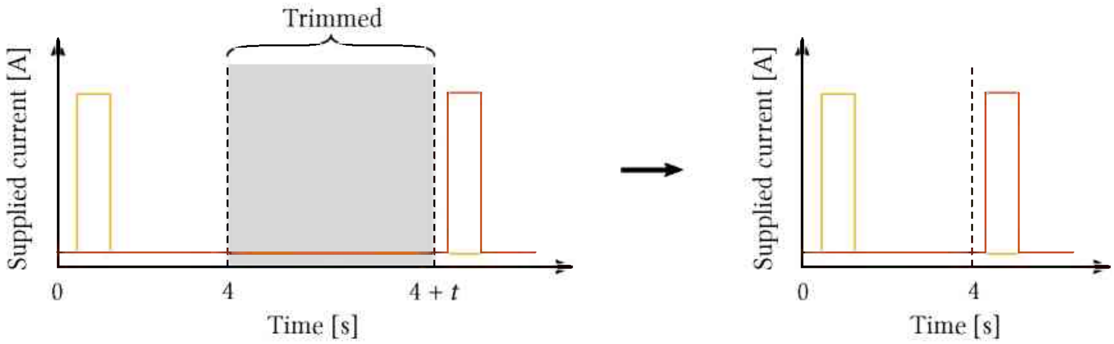

Figure 5.9 – Trimming procedure used to remove uneventful portions of experimental results during post-processing

near zero. The next pulse starts at 4 s. But this does not necessarily mean that only 4 s have been waited between these successive current pulses. In fact, sufficient time was given for the SMA wire that was actuated to cool back to ambient temperature. Figure 5.9 provides further clarifications in this respect; the value of t varied throughout distinct current pulses, but was kept in the order of 10 to 20 s for most cases. The illustrated procedure has been adopted so that plots concern themselves only to significant aspects of the results. Because of this, some small discontinuities might be seen at the specific time markings.

The angular displacements of the unit cells of the metastructure are provided in Figs. 5.10 and 5.11 for the actuation pattern given in Fig. 5.8. Video frames showing displaced configurations of the system are shown in Fig. 5.12. Relative rotations have been measured for each of the unit cells, and correspond to the amount of rotation the top of a particular cell has in relationship with its bottom part. The absolute rotation of a unit cell, on the other hand, measures the attitude of its top portion with respect to the horizontal direction. Counter-clockwise angles are considered positive and, initially, all unit cells were rotated towards this direction, as indicated by Fig. 5.10.

The figures in question allow one to see that permanent magnets were able to provide two new equilibrium configurations for unit cells 2 and 3, while unit cell 1 was not able to maintain itself in a clockwise rotation state which could be classified as stable during these tests.

Further inspection of the plots allows one to verify that the maximum rotations achieved by each of the unit cells are approximately equal to $\pm 4^\circ$, and thus smaller than the initial target of $\pm 5^\circ$. This fact can be attributed to deformations occurring in the compliant hinges, or to improper positioning of the permanent magnets. Since consistency can be observed across results related to all three cells, this last hypothesis seems unlikely to have occurred during prototype assembly. Therefore, one is confident that characteristics of the compliant hinge that has been used are responsible for the considered discrepancy. Simple modifications could be made in the design if greater angles were to be achieved.

Another feature in the responses that have been shown is related to the relatively fast transition times between the stable states, which are on the order of 0.6–0.8 s. These occur not only because of the relatively high current that is passed through the SMA wires, but also in account of the interactions between the permanent magnets.

After the previous verifications, focus is turned to the second set of experiments that were performed while the morphing metastructure was still equipped with permanent magnets. These were concerned with the stability of the neutral orientation configuration of the unit cells. An actuation pattern has been devised to try to make them achieve this condition. The currents that were supplied to the SMA actuators are shown in Fig. 5.13. The resulting relative rotations, absolute rotations and some displaced configurations are given in Figs. 5.14, 5.15 and 5.16, respectively.

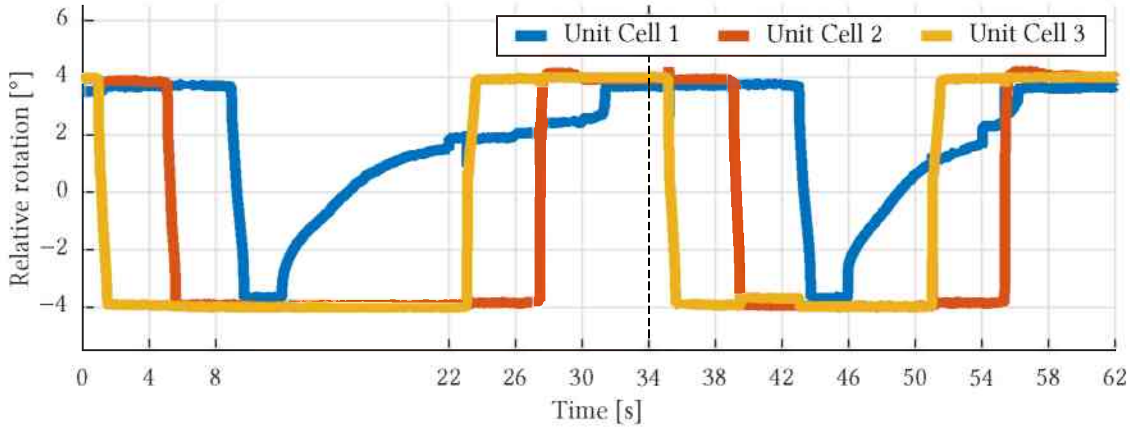

Figure 5.10 – Relative rotations of the unit cells equipped with permanent magnets, for the actuation currents given in Fig. 5.8

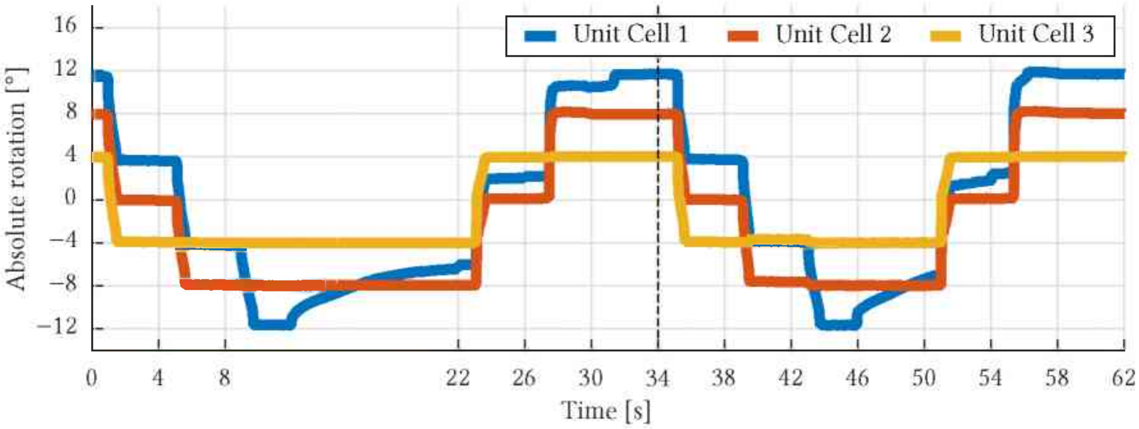

Figure 5.11 – Absolute rotations of the unit cells equipped with permanent magnets, for the actuation currents given in Fig. 5.8

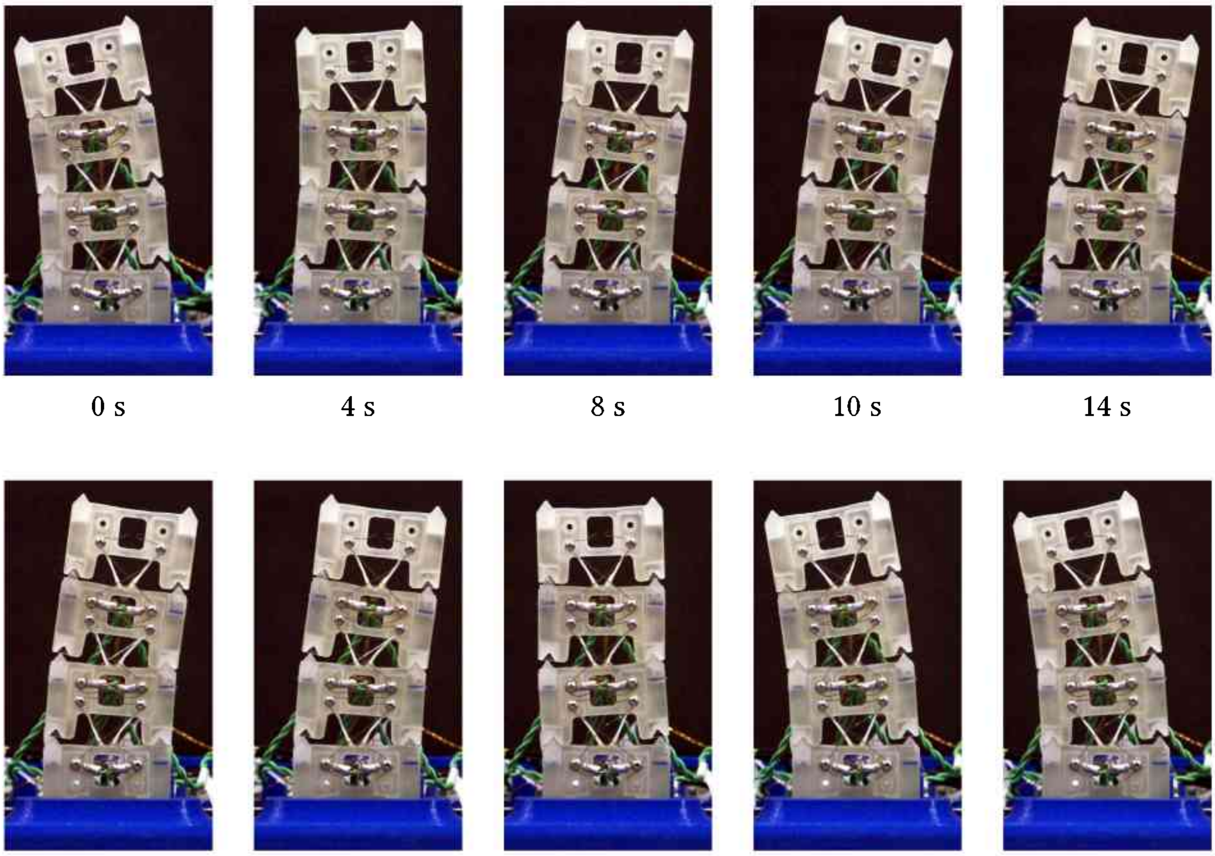

0 s 4 s 8 s 10 s 14 s

18 s 22 s 26 s 30 s 34 s

Figure 5.12 – Deformed configurations of the morphing metastructure when equipped with permanent magnets, for the actuation currents given in Fig. 5.8

It can be seen from Fig. 5.13 that attempts have been made for all three unit cells; the dashed vertical lines at 21 and 55 s timing marks distinguish between those. One tried to achieve a neutral orientation by starting from the two stable states that were observed to occur at $\pm 4°$.

Inspection of Figs. 5.14 and 5.15 immediately reveals that none of the unit cells possesses neutral orientation conditions which can be classified as stable. Tests performed with unit cells 1 and 3 showed best results, with these remaining in almost neutral conditions for approximately 4 s, for the attempts that started just after the 10 and 76 s timing marks.

The main reason that justify these results is the manual prestressing of the SMA wire actuators. The lack of a control methodology for applying prestress has led to tedious trial-and-error procedures during prototype assembly, due to its small size. Minute changes in wire orientation were induced by the way screws were used for securing them. Depending on the

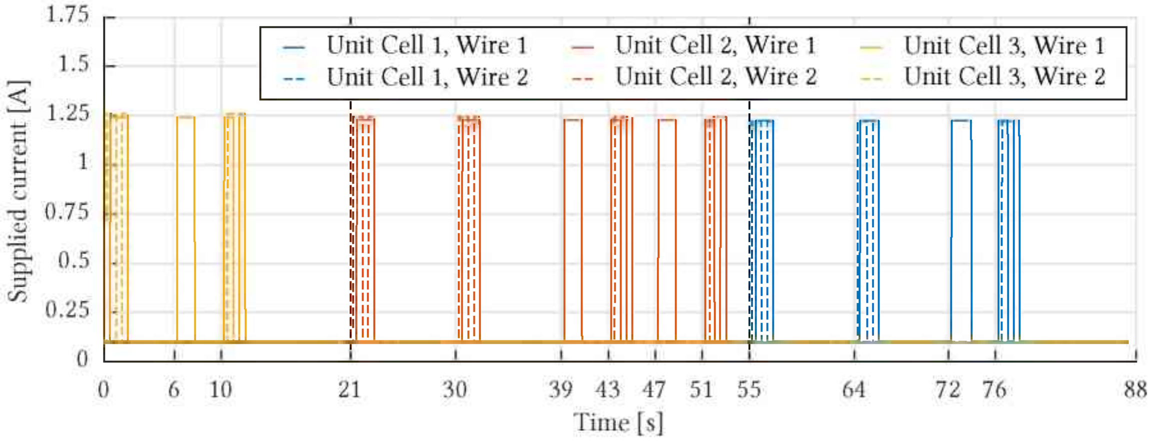

Figure 5.13 – Second set of currents that have been supplied for SMA actuation of the morphing metastructure equipped with magnets

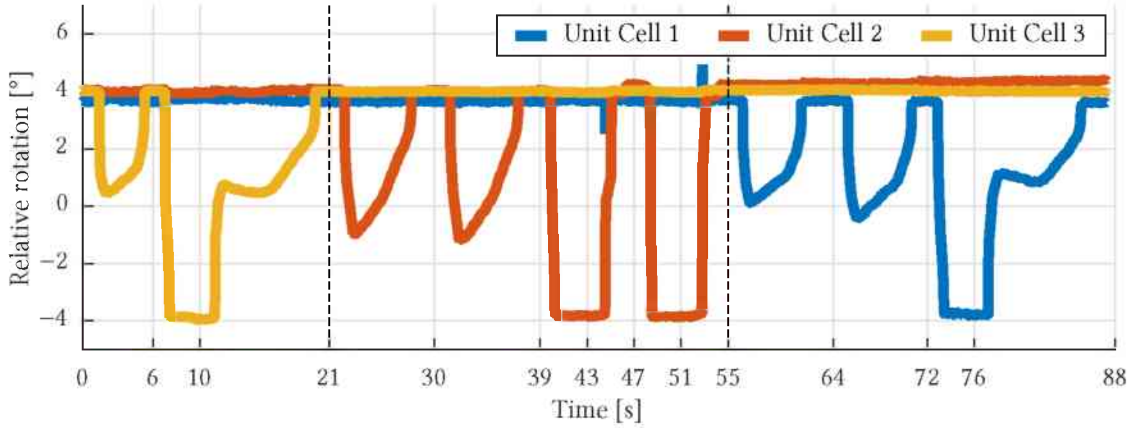

Figure 5.14 – Relative rotations of the unit cells equipped with permanent magnets, for the actuation currents given in Fig. 5.13

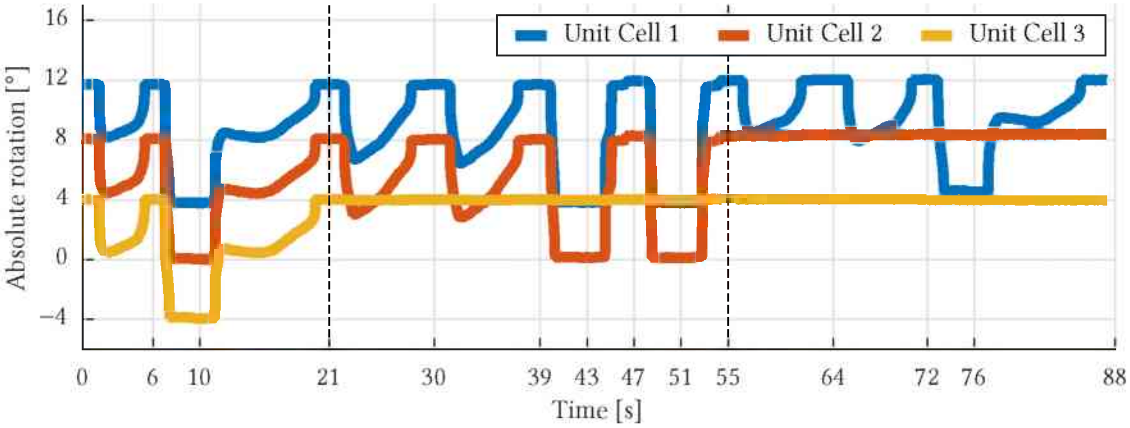

Figure 5.15 – Absolute rotations of the unit cells equipped with permanent magnets, for the actuation currents given in Fig. 5.13

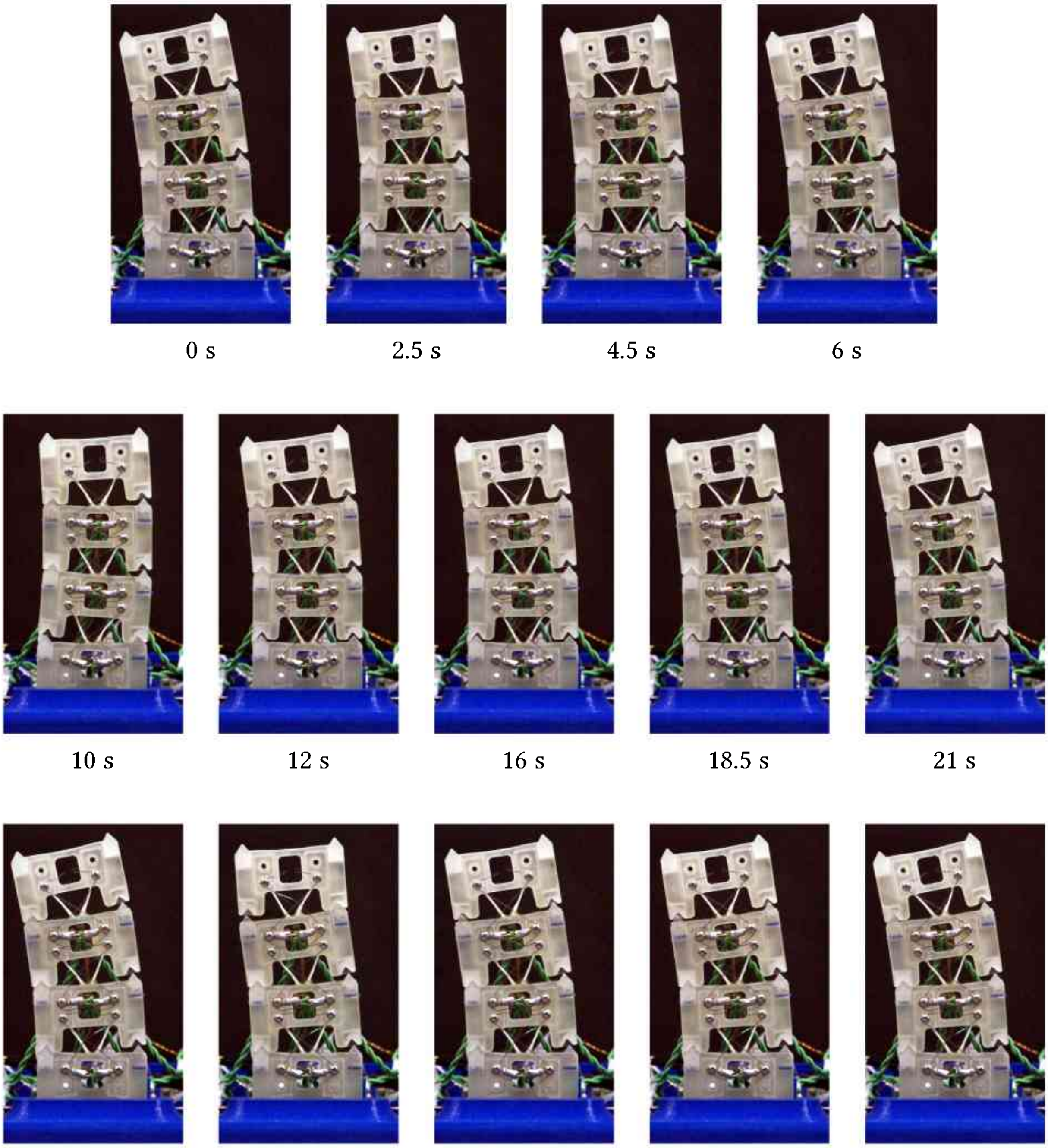

0 s 2.5 s 4.5 s 6 s

10 s 12 s 16 s 18.5 s 21 s

72 s 76 s 78.5 s 81.5 s 88 s

Figure 5.16 – Deformed configurations of the morphing metastructure when equipped with permanent magnets, for the actuation currents given in Fig. 5.13

side occupied by the SMA wire, the fastening of a screw could tighten or loosen it, thus leading to changes in the applied prestress. These aspects have been taken into account during hand assembly of the prototype. Much likely, a more precise methodology could be used, or the design could be changed, in order to avoid the troubles that have been encountered.

Another minor reasons for not achieving neutral rotation stable configurations are related to the actuation procedure that has been adopted, and to the vertical orientation used for testing. While improvements could be performed with regards to the first point, the lack of a proper stable configuration is not altered by it. As to the orientation assumed for testing, it demands a higher degree of stability from the metastructure, which, due to its low bending stiffness, resembles an inverted pendulum system in some sense.

A remarkable finding in the tests considered in Figs. 5.13 – 5.16 deals with the stability of unit cell 1. The use of a longer actuation current pulse, with duration of 1.7 s, has been able to make it sustain a stable configuration while deflected in the clockwise direction. This contradicts the behavior previously shown for the first set of actuation conditions, as per Fig. 5.10, for example.

The last results provided in this Chapter are related to the tests performed with the morphing metastructure after the removal of its permanent magnets. Figure 5.17 shows the currents that have been supplied to the SMA wire actuators for this condition. Figures 5.18, 5.19 and 5.20 display the relative rotations, absolute rotations, and some of the deformed configurations the system has experienced, respectively, for the actuation pattern of Fig. 5.17.

From Fig. 5.17, it is possible to see that three distinct sets of electrical currents have been provided to the SMA actuators. The first set consisted of pulses of 1.25 A with durations of 1.2 s. The second one still considered pulses with 1.25 A, but durations were increased to 1.9 s. The last set of pulsed currents had their amplitudes reduced to 1 A, while width durations were increased to 4 s.

SMA wire actuators were operated one at a time, just like it had been done for the experiments with the morphing metastructure when it had magnets attached to it. In the first round of actuation, the unit cells did not achieve full rotation capabilities, because a small pulse width had been considered. Similar conditions were adopted while testing the metastructure with attached magnets, and a clear distinction between the two cases can be point out in this regard: permanent magnets helped SMA actuation promote larger rotations in the system while very similar currents have been used in both cases.

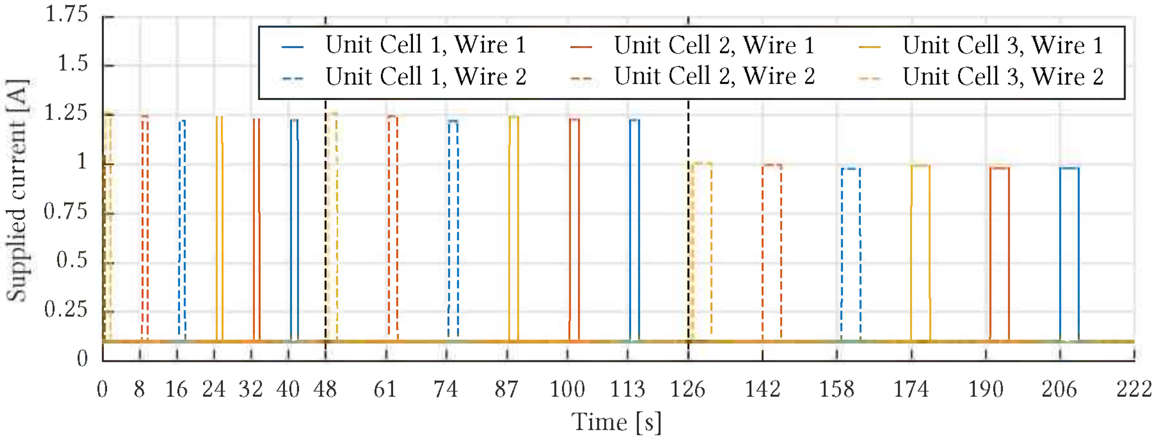

Figure 5.17 – Currents that have been supplied for SMA actuation of the morphing metastructure after removal of its permanent magnets

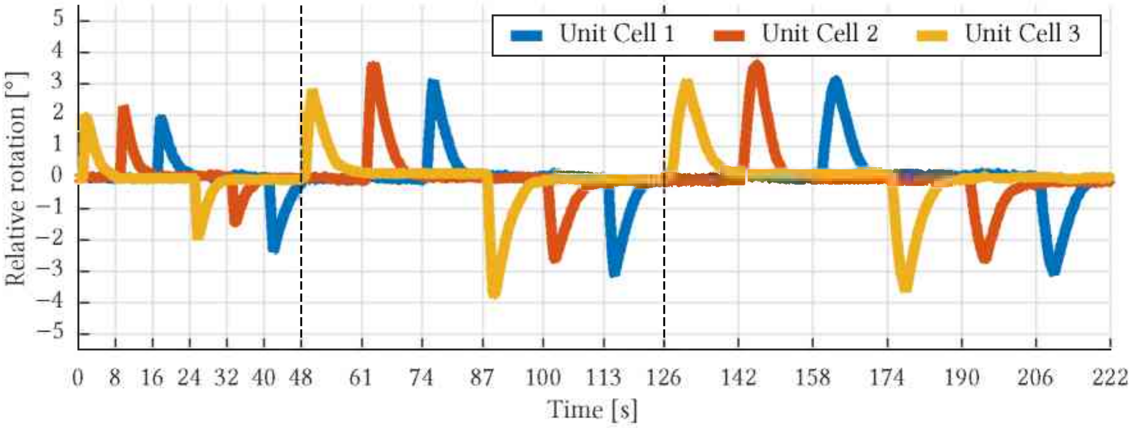

Figure 5.18 – Relative rotations of the unit cells with permanent magnets removed, for the actuation currents given in Fig. 5.17

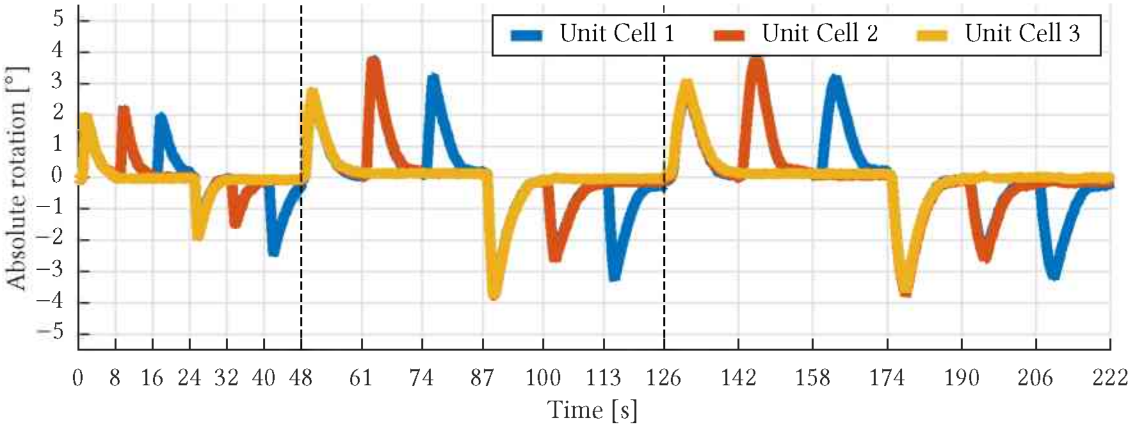

Figure 5.19 – Absolute rotations of the unit cells with permanent magnets removed, for the actuation currents given in Fig. 5.17

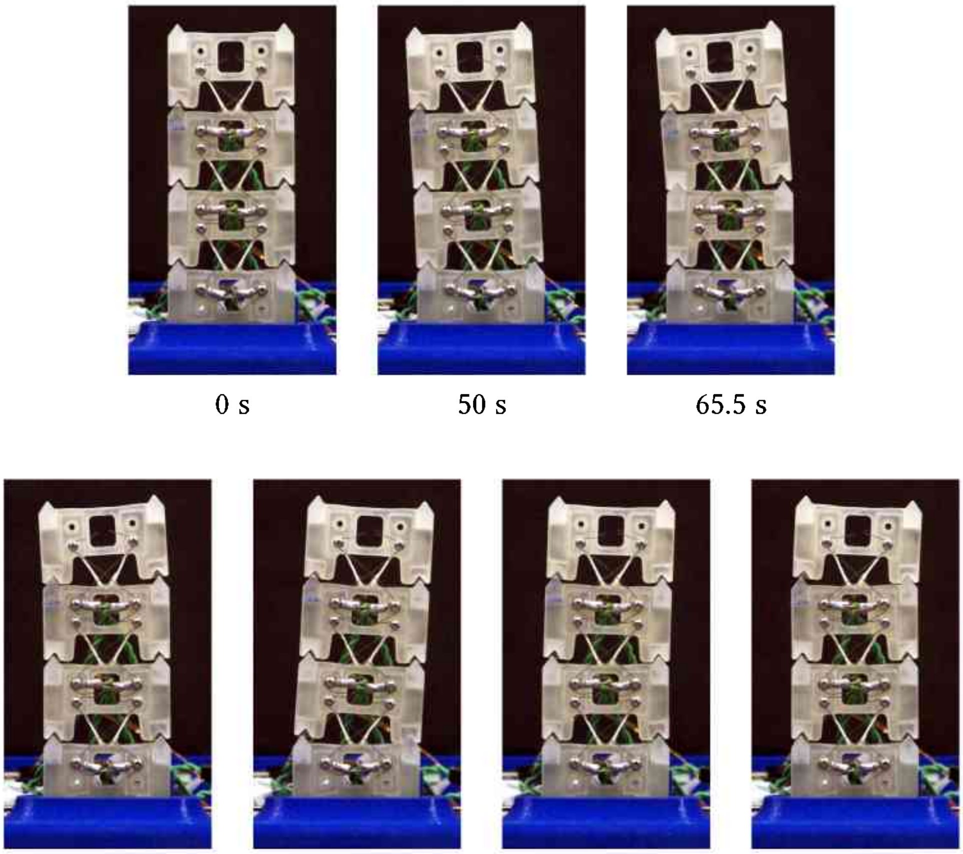

0 s 50 s 65.5 s

76 s 89.5 s 102.5 s 115 s

Figure 5.20 – Deformed configurations of the morphing metastructure with permanent magnets removed, for the actuation currents given in Fig. 5.17

The second round of SMA actuation had their durations increased, and as a result larger rotational displacements were achieved. These did not surpass the levels observed for the system with magnets, which once more confirms the point raised in the previous paragraph.

In the third round of actuation, similar maximum amplitudes were achieved by the unit cells, but during a longer period of time, in account of the smaller currents that were supplied.

The response times observed for the metastructure after the removal of permanent magnets are on the order of 1.2–1.3 s. This represents a significant increase over the timings related to the previous configuration, with permanent magnets attached to the metastructure, specially considering that much larger angular displacements were achieved in that case.

An interesting feature observed in Fig. 5.18 is related to the asymmetry between clockwise and counter-clockwise rotations for the same unit cells. This fact is much probably linked to different prestress being applied to the SMA wires of the same unit cell. Greater asymmetry is seen for unit cell 2, and helps to explain, in some degree, the poor results observed previously in Fig. 5.14 for this same cell.

The observed asymmetries also suggest that insufficient levels of prestress were applied to the SMA wires. This is indeed a possibility, because the wires were prestressed when permanent magnets were already installed on the metastructure. Verifications performed at that time, however, would be much likely pointless. This is because there is little room for predicting that the operation of the SMA wires would be hampered after the removal of permanent magnets from the system, while these were still in place. Also, as already explained, the levels of prestress have been kept the same for both system conditions to allow for a fair evaluation of the effects that are due to permanent magnets.

5.5 Summary and Conclusions

Along this Chapter, a description was provided for the proposed morphing unit cell. Justifications were also given for various choices that one has opted for in its design. Three distinct unit cell versions were dealt with during the studies that have been performed. Most promising versions were integrated into morphing beam metastructures. Prototypes were fabricated via 3D printing. This allowed easy manufacturing, but also has led to challenges in design that latter showed up during testing. Issues were also identified with the methodology used for prestressing SMA wires, which was aggravated by the setup considered for anchoring the actuators onto the metastructure.

The prototype was, nevertheless, tested in two distinct conditions: with and without permanent magnets. Experimental results have shown that permanent magnets were able to introduce two new stable configurations in the morphing unit cells, which were related to their maximum angular displacements. Stability originally observed for their neutral orientation was lost, however. Considering the unit cells to be bistable, instead of tristable as one worked for, the morphing beam metastructure is able to achieve $2^3 = 8$ distinct stable configurations, which require no external power to be maintained. The permanent magnets have also been shown to significantly reduce the response time of the system as a whole.

CHAPTER VI

SIX CELL MORPHING AIRFOIL

Chapters IV and V successively elaborated upon the simultaneous use of SMA actuators and permanent magnets for achieving multistable smart structures, while also tackling the poor energy efficiency related to SMAs. Throughout them, the analysis of a proof-of-concept beam system, and the test of a morphing beam metastructure have been considered. Now a morphing airfoil concept is investigated.

Section 6.1 details aspects related to the concept and the experimental setup that have been used for its test. Results and discussions follow in Section 6.2. A summary and conclusions are finally provided in Section 6.3.

6.1 Airfoil Description and Experimental Setup

The morphing airfoil considered in this Chapter has been based on the widely studied NACA 0012 airfoil. A chord of 400 mm was chosen for its design. In view of the selected profile, a maximum thickness of 48 mm results at 120 mm from the airfoil leading edge.

Integration of morphing capabilities into the design was made by considering the morphing unit cell proposed in the previous Chapter. The front part of the airfoil has been kept rigid, while its trailing edge portion was fitted with six unit cells. The prototype was fabricated via 3D printing, performed at the University of Michigan 3D Lab, as has been done for the beam metastruture previously. Because the length of the airfoil was larger than the maximum print

(a) Front part (b) Back part

Figure 6.1 – 3D printed parts of the morphing airfoil

size supported by the ProJet 3500 HD Max printer, the front and back parts of the prototype were split and printed separately; photographs of them can be seen in Fig. 6.1. The material used for printing was the VisiJet M3 Crystal plastic.

From Fig. 6.1(b), it can be seen that no more than six unit cells would have been able to be fitted along the back portion of the airfoil section, at least for the considered design. Because of the tapering that happens towards its trailing edge, all unit cells are slightly different from each other when it comes to the positioning of permanent magnets.

In this regard, NdFeB ones were adopted once more. Magnets with grade N42 were used for the four leftmost unit cells; while grade N52 ones, which are able to provide larger magnetic loads, were used for the two cells that are closer to the trailing edge of the airfoil. This has been done to counteract the reduction that occurs in the lever arms of the magnetic loads induced torques about the compliant joint center of rotation.

Apart from these distinctions related to permanent magnets, the characteristics of the unit cells used in the morphing airfoil are equal to those given previously in Chapter V. With respect to the airfoil section width, its value has been set equal to 10 mm.

Figure 6.2 shows the morphing airfoil after it was prepared for testing. Assembly involved the installation of 8 metal nuts and 8 screws for securing 4 SMA wire actuators, as well

Figure 6.2 – Morphing airfoil after assembly, ready for testing

as 4 permanent magnets for each unit cell. As there were six ones in the concept, a total of 48 nuts, 48 screws, 24 SMA wires, and 24 permanent magnets were integrated to the airfoil section.

As has been done for the morphing metastructure of Chapter V, Loctite® Super Glue was used to secure both the nuts and the permanent magnets to the 3D printed components. A ring terminal, to which electrical copper wire was soldered to, was secured with each SMA wire, when of its clamping with a screw, to facilitate electrical connections. Opposing SMA wires on the unit cell were also connected in series. Application of prestress to the wire actuators was done manually, while trying to maintain consistency between different unit cells.

The experimental setup used for running tests is identical to the one described in the previous Chapter, cf. Section 5.3. The same current regulators considered at that time were used to drive the SMA actuators in the morphing airfoil. A B&K Precision® power supply model 9115 was used to meet current requirements. The NI® USB-6259 BNC DAQ was once again used for controlling the current sources through the setup involving electromechanical relays. The experiment was recorded with a Sony® NEX-VG10 Handycam, which allowed for the determination of displacements during post-processing of results. The open source Tracker software was used for this purpose. Figure 6.3 shows an overview of the experimental setup ready for testing.

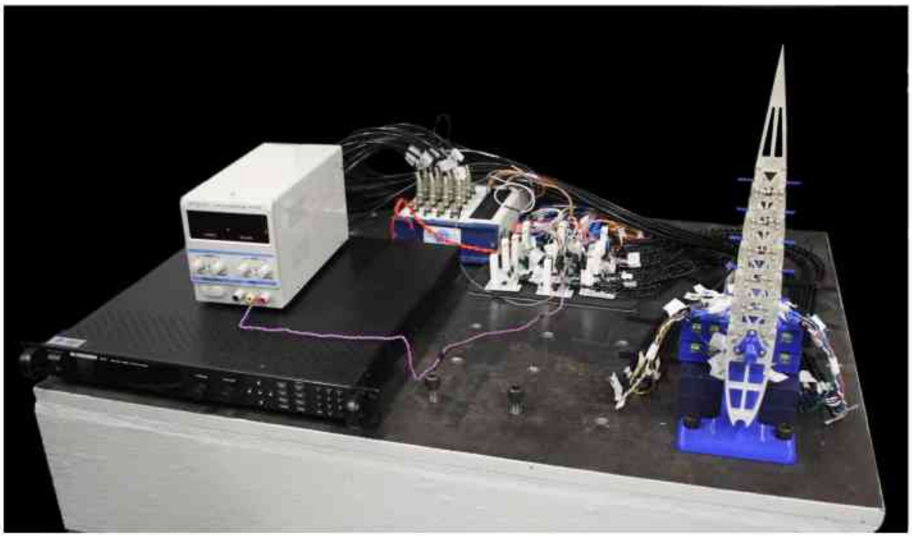

Figure 6.3 – Experimental setup used for testing the morphing airfoil

6.2 Experimental Results and Discussion

The morphing airfoil prototype has been tested, like the previous systems, with and without permanent magnets. One aimed to demonstrate and evaluate its behavior.

One remarks that the results presented next are covered by the same comments given in the previous Chapter. For instance, timing marks are related to the start of a new actuation condition, cf. Fig. 5.9 on p. 94. In addition, unit cells of the airfoil are numbered from one to six stating from its trailing edge, towards its front. SMA wire actuators are labeled as "wire 1" and "wire 2" for each unit cell depending if they are oriented along the downward diagonal (╲) or the upward diagonal (╱) directions, respectively, when the airfoil is look from the front, in an upright vertical position, such as the one shown in Fig. 6.3.

The first tests were performed with the morphing airfoil when it had permanent magnets attached to it. Figures 6.4, 6.5, 6.6 and 6.7 display, respectively, the currents adopted for actuation, the relative orientations of the unit cells during the tests, their absolute rotations, and deformed configurations of the system.

As can be seen from Fig. 6.4, SMA wires were actuated one at a time, starting from the one closest to the airfoil trailing edge. In the sequence, the next unit cell towards the front of the airfoil was actuated, and the procedure was repeated successively until the cell that is the closest to the leading edge was reached. Afterwards, the same procedure was repeated, actuating the unit cells starting at the trailing edge, and advancing towards the leading edge, but for obtaining rotations in the opposite direction. Current pulses with amplitudes of 1.25 A and duration of 1.5 s were considered for all wires. A second round of actuation has also been performed in the same way, to evaluate consistency.

Relative orientations provided in Fig. 6.5 show that most of the cells were able to achieve ±4° of angular displacement, and maintain these positions without the need of additional SMA actuation. Unit cell 1, which is the closest to the airfoil trailing edge, had rotations limited to roughly ±2.5°, and consists of the only exception. One is confident that this behavior is a result of the permanent magnets adopted in this cell being of grade N52, and more close to each other,

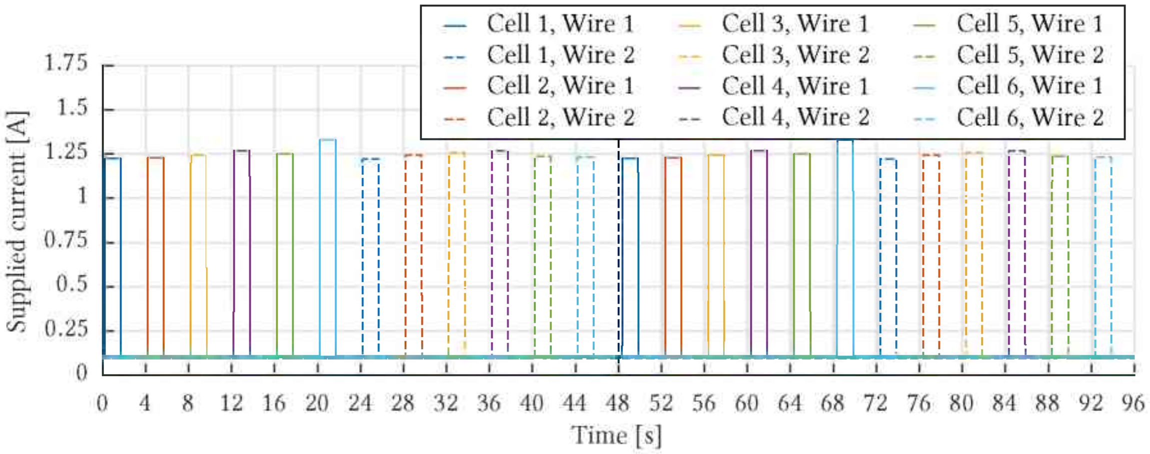

Figure 6.4 – Currents that have been supplied for SMA actuation of the morphing airfoil equipped with magnets

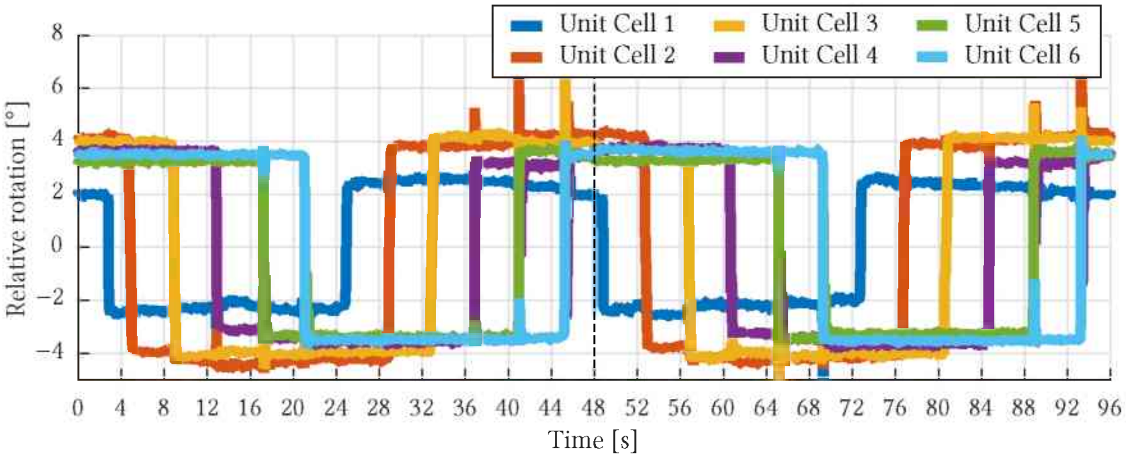

Figure 6.5 – Relative rotations of the unit cells equipped with permanent magnets, for the actuation currents given in Fig. 6.4

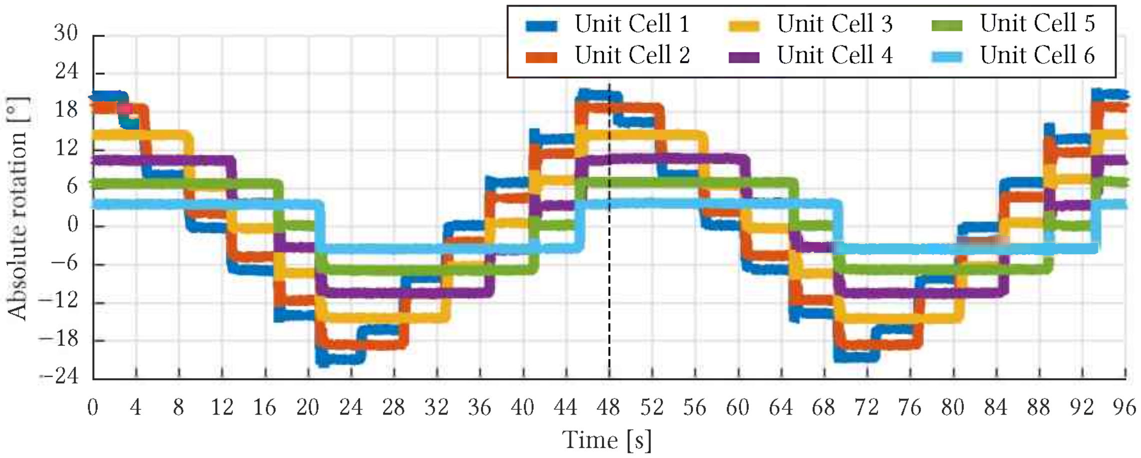

Figure 6.6 – Absolute rotations of the unit cells equipped with permanent magnets, for the actuation currents given in Fig. 6.4

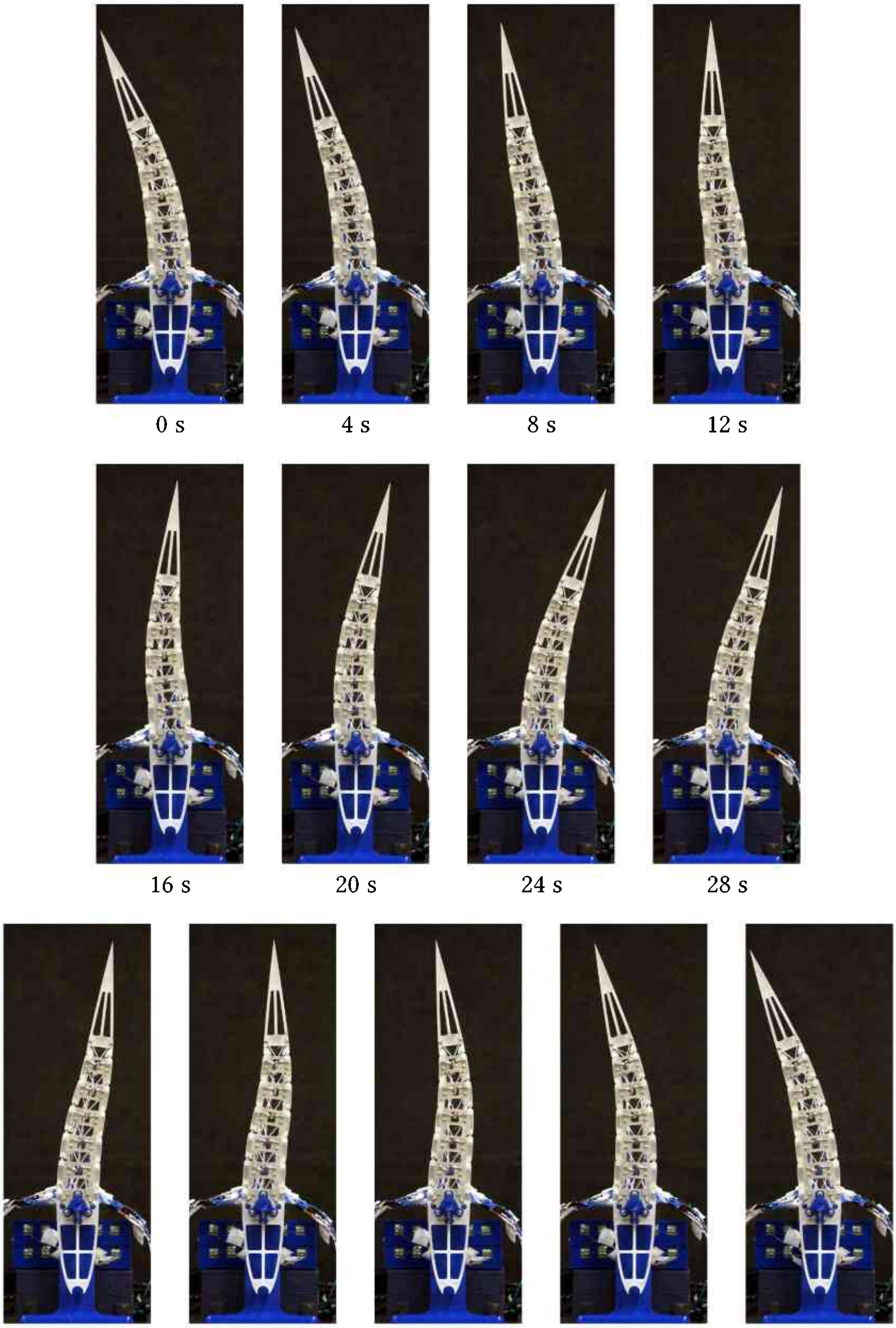

0 s 4 s 8 s 12 s

16 s 20 s 24 s 28 s

32 s 36 s 40 s 44 s 48 s

Figure 6.7 – Deformed configurations of the morphing airfoil when equipped with permanent magnets, for the actuation currents given in Fig. 6.4

as well; as a side effect of this, larger loads might have been applied to the compliant hinge, and thus constraint its motion.

The absolute rotations seen in Fig. 6.6 allows one to verify that the maximum rotations for the last portion of the airfoil were on the order of ±20°. While the unit cells were designed aiming maximum rotations of ±5°, as discussed in Chapter V, results are considered to be good, and on par with other ones reported in the literature (BARBARINO et al., 2009; BARBARINO et al., 2011a).

Results from both Figs. 6.5 and 6.6 point to some vibrations that occurred during morphing, as indicated by rotation overshoots during actuation. These are owed to the snap through events the morphing airfoil experiences when contact between two magnets happens, or is ended. Vibrations fade away pretty quickly, and because of this further investigations in this regard have not been performed.

The deformed shapes shown in Fig. 6.7 illustrate that relatively large, smooth morphing configurations were achieved. Also, one remembers that every shape that is shown is stable, and do not require any amount of external energy to be maintained.

In the previous Chapter it has been shown that the unit cells of the beam metastructure were not capable of stable configurations characterized by rotations close to zero. Because of this, tests have not been performed with the morphing airfoil prototype to try achieving such type of configurations.

After experiments with the morphing airfoil equipped with permanent magnets were completed, these were removed. Extreme caution has been taken when performing this task to avoid changing the prestress in the SMA wire actuators.

Figures 6.8 through 6.11 provide results concerning the initial tests performed with the airfoil after removal of the permanent magnets.

From Fig. 6.8 it can be seen that the experiment at hand aimed for the actuation of the SMA wires one at a time, as has been performed for the previous case. Once again, the current pulses that were applied had 1.25 A during an interval of 1.5 s.

The relative rotations provided in Fig. 6.9 show that the performance of the six units cells were very similar between themselves. Maximum rotations of approximately ±4° were

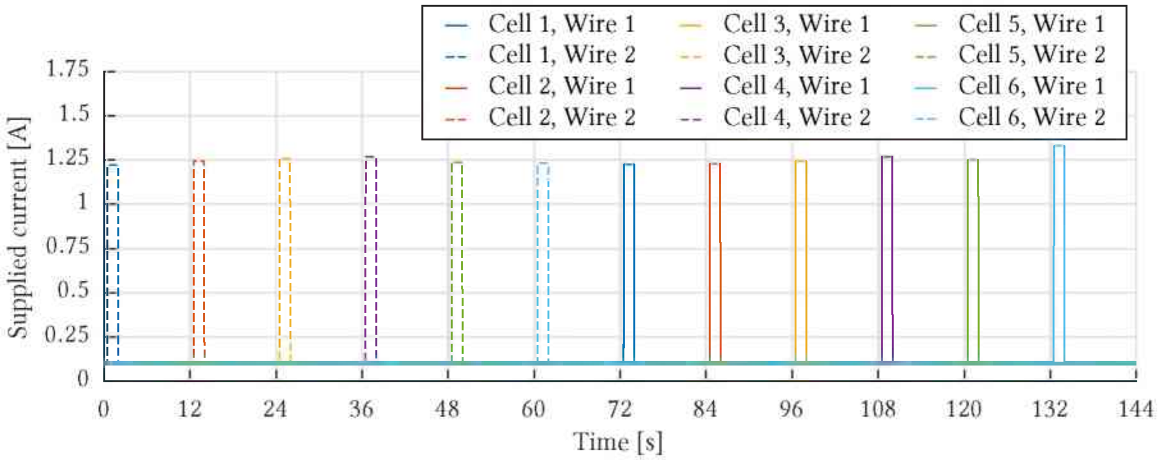

Figure 6.8 – Currents that have been supplied for SMA actuation of the morphing airfoil after removal of its permanent magnets

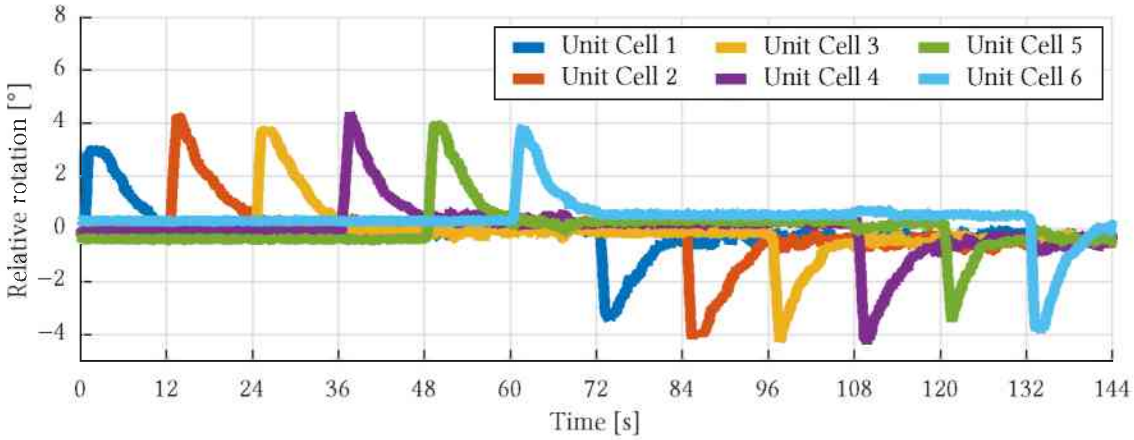

Figure 6.9 – Relative rotations of the unit cells with permanent magnets removed, for the actuation currents given in Fig. 6.8

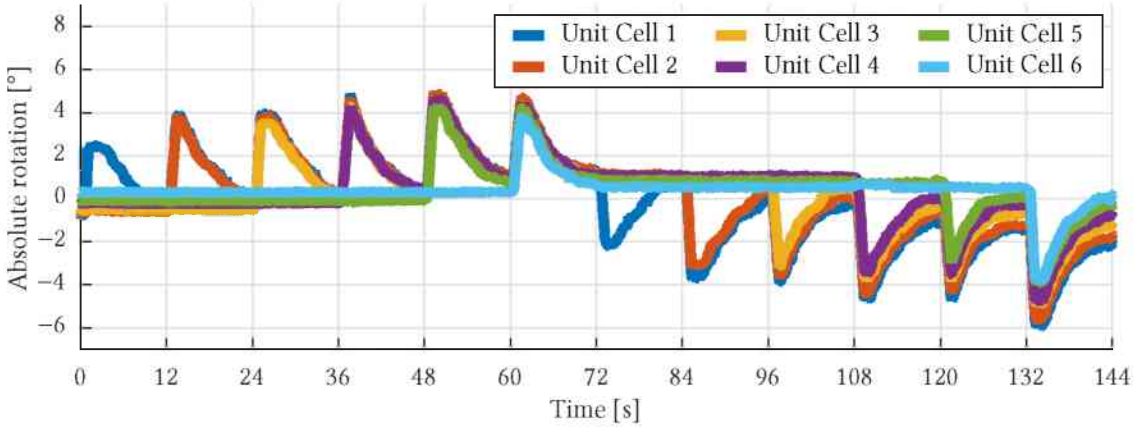

Figure 6.10 – Absolute rotations of the unit cells with permanent magnets removed, for the actuation currents given in Fig. 6.8

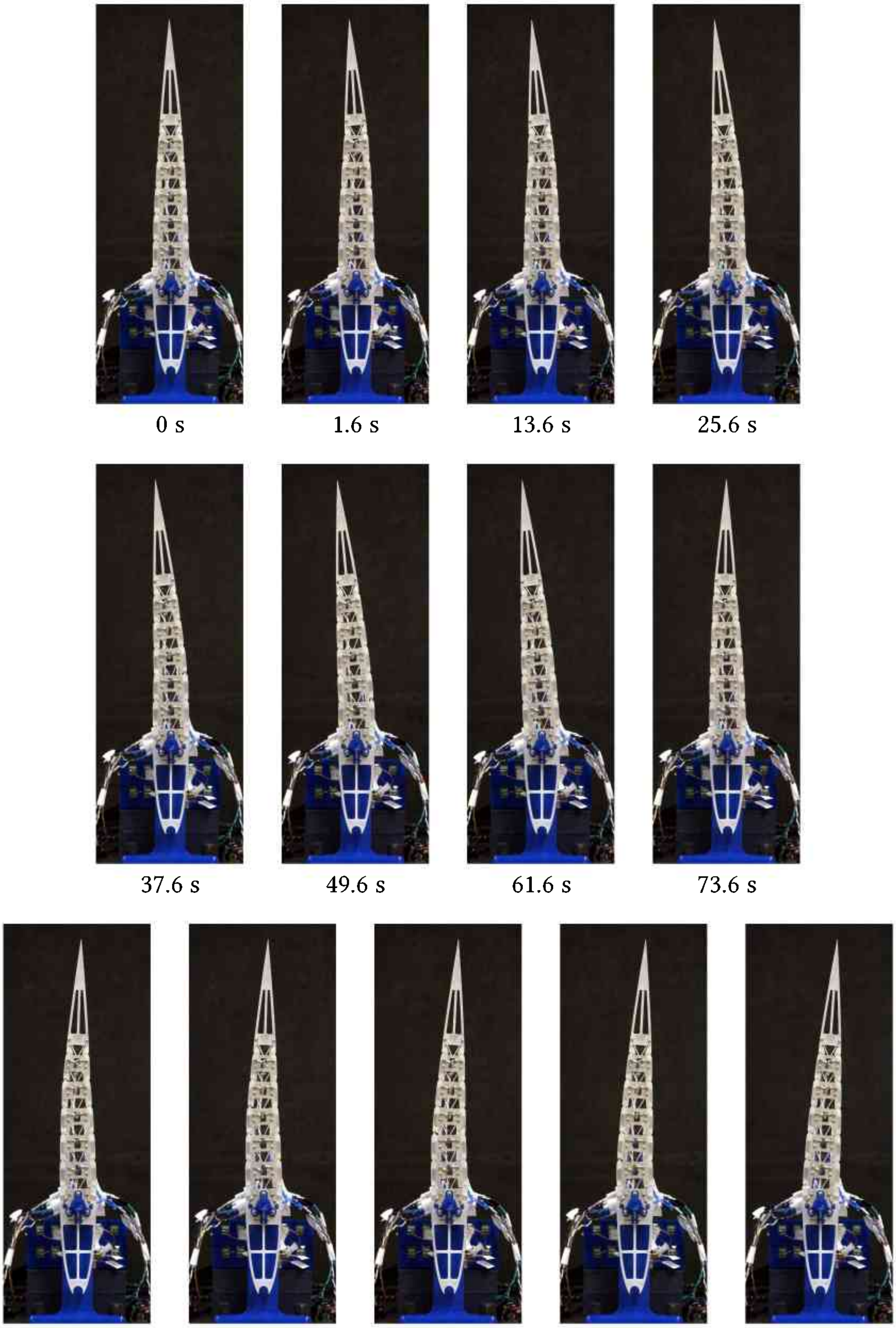

0 s 1.6 s 13.6 s 25.6 s

37.6 s 49.6 s 61.6 s 73.6 s

85.6 s 97.6 s 109.6 s 121.6 s 133.6 s

Figure 6.11 – Deformed configurations of the morphing airfoil with permanent magnets removed, for the actuation currents given in Fig. 6.8

achieved, which are on par with the ones presented previously in Fig. 6.5. With respect to the case in which permanent magnets were installed in the morphing airfoil, though, it can be seen that it is not able to sustain deformed configurations without relying on external power input. Figure 6.9 also indicate a good symmetry for the behavior of each unit cell, since the same level of rotation has been achieved in both clockwise and counter-clockwise directions.

Absolute rotations shown in Fig. 6.10 simply reflect the fact that unit cells that are closer to the morphing airfoil trailing edge have their orientations changed by the actuation of those near the front of the airfoil. Apart from that, the same inferences given previously for Fig. 6.9 apply.

Figure 6.11 finally shows the maximum deformed configurations achieved by the morphing airfoil when each unit cell was actuated independently. These are not particularly exciting simply due to the lack of considerable shape change.

Following these tests, the morphing airfoil was subjected to a second set of actuation currents, which can be seen in Fig. 6.12. The resulting rotations can be seen in Fig. 6.13 and 6.14, while deformed shapes of the morphing airfoil are provided in Fig. 6.15.

Figure 6.12 shows that the current pulses applied to the SMA wires had once again 1.25 A for 1.5 s. This time, however, several distinct patterns were considered for actuation. Following the sequence shown in the figure, one has heated:

- the wire 1 of all unit cells;
- the wire 2 of all unit cells;
- the wire 1 of unit cells 1 to 3;
- the wire 2 of unit cells 1 to 3;
- the wire 1 of unit cells 4 to 6;
- the wire 2 of unit cells 4 to 6;
- the wire 1 of unit cells 4 to 6 and the wire 2 of unit cells 1 to 3; and
- the wire 1 of unit cells 1 to 3 and the wire 2 of unit cells 4 to 6.

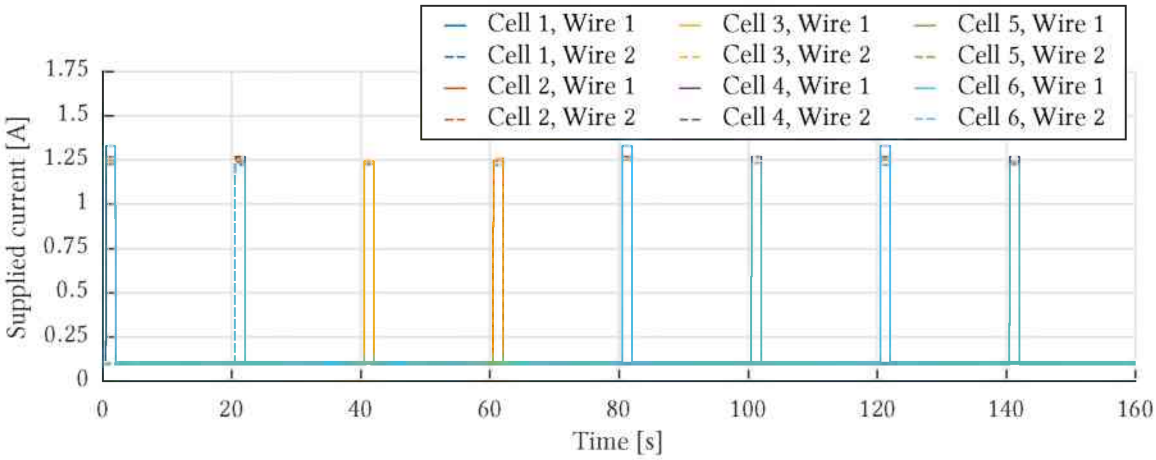

Figure 6.12 – Second set of currents that have been supplied for SMA actuation of the morphing airfoil after removal of its permanent magnets

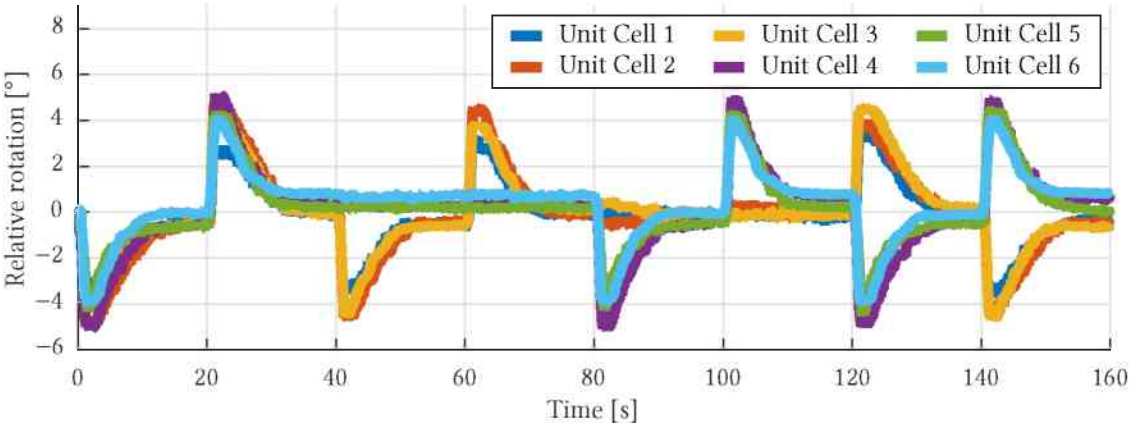

Figure 6.13 – Relative rotations of the unit cells with permanent magnets removed, for the actuation currents given in Fig. 6.12

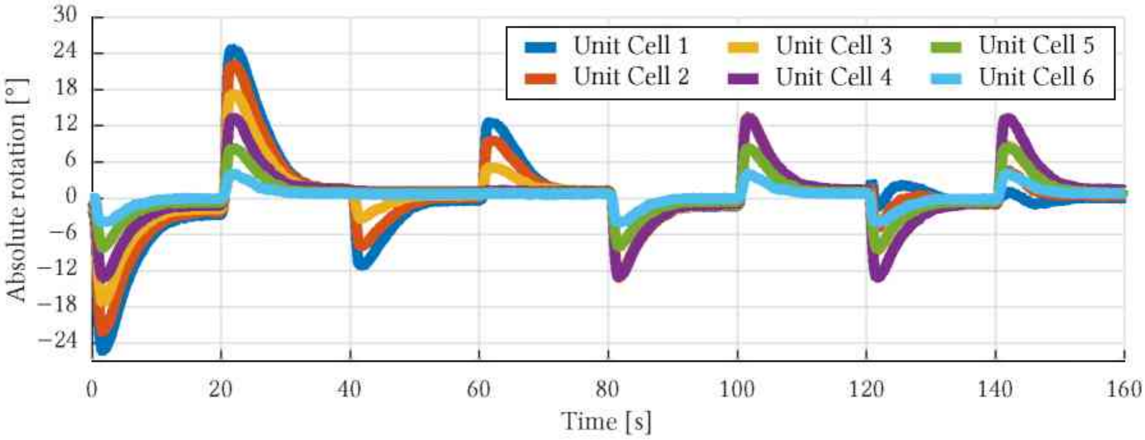

Figure 6.14 – Absolute rotations of the unit cells with permanent magnets removed, for the actuation currents given in Fig. 6.12

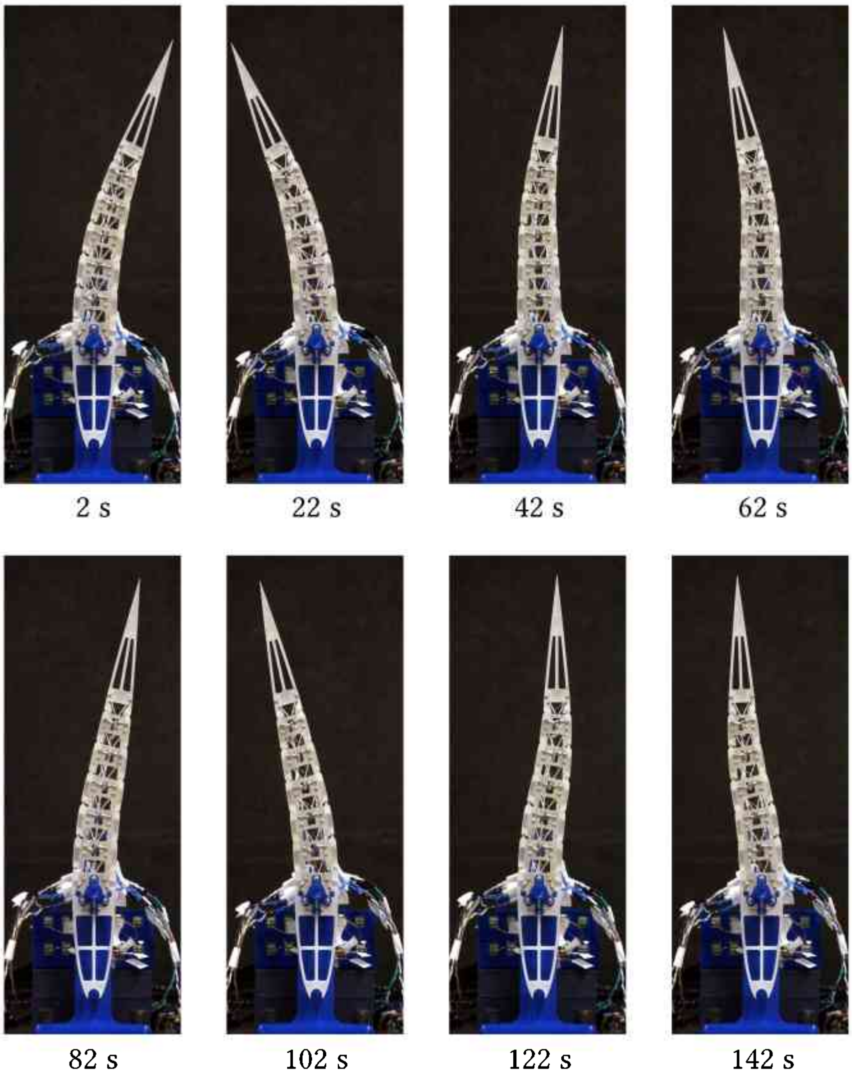

Figure 6.15 – Deformed configurations of the morphing airfoil with permanent magnets removed, for the actuation currents given in Fig. 6.12

Relative and absolute rotations are given in Figs. 6.13 and 6.14, respectively. They show that the maximum rotations achieved by the trailing edge of the airfoil are approximately ±25°, which are related to the first two actuation patterns just given. These values are marginally larger than the ones observed for the condition in which the morphing airfoil was equipped with permanent magnets, cf. Fig. 6.6. This might be due to the loads inflicted by the permanent magnets on the compliant hinges on that occasion, which might have constrained the maximum achievable rotations by the unit cells, due to the associated deformation. Nevertheless, the shapes achieved by the morphing airfoil after removal of permanent magnets are not stable, which is a significant trade-off for the minor increase observed for the maximum rotation at the trailing edge.

Aesthetic deformed shapes associated with the actuation patterns at analysis can be seen in Fig. 6.15. These, together with the previous ones observed for the case in which permanent magnets were installed onto the morphing airfoil, cf. Fig. 6.7, highlight one of the major benefits of the metastructure layout adopted for morphing, which is the possibility of localized rotation control.

6.3 Summary and Conclusions

Along this Chapter, a morphing airfoil metastructure concept has been considered. Its geometric layout has been based on the use of the unit cell considered in Chapter V. A prototype of the morphing airfoil was produced via 3D printing. It was assembled and prepared for testing. Experimental results were obtained for two conditions, in which the airfoil had, and had not, permanent magnets attached to it.

One more time it has been shown that permanent magnets were able to provide new stable configurations for the unit cell. When these are adopted in the morphing airfoil, in a number of six, and considering them to be bistable, a total of $2^6 = 64$ distinct configurations could be achieved. As has been reported in the previous Chapter, permanent magnets also improve the response times of SMA actuation, at least during its heating phase.

Because the proposed morphing airfoil possess distributed actuation, localized control of its camber line is made possible, which is ideal for the considered application for the range of possibilities it introduces. While multistability limits to some degree the number of alternative configurations the morphing airfoil is able to achieve, it allows for deformed states to be maintained at the expense of no external power. In the case SMA wires are used for actuation, as has been considered, this becomes advantageous as one is able to tackle their low energetic efficiency by avoiding their continuous operation.

CHAPTER VII

CONCLUSIONS AND PERSPECTIVES

Along this Thesis, one has considered the simultaneous use of SMA actuators and permanent magnets for achieving multistable smart structures, while aiming for morphing applications.

A literature review has been presented, which showed that multistable structures are attractive for morphing applications, as well as for remedying the low energetic efficiency of SMA actuators. Furthermore, it has been seen that the simultaneous use of SMA actuators and permanent magnets has received little to none interest by the scientific community. Another point that was briefly addressed in the review had to do with the so-called metastructures, which consist of periodic geometrical arrangements that benefit from possessing an array of integrated features.

A mathematical modeling strategy was then outlined for enabling the simulation of magneto-thermo-mechanical systems. One have addressed a geometrically nonlinear beam finite element formulation; a constitutive model for SMA wires; the modeling of the interaction between rectangular-parallelepiped-shaped permanent magnets with arbitrary orientations; and an algorithm for node-to-element contact. Coupling procedures for the modeling strategies were also discussed, and a solution strategy was also presented.

The first investigations performed dealt with a proof-of-concept beam system, to which antagonistic SMA actuators and permanent magnets were attached. Quasi-static experiments were conducted, which allowed one to show the integration of permanent magnets in SMA actuated systems could lead to additional stable equilibrium configurations. Numerical results were computed and showed good agreement with experimental data.

Following this, the design of a morphing unit cell that incorporates the simultaneous use of SMA wires and permanent magnets was considered. It was initially used in the construction of a morphing beam metastructure, composed of three unit cells. Experiments were performed, and one verified that the unit cells composing the metastructure were able to achieve new stable equilibrium states. Since three were used in the metastructure, and the unit cells turned out to be bistable, a total of eight distinct stable equilibrium states could have been achieved. Reasons for the loss of stability for the neutral orientation state of the unit cells were also discussed, and included the prototype being 3D printed, and the lack of control while prestressing SMA wires.

A morphing airfoil concept, made out of the same unit cells adopted previously, was finally considered. Prototypes were 3D printed and assembled. Tests showed that the airfoil camber could be properly morphed. A total of 64 distinct stable configurations should be possible for the morphing airfoil section when it is equipped with permanent magnets. The distributed actuation provided by the metastructure layout also allowed for localized control, which consists of a desirable feature in morphing applications.

Based on these premises, it can be seen that the objectives of the Thesis initially proposed in Chapter I have been successfully achieved. Furthermore, conclusions can be drawn regarding contributions that have been made with respect to multi-physics modeling, and the progress of morphing technologies. For instance, for the first time a multistable morphing airfoil section based on the simultaneous use of SMA wire actuators and permanent magnets has been studied. Also, a general modeling framework has been proposed, which has been demonstrated to successfully capture relevant features of the type of systems considered in the Thesis.

With respect to the airfoil prototype that has been manufactured, it is not more than that, i.e. just a prototype. To be used in an actual application, design should be made more carefully, aiming for higher stiffness. Also, multistability achieved for the tested prototypes does not seem robust enough, as reasonably low loads appear to make them move between distinct equilibrium states. In this sense, optimization could be used for increasing the degree of stability associated with the relevant configurations of the proposed unit cell, provided that an accurate model can be established for it. It might be wise to consider, for instance, the so-called V-model, adopted in systems engineering and verification, for model validation during sequential stages of the design.

In short, considering that the prototypes that have been manufactured were not optimized, and have been devised only as proofs of concept, it seems that the main idea proposed in the Thesis needs to be further explored, so it can be adopted in applications.

Given the previous statements, results that have been obtained appear encouraging. As mentioned, designs proposed in Chapters V and VI, as well as the mathematical model of Chapter III, can all be improved. Therefore, the following aspects can be suggested for future research:

a) The considered unit cell resulted relatively flexible, which could harm its ability in sustaining loads. Optimization has not been considered during design, and could help in the search for better unit cell configurations in this regard.

b) The layout adopted for the permanent magnets also did not favor stable states with neutral orientation, i.e. with null rotation. In this respect, other topologies could have been considered, in which magnets are positioned differently. To provide solid means for securing new stable configurations, mechanical locking mechanisms could also be implemented in the design.

c) The adopted constitutive model for SMA wire actuators was not able to perform good predictions during material phase transformation. Smoothing techniques and other modeling strategies could be considered for better representation and predictions. Performing proper characterization of the SMA material could also help clarify if identified parameters are truly representative of its behavior.

d) The study has been limited to a single morphing airfoil because of time constraints. More elaborated investigations could have been performed if a morphing wing was considered. Wind tunnel tests could be used to evaluate questions related to aerodynamic benefits, for example. Fluid-structure interaction modeling and aeroelastic phenomena arising due to morphing owed flexibility could also be considered.

e) The proposed morphing metastructures have all been one dimensional, and actuated by SMA actuators. Studies might be performed in trying to expand the concept of morphing metastructures to higher dimensionality, or by considering different actuator types. Simplified strategies for modeling metastructures, that consider reduced order modeling for its unit cells, is also a theme that can be of interest.

f) Dynamic characteristics related to the multistable behavior provided by permanent magnets in SMA actuated smart structures also make for an interesting subject that can be investigated.

BIBLIOGRAPHIC REFERENCES

AKOUN, G.; YONNET, J. P. 3D analytical calculation of the forces exerted between two cuboidal magnets. **IEEE Transactions on Magnetics**, v. 20, n. 5, pp. 1962–1964, 1984.

ALLAG, H.; YONNET, J.-P. 3-D analytical calculation of the torque and force exerted between two cuboidal magnets. **IEEE Transactions on Magnetics**, v. 45, n. 10, pp. 3969–3972, 2009.

ANSYS. **ANSYS® academic research, release 17.0, help system, mechanical APDL theory reference**. Chapter 14, Section 11. [S.l.: s.n.], 2015.

ARRIETA, A. F.; KUDER, I. K.; RIST, M.; WAEBER, T.; ERMANNI, P. Passive load alleviation aerofoil concept with variable stiffness multi-stable composites. **Composite Structures**, v. 116, pp. 235–242, 2014.

ARRIETA, A.; WAGG, D.; NEILD, S. Dynamic snap-through for morphing of bi-stable composite plates. **Journal of Intelligent Material Systems and Structures**, v. 22, n. 2, pp. 103–112, 2011.

AURICCHIO, F.; BONETTI, E.; SCALET, G.; UBERTINI, F. Theoretical and numerical modeling of shape memory alloys accounting for multiple phase transformations and martensite reorientation. **International Journal of Plasticity**, v. 59, pp. 30–54, 2014.

AVVARI, P. V.; TANG, L.; YANG, Y.; SOH, C. K. Enhancement of piezoelectric energy harvesting with multi-stable nonlinear vibrations. In: Active and Passive Smart Structures and Integrated Systems 2013. Mar. 10–14, 2013, San Diego, California, USA. **Proceedings of SPIE Vol. 8688**, 86882H-1–86882H-12.

BARBARINO, S.; FLORES, E. I. S.; AJAJ, R. M.; DAYYANI, I.; FRISWELL, M. I. A review on shape memory alloys with applications to morphing aircraft. **Smart Materials and Structures**, v. 23, n. 6, pp. 063001-1–063001-19, 2014.

BARBARINO, S.; PECORA, R.; LECCE, L.; CONCILIO, A.; AMEDURI, S.; CALVI, E. A novel SMA-based concept for airfoil structural morphing. **Journal of Materials Engineering and Performance**, v. 18, pp. 696–705, 2009.

BARBARINO, S.; PECORA, R.; LECCE, L.; CONCILIO, A.; AMEDURI, S.; DE ROSA, L. Airfoil structural morphing based on SMA actuator series: numerical and experimental studies. **Journal of Intelligent Material Systems and Structures**, v. 22, n. 10, pp. 987–1004, 2011a.

BARBARINO, S.; BILGEN, O.; AJAJ, R. M.; FRISWELL, M. I.; INMAN, D. J. A review of morphing aircraft. **Journal of Intelligent Material Systems and Structures**, v. 22, n. 9, pp. 823–877, 2011b.

BARTH, J.; KOHL, M. A bistable magnetically enhanced shape memory microactuator with high blocking forces. **Physics Procedia**, v. 10, pp. 189–196, 2010.

BARTH, J.; KREVET, B.; KOHL, M. A bistable shape memory microswitch with high energy density. **Smart Materials and Structures**, v. 19, n. 9, pp. 094004-1–094004-8, 2010.

BARTH, J.; MEGNIN, C.; KOHL, M. A bistable shape memory alloy microvalve with magnetostatic latches. **Journal of Microelectromechanical Systems**, v. 21, n. 1, pp. 76–84, 2012.

BATHE, K. J.; BOUZINOV, P. A. On the constraint function method for contact problems. **Computers & Structures**, v. 64, n. 5–6, pp. 1069–1085, 1997.

BROWN, D. **Tracker video analysis and modeling tool**. Version 4.97. Available at: < `http://physlets.org/tracker/` >. Accessed on: May 19, 2017.

CAZÓN, A.; MORER, P.; MATEY, L. PolyJet technology for product prototyping: tensile strength and surface roughness properties. **Proceedings of the Institution of Mechanical Engineers, Part B: Journal of Engineering Manufacture**, v. 228, n. 12, pp. 1664–1675, 2014.

CHANG, B.-C.; SHAW, J. A.; IADICOLA, M. A. Thermodynamics of shape memory alloy wire: modeling, experiments, and application. **Continuum Mechanics and Thermodynamics**, v. 18, n. 1, pp. 83–118, 2006.

CHEN, Y. Y.; HU, G. K.; HUANG, G. L. An adaptive metamaterial beam with hybrid shunting circuits for extremely broadband control of flexural waves. **Smart Materials and Structures**, v. 25, n. 10, pp. 105036-1–105036-13, 2016.

CISSE, C.; ZAKI, W.; ZINEB, T. B. A review of constitutive models and modeling techniques for shape memory alloys. **International Journal of Plasticity**, v. 76, pp. 244–284, 2016a.

CISSE, C.; ZAKI, W.; ZINEB, T. B. A review of modeling techniques for advanced effects in shape memory alloy behavior. **Smart Materials and Structures**, v. 25, n. 10, pp. 103001-1–103001-36, 2016b.

DAYNES, S.; POTTER, K. D.; WEAVER, P. M. Bistable prestressed buckled laminates. **Composites Science and Technology**, v. 68, n. 15, pp. 3431–3437, 2008.

DAYYANI, I.; SHAW, A. D.; SAAVEDRA FLORES, E. I.; FRISWELL, M. I. The mechanics of composite corrugated structures: a review with applications in morphing aircraft. **Composite Structures**, v. 133, pp. 358–380, 2015.

DIACONU, C. G.; WEAVER, P. M.; MATTIONI, F. Concepts for morphing airfoil sections using bi-stable laminated composite structures. **Thin-Walled Structures**, v. 46, n. 6, pp. 689–701, 2008.

DYNALLOY. **Technical characteristics of Flexinol® actuator wires**. Available at: < `http://www.dynalloy.com/pdfs/TCF1140.pdf` >. Accessed on: July 31, 2017.

EMAM, S. A.; INMAN, D. J. A review on bistable composite laminates for morphing and energy harvesting. **Applied Mechanics Reviews**, v. 67, n. 6, pp. 060803-1–060803-15, 2015.

ETEROVIC, A. L.; BATHE, K. J. On the treatment of inequality constraints arising from contact conditions in finite element analysis. **Computers & Structures**, v. 40, n. 2, pp. 203–209, 1991.

FRISWELL, M. I. Morphing aircraft: an improbable dream? In: SMASIS 2014. Sept. 8–10, 2014, Newport, Rhode Island, USA. **Proceedings of the ASME 2014 Conference on Smart Materials, Adaptive Structures and Intelligent Systems**, pp. 7754-1–7754-7.

FU, S.; DING, G.; WANG, H.; YANG, Z.; FENG, J. Design and fabrication of a magnetic bi-stable electromagnetic MEMS relay. **Microelectronics Journal**, v. 38, n. 4, pp. 556–563, 2007.

GALL, Y. L.; BOLZMACHER, C. Design and characterization of a multi-stable magnetic shape memory alloy hybrid actuator. **Microsystem Technologies**, v. 20, n. 4, pp. 533–543, 2014.

GAUTHIER, J.-Y.; HUBERT, A.; ABADIE, J.; LEXCELLENT, C.; CHAILLET, N. Multistable actuator based on magnetic shape memory alloy. In: ACTUATOR'2006. June 14–16, 2006, Bremen, Germany. **Proceedings of the 10th International Conference on New Actuators, ACTUATOR'06**, pp. 787–790.

GOMEZ, J. C.; GARCIA, E. Morphing unmanned aerial vehicles. **Smart Materials and Structures**, v. 20, n. 10, pp. 103001-1–103001-16, 2011.

HAGHPANAH, B.; SALARI-SHARIF, L.; POURRAJAB, P.; HOPKINS, J.; VALDEVIT, L. Multistable shape-reconfigurable architected materials. **Advanced Materials**, v. 28, n. 36, pp. 7915–7920, 2016.

HARNE, R. L.; WANG, K. W. A review of the recent research on vibration energy harvesting via bistable systems. **Smart Materials and Structures**, v. 22, n. 2, pp. 023001-1–023001-12, 2013.

HARTL, D. J.; LAGOUDAS, D. C. Aerospace applications of shape memory alloys. **Proceedings of the Institution of Mechanical Engineers, Part G: Journal of Aerospace Engineering**, v. 221, n. 4, pp. 535–552, 2007.

HOBECK, J. D.; INMAN, D. J. Simultaneous passive broadband vibration suppression and energy harvesting with multifunctional metastructures. In: A Tribute Conference Honoring Daniel Inman. Mar. 25–29, 2017, Portland, Oregon, USA. **Proceedings of SPIE Vol. 10172**, 101720K-1–101720K-15.

HU, N.; BURGUEÑO, R. Buckling-induced smart applications: recent advances and trends. **Smart Materials and Structures**, v. 24, n. 6, pp. 063001-1–063001-20, 2015.

HUFENBACH, W.; GUDE, M.; KROLL, L. Design of multistable composites for application in adaptive structures. **Composites Science and Technology**, v. 62, n. 16, pp. 2201–2207, 2002.

ISHII, H.; TING, K.-L. SMA actuated compliant bistable mechanisms. **Mechatronics**, v. 14, n. 4, pp. 421–437, 2004.

JANSSEN, J. L. G.; PAULIDES, J. J. H.; LOMONOVA, E.; BÖLÖNI, F.; TOUNZI, A.; PIRIOU, F. Analytical calculation of interaction force between orthogonally magnetized permanent magnets. **Sensor Letters**, v. 7, n. 3, pp. 442–445, 2009.

JHA, A. K.; KUDVA, J. N. Morphing aircraft concepts, classifications, and challenges. In: Smart Structures and Materials 2004: Industrial and Commercial Applications of Smart Structures Technologies. Mar. 14–18, 2004, San Diego, California, USA. **Proceedings of SPIE Vol. 5388**, pp. 213–224.

KARAMI, M. A.; VAROTO, P. S.; INMAN, D. J. Experimental study of the nonlinear hybrid energy harvesting system. In: 29th IMAC, A Conference on Structural Dynamics, 2011. Jan. 31–Feb. 3, 2011, Jacksonville, Florida, USA. **Modal Analysis Topics, Volume 3. Conference Proceedings of the Society for Experimental Mechanics Series**, pp. 461–478.

KHEIRIKHAH, M. M.; RABIEE, S.; EDALAT, M. E. A review of shape memory alloy actuators in robotics. In: Robot Soccer World Cup. June 19–25, 2010, Singapore, Singapore. **RoboCup 2010: Robot Soccer World Cup XIV**, pp. 206–217.

KIM, H. A.; BETTS, D. N.; SALO, A. I. T.; BOWEN, C. R. Shape memory alloy-piezoelectric active structures for reversible actuation of bistable composites. **AIAA Journal**, v. 48, n. 6, pp. 1265–1268, 2010.

KIM, P.; SEOK, J. A multi-stable energy harvester: dynamic modeling and bifurcation analysis. **Journal of Sound and Vibration**, v. 333, n. 21, pp. 5525–5547, 2014.

KING, C.; BEAMAN, J. J.; SREENIVASAN, S. V.; CAMPBELL, M. Multistable equilibrium system design methodology and demonstration. **Journal of Mechanical Design**, v. 126, n. 6, pp. 1036–1046, 2005.

K&JMAGNETICS. **K&J Magnetics, Inc. Your online source for incredibly powerful neodymium magnets**. Available at: < `http://www.kjmagnetics.com` >. Accessed on: May 19, 2017.

LACHENAL, X.; DAYNES, S.; WEAVER, P. M. Review of morphing concepts and materials for wind turbine blade applications. **Wind Energy**, v. 16, n. 2, pp. 283–307, 2013.

LAGOUDAS, D. C. **Shape memory alloys: modeling and engineering applications**. [S.l.]: Springer, 2008. 446 pp.

LAGOUDAS, D. C.; HARTL, D.; CHEMISKY, Y.; MACHADO, L.; POPOV, P. Constitutive model for the numerical analysis of phase transformation in polycrystalline shape memory alloys. **International Journal of Plasticity**, v. 32–33, pp. 155–183, 2012.

LAN, C. C.; FAN, C. H. Investigation on pretensioned shape memory alloy actuators for force and displacement self-sensing. In: 2010 IEEE/RSJ International Conference on Intelligent Robots and Systems. Oct. 18–22, 2010a, Taipei, Taiwan. **2010 IEEE/RSJ International Conference on Intelligent Robots and Systems**, pp. 3043–3048.

LAN, C.-C.; FAN, C.-H. An accurate self-sensing method for the control of shape memory alloy actuated flexures. **Sensors and Actuators A: Physical**, v. 163, n. 1, pp. 323–332, 2010b.

LEE, A. J.; MOOSAVIAN, A.; INMAN, D. J. A piezoelectrically generated bistable laminate for morphing. **Materials Letters**, v. 190, pp. 123–126, 2017.

LEE, J.-G.; RYU, J.; LEE, H.; CHO, M. Saddle-shaped, bistable morphing panel with shape memory alloy spring actuator. **Smart Materials and Structures**, v. 23, n. 7, pp. 074013-1–074013-9, 2014.

LEI, Y.-M.; YAO, X.-F. Experimental study of bistable behaviors of deployable composite structure. **Journal of Reinforced Plastics and Composites**, v. 29, n. 6, pp. 865–873, 2010.

LEO, D. J. **Engineering analysis of smart material systems**. [S.l.]: John Wiley & Sons, 2007. 576 pp.

MA, N.; SONG, G.; LEE, H. J. Position control of SMA actuators with internal electrical resistance feedback. In: Smart Structures and Materials 2003: Modeling, Signal Processing, and Control. Mar. 2, 2003, San Diego, California, USA. **Proceedings of SPIE Vol. 5049**, pp. 46–55.

MACHADO, L. G.; SAVI, M. A. Medical applications of shape memory alloys. **Brazilian Journal of Medical and Biological Research**, v. 36, n. 6, pp. 683–691, 2003.

MACHEKPOSHTI, D. F.; TOLOU, N.; HERDER, J. L. A review on compliant joints and rigid-body constant velocity universal joints toward the design of compliant homokinetic couplings. **Journal of Mechanical Design**, v. 137, n. 3, pp. 032301-1–032301-12, 2015.

MATTIONI, F.; WEAVER, P. M.; FRISWELL, M. I. Multistable composite plates with piecewise variation of lay-up in the planform. **International Journal of Solids and Structures**, v. 46, n. 1, pp. 151–164, 2009.

MATTIONI, F.; WEAVER, P. M.; POTTER, K. D.; FRISWELL, M. I. Analysis of thermally induced multistable composites. **International Journal of Solids and Structures**, v. 45, n. 2, pp. 657–675, 2008a.

MATTIONI, F.; WEAVER, P. M.; POTTER, K. D.; FRISWELL, M. I. The application of thermally induced multistable composites to morphing aircraft structures. In: Industrial and Commercial Applications of Smart Structures Technologies 2008. Mar. 9–13, 2008b, San Diego, California, USA. **Proceedings of SPIE Vol. 6930**, pp. 693012-1–693012-11.

MCGOWAN, A.-M. R. Technologies for adaptive and morphing airplanes: history, challenges & lessons learned. In: IX Simposium Internacional de Física. Feb. 16, 2007, Monterrey, Nuevo León, Mexico. **Proceedings of IX Simposium Internacional de Física**. Keynote Lecture.

MOHD JANI, J.; LEARY, M.; SUBIC, A.; GIBSON, M. A. A review of shape memory alloy research, applications and opportunities. **Materials & Design**, v. 56, pp. 1078–1113, 2014.

MONTALVO, C. J. **Meta aircraft flight dynamics and controls**. 2014. 139 pp. Ph.D. Thesis – School of Aerospace Engineering, Georgia Institute of Technology, Atlanta, Georgia, USA.

MORGAN, N. B. Medical shape memory alloy applications — the market and its products. **Materials Science and Engineering: A**, v. 378, n. 1, pp. 16–23, 2004.

NESPOLI, A.; BESSEGHINI, S.; PITTACCIO, S.; VILLA, E.; VISCUSO, S. The high potential of shape memory alloys in developing miniature mechanical devices: a review on shape memory alloy mini-actuators. **Sensors and Actuators A: Physical**, v. 158, n. 1, pp. 149–160, 2010.

PAIVA, A.; SAVI, M. A. An overview of constitutive models for shape memory alloys. **Mathematical Problems in Engineering**, v. 2006. Article ID 56876, pp. 1–30, 2006.

PELLEGRINI, S. P.; TOLOU, N.; SCHENK, M.; HERDER, J. L. Bistable vibration energy harvesters: a review. **Journal of Intelligent Material Systems and Structures**, v. 24, n. 11, pp. 1303–1312, 2013.

PETRINI, L.; MIGLIAVACCA, F. Biomedical applications of shape memory alloys. **Journal of Metallurgy**, v. 2011, pp. 501483-1–501483-15, 2011.

PHAM, H.-T.; WANG, D.-A. A quadristable compliant mechanism with a bistable structure embedded in a surrounding beam structure. **Sensors and Actuators A: Physical**, v. 167, n. 2, pp. 438–448, 2011.

PORTELA, P.; CAMANHO, P.; WEAVER, P.; BOND, I. Analysis of morphing, multi stable structures actuated by piezoelectric patches. **Computers & Structures**, v. 86, n. 3, pp. 347–356, 2008.

QIU, J.; LANG, J. H.; SLOCUM, A. H. A curved-beam bistable mechanism. **Journal of Microelectromechanical Systems**, v. 13, n. 2, pp. 137–146, 2004.

QIU, J.; LANG, J. H.; SLOCUM, A. H.; WEBER, A. C. A bulk-micromachined bistable relay with U-shaped thermal actuators. **Journal of Microelectromechanical Systems**, v. 14, n. 5, pp. 1099–1109, 2005.

REICHL, K.; INMAN, D. J. Longitudinal metastructure bar with an active vibration absorber (conference presentation). In: Active and Passive Smart Structures and Integrated Systems 2017. Mar. 25–29, 2017, Portland, Oregon, USA. **Proceedings of SPIE Vol. 10164**, 101640Z–101640Z-1.

REISSNER, E. On one-dimensional finite-strain beam theory: the plane problem. **Zeitschrift für angewandte Mathematik und Physik**, v. 23, n. 5, pp. 795–804, 1972.

RODRIGUEZ, A. Morphing aircraft technology survey. In: 45th AIAA Aerospace Sciences Meeting and Exhibit. Jan. 8–11, 2007, Reno, Nevada, USA. **Proceedings of the 45th AIAA Aerospace Sciences Meeting and Exhibit**, pp. 1–16.

SANDERS, B.; CROWE, R.; GARCIA, E. Defense Advanced Research Projects Agency – smart materials and structures demonstration program overview. **Journal of Intelligent Material Systems and Structures**, v. 15, n. 4, pp. 227–233, 2004.

SCHIEPP, T.; SCHNETZLER, R.; RICCARDI, L.; LAUFENBERG, M. Energy-efficient multistable valve driven by magnetic shape memory alloys. In: 10th International Fluid Power Conference. Mar. 8–10, 2016, Dresden, Germany. **Proceedings of the 10th International Fluid Power Conference**, pp. 491–502.

SCHULTZ, M.; HYER, M. A morphing concept based on unsymmetric composite laminates and piezoceramic MFC actuators. In: 45th AIAA/ASME/ASCE/AHS/ASC Structures, Structural Dynamics & Materials Conference. Apr. 19–22, 2004, Palm Springs, California, USA. **Proceedings of the 45th AIAA/ASME/ASCE/AHS/ASC Structures, Structural Dynamics & Materials Conference**.

SHAW, J. A.; CHURCHILL, C. B. A reduced-order thermomechanical model and analytical solution for uniaxial shape memory alloy wire actuators. **Smart Materials and Structures**, v. 18, n. 6, pp. 065001-1–065001-21, 2009.

SOFLA, A.; ELZEY, D.; WADLEY, H. Two-way antagonistic shape actuation based on the one-way shape memory effect. **Journal of Intelligent Material Systems and Structures**, v. 19, n. 9, pp. 1017–1027, 2008.

SUN, J.; GUAN, Q.; LIU, Y.; LENG, J. Morphing aircraft based on smart materials and structures: a state-of-the-art review. **Journal of Intelligent Material Systems and Structures**, v. 27, n. 17, pp. 2289–2312, 2016.

THILL, C.; ETCHES, J.; BOND, I.; POTTER, K.; WEAVER, P. Morphing skins. **The Aeronautical Journal**, v. 112, n. 1129, pp. 117–139, 2008.

UEDA, J.; SECORD, T. W.; ASADA, H. H. Large effective-strain piezoelectric actuators using nested cellular architecture with exponential strain amplification mechanisms. **IEEE/ASME Transactions on Mechatronics**, v. 15, n. 5, pp. 770–782, 2010.

VALASEK, J. **Morphing Aerospace Vehicles and Structures**. [S.l.]: John Wiley & Sons, 2012. 312 pp.

VANGBO, M. An analytical analysis of a compressed bistable buckled beam. **Sensors and Actuators A: Physical**, v. 69, n. 3, pp. 212–216, 1998.

VIANA, F. A. C. **Surrogate modeling techniques and heuristic optimization methods applied to design and identification problems**. 2008. 156 pp. Ph.D. Thesis – School of Mechanical Engineering, Federal University of Uberlândia, Uberlândia, Minas Gerais, Brazil.

VOKOUN, D.; BELEGGIA, M.; ŠITTNER, P. Magnetostatic interactions and forces between cylindrical permanent magnets. **Journal of Magnetism and Magnetic Materials**, v. 321, n. 22, pp. 3758–3763, 2009.

WEISSHAAR, T. A. Morphing aircraft systems: historical perspectives and future challenges. **Journal of Aircraft**, v. 50, n. 2, pp. 337–353, Mar. 2013.

WEISSHAAR, T. A. Morphing aircraft technology – new shapes for aircraft design. In: NATO-RTO-MP-AVT-141 – Multifunctional Structures/Integration of Sensors and Antennas. Oct. 2–4, 2006, Vilnius, Lithuania. **Proceedings of NATO-RTO-MP-AVT-141**, O1-1 –O1-20.

WLEZIEN, R. W.; HORNER, G. C.; MCGOWAN, A.-M. R.; PADULA, S. L.; SCOTT, M. A.; SILCOX, R. J.; HARRISON, J. S. Aircraft morphing program. In: Smart Structures and Materials 1998: Industrial and Commercial Applications of Smart Structures Technologies. Mar. 1–5, 1998, San Diego, California, USA. **Proceedings of SPIE Vol. 3326**, pp. 176–187.

WRIGGERS, P. **Nonlinear finite element methods**. Chapter 9, Section 2. [S.l.]: Springer-Verlag Berlin Heidelberg, 2008.

XIONG, C.; LEI, Y.-M.; YAO, X.-F. Dynamic experimental study of deployable composite structure. **Applied Composite Materials**, v. 18, n. 5, pp. 439–448, 2011.

XU, P.; JINGJUN, Y.; GUANGHUA, Z.; SHUSHENG, B. The stiffness model of leaf-type isosceles-trapezoidal flexural pivots. **Journal of Mechanical Design**, v. 130, n. 8, pp. 082303-1–082303-6, 2008a.

XU, P.; JINGJUN, Y.; GUANGHUA, Z.; SHUSHENG, B.; ZHIWEI, Y. Analysis of rotational precision for an isosceles-trapezoidal flexural pivot. **Journal of Mechanical Design**, v. 130, n. 5, pp. 052302-1–052302-9, 2008b.

YONNET, J.-P.; ALLAG, H. Analytical calculation of cuboïdal magnet interactions in 3D. In: The 7th International Symposium on Linear Drives for Industry Applications. Sept. 20–23, 2009, Incheon, Korea. **Proceedings of LDIA 2009**, pp. 162–165.

ZHAO, J.; GAO, R.; CHEN, G.; LIU, S.; CAO, Q.; QIU, T. Nonlinear coupling mechanical model for large stroke magnetic-based multistable mechanisms. **Mechanism and Machine Theory**, v. 83, pp. 56–68, 2015.

ZHAO, J.; GAO, R.; YANG, Y.; HUANG, Y.; HU, P. A bidirectional acceleration switch incorporating magnetic-fields-based tristable mechanism. **IEEE/ASME Transactions on Mechatronics**, v. 18, n. 1, pp. 113–120, 2013.

ZHAO, J.; HUANG, Y.; GAO, R.; CHEN, G.; YANG, Y.; LIU, S.; FAN, K. Novel universal multistable mechanism based on magnetic–mechanical–inertial coupling effects. **IEEE Transactions on Industrial Electronics**, v. 61, n. 6, pp. 2714–2723, 2014a.

ZHAO, J.; ZHANG, Y.; HUANG, Y.; LIU, S.; CHEN, G.; GAO, R.; YANG, Y. Mechanical-magnetic coupling analysis of a novel large stroke penta-stable mechanism possessing multistability transforming capability. **Journal of Mechanisms and Robotics**, v. 6, n. 3, pp. 031004-1–031004-9, 2014b.